Summer 2014

Synthesis of silica based porous nanomaterials

Paul S. Mueller
University of Iowa

SYNTHESIS OF SILICA BASED POROUS NANOMATERIALS

by

Paul S. Mueller

A thesis submitted in partial fulfillment
of the requirements for the Doctor of
Philosophy degree in Chemistry
in the Graduate College of
The University of Iowa

August 2014

Thesis Supervisor: Professor Sarah C. Larsen

Graduate College
The University of Iowa
Iowa City, Iowa

CERTIFICATE OF APPROVAL

PH.D. THESIS

This is to certify that the Ph.D. thesis of

Paul S. Mueller

has been approved by the Examining Committee for the thesis requirement for the Doctor of Philosophy degree in Chemistry at the August 2014 graduation.

Thesis Committee: _____
Sarah Larsen, Thesis Supervisor

_____
Edward Gillan

_____
Amanda Haes

_____
Len MacGillivray

_____
Eric Nuxoll

To: My Family

Experience: that most brutal of teachers. But you learn, my God do you learn.

C.S.Lewis

ACKNOWLEDGEMENTS

First and foremost, I would like to acknowledge the contributions of my family. Their encouragement and support throughout my life made all I do possible. In their infinite patience, they tolerated the numerous of the odd culinary experiments over the years that foreshadowed my love of chemistry.

None of this work would be possible without the support of Professor Sarah Larsen. Professor Larsen always provided me with careful measure of guidance and independence. I am the scientist I am today because of her.

I would like to thank both current and past members of the Dr. Sarah Larsen Research Group. I am grateful to Ashish Datt, Anton Petushkov and Nicholas Ndiege all helped me to learn the ins and outs of research as a new graduate student. Shani Egodawatte, Sean Lehman, Cicily Ronhovde, Yulia Tataurova, and Melissa Torres have all aided me in my studies and were always willing to engage in scientific discourse. The support, advice, and friendship of these individuals is and has been a great source of motivation and strength.

I would also like to give a special thanks to all of the undergraduate and high school students whom it has been my great privilege to mentor: Mousa Abulssa, John Baer, Matthew Blake, Stephanie Chin, Destinee Gwee, Connor Parker, and Jiwhan Son. The contributions of these students helped me to accomplish more than I could have hoped.

Finally, I would like to acknowledge the support of the staff of the chemistry building. The work of these individual allowed me focus on my research and education.

ABSTRACT

Silica is one of the most abundant elements on the planet, has flexible bonding properties and generally excellent stability. Because of these properties, silica has been a vital component in technologies ranging from ancient glassware to modern supercomputers. Silica is able to form a wide range of materials both alone and as a component of larger material frameworks. Porous silica based nanomaterials are rapidly growing in importance because of their many applications in a wide variety of fields. This thesis focuses on the synthesis of silica based porous nanomaterials: nanocrystalline zeolites, mesoporous silica nanoparticles, and iron oxide core/shell nanocomposites. The synthetic conditions of these materials were varied in order to maximize efficiency, minimize environmental impact, and produce high quality material with far reaching potential applications. The materials were characterized by physicochemical techniques including Transmission Electron Microscopy, Dynamic Light Scattering, Powder X-Ray Diffraction, Solid State NMR, and Nitrogen Adsorption Isotherms. The materials were evaluated and conditions were controlled to produce high yields of quality nanomaterials and hypothesize methods for further synthetic control. The products will be used in studies involving nanoparticle toxicity, environmental remediation, and drug delivery.

TABLE OF CONTENTS

LIST OF TABLES

LIST OF FIGURES

CHAPTER 1: INTRODUCTION

1.1. Introduction to SiO_2 Based Porous Materials

Silicon is the second most common element in earth's crust and comes in many forms. The metalloid nature of Si allows this tetravalent element to readily bond to the degree that pure silicon is relatively rare. Silicon is frequently found bonded to oxygen, the most common of the elements in earth's crust, in the form of silicon oxides. In general, silicon oxide forms with four oxygen atoms surrounding each silicon atom forming large interconnected networks. This material has the formula SiO_2 and is known as silicon dioxide or silica and is able to form many different structures both crystalline and amorphous such as quartz and glass respectively. Additionally silica structures can really incorporate other elements such as aluminum. Silica is also able to form a variety of porous structures in both crystalline and amorphous forms. These silica based porous materials are well studied and used due to their variable properties high abundance. The work in this thesis focuses mainly on two types of silica materials: zeolites and mesoporous silica. A crystalline and amorphous material, respectively, these are both well utilized and studied classes of porous silica materials. There are numerous potential and future applications for zeolites and mesoporous silica which can be unlocked through continuous research and development.

1.2 Synthesis and Structural Properties of Zeolites

1.2.1. Current and Future Applications of Zeolites

Zeolite is the classification given to a group of aluminosilicate materials that possess a porous structure. Zeolites occur naturally and have been continuously mined for hundreds of years because of their many useful properties. Although all zeolites are comprised primarily of tetrahedra of silica and alumina, many distinct framework types exist. In addition to approximately 40 naturally occurring zeolites framework types, many more have been synthesized[1]. As of this writing, almost 220 unique zeolite framework types have been accepted by the International Zeolite Association[2]. These framework types such as those that are shown in Figure 1 are assigned three letter codes like FAU, LTL, and LTA. Within each of

these frameworks there is a degree of flexibility in regards to pore dimensions as well as elemental types and ratios.

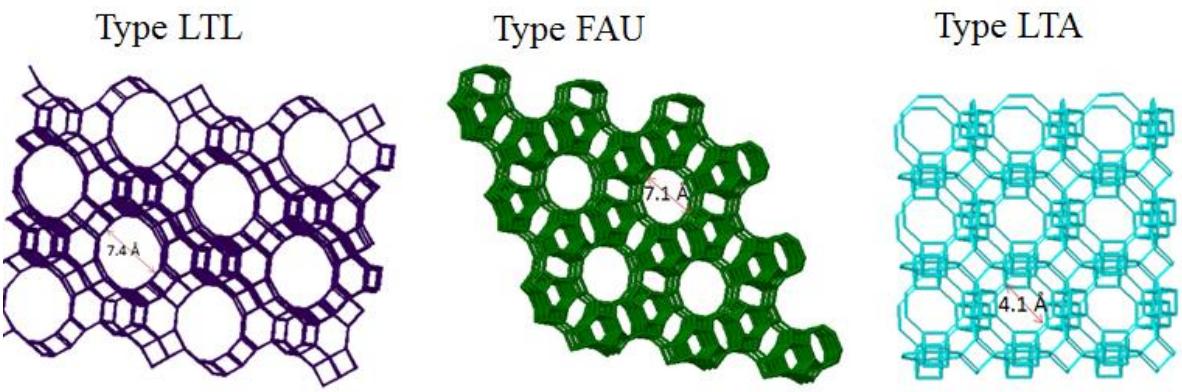

Figure 1 Three common zeolite framework types. The pore diameter of each framework type is displayed in angstroms.

Zeolites have a wide variety of applications including environmental remediation, catalysis, agriculture, and cleaning[3, 4]. This class of material is found in many commercial products such as cat litter, aquarium bedding, and detergent[4]. Zeolites are used for filtration and are an important part of the water purification process in many areas of the world[5]. Many of these applications utilize natural zeolites which are mined from deposits around the world. However, since the 1960s, synthetic zeolites have gained a more prominent role due to their usefulness in catalytic cracking reactions used in petroleum refining[4, 6].

When the usefulness of zeolites in the petroleum refining process was discovered, there was a drive to synthesize zeolites with properties that maximized their effectiveness in catalysis. While petroleum refining remains one of the leading driving forces for synthetic zeolite research, the controllable properties and nontoxic nature of synthetic zeolites generated great interest in this class of material. While synthetic zeolites are expensive compared to natural zeolites, their

tunable properties have generated considerable interest. Currently more than 1.4 million tons of synthetic zeolites are produced every year[4].

Synthetic zeolites have seen widespread use as catalysts due to their modifiable surface chemistry, robust structure, and general tunability. Currently synthetic zeolites are being studied for potential applications in areas such as healthcare where zeolites have been identified as potential drug delivery and imaging agents[7, 8]. Their high pore volume and modifiable surface properties allow for possible energy storage applications[9]. Because of the many current and future uses of synthetic zeolites, there will be a constant demand to continuously develop new methods for the synthesis and modification of this important class of material.

1.2.2. Factors Affecting Framework Type and Properties of Zeolites

The general formula for the zeolite framework is [$Al_xSi_yO_{(x+y)*2}$] and can be seen in Figure 2. In addition to Si and Al, other tetravalent atoms such as Ga, Ge, or Ti can also be substituted into the overall structure [10, 11]. Each of these tetrahedral atoms is surrounded by four oxygen atoms which together constitute secondary building units that lead to a wide variety of framework types. As can be seen in Figure 3, zeolites are comprised of secondary building units that in turn consist of oxygen surrounded tetravalent atoms. These framework types have well defined channels and structural units with repeating unit cells giving them a crystalline porous structure. The size, shape, and pattern of these pores are well defined due to the crystalline structure of the material and are typically micropores although mesoporous zeolites have been synthesized[12]. In general, zeolites possess pore diameters well below 10 Å[13]. The pores are generally limited to this sub nanometer size because the limited number of tetrahedra atoms that can stably form a ring.

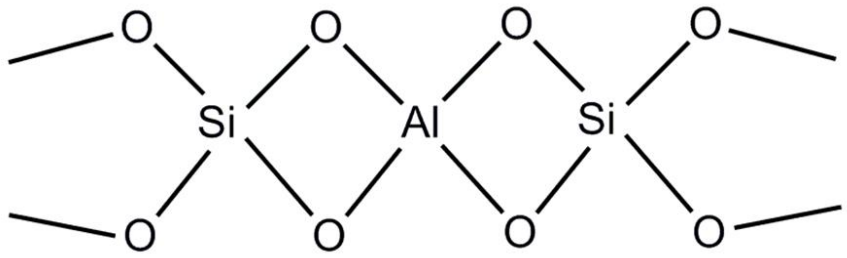

Figure 2 Atomic framework of an aluminosilicate zeolite.

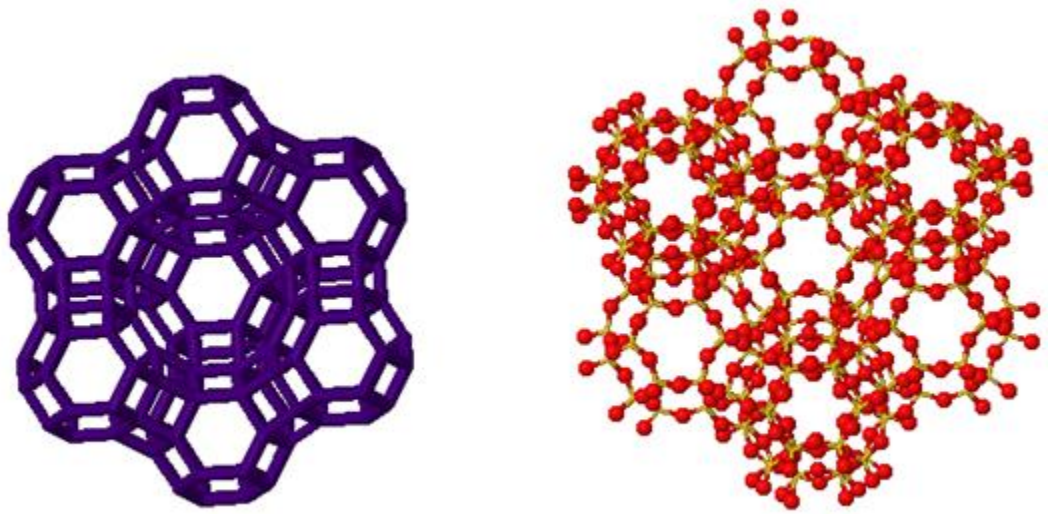

Figure 3 FAU type zeolite viewed as a stylized framework (left) and illustrated to include this zeolite's tetrahedral structure.

The structure of a zeolite allows each type of zeolite to have a wide range of properties. A large part of this variety is due to the tetrahedra building blocks of which the zeolite is comprised, specifically the Si/Al ratio. Si has an oxidation state of 4+ in tetrahedral coordination and thus has a neutral charge as a tetrahedral zeolite building block while Al has a 3+ oxidation state and thus possesses a net negative charge when tetrahedrally coordinated zeolite building block. Because of the negatively charged regions distributed through both external and internal surfaces, aluminoosilicate zeolites possess a large amount of ion exchangeable surface area.

During synthesis, cations from the synthesis reaction mixture (such as Na^+) become associated with the negatively charged alumina tetrahedra. These cationic species can be post synthetically exchanged with a wide range of cationic atoms and molecules. The negative charge of the alumina tetrahedra makes zeolites with low Si/Al ratios useful as acid catalyst zeolites because they can contain large amounts of protons which balance out the negative charges of the alumina tetrahedra [14]. Coupled with the durability inherent in their crystalline structure, the ability to act as strong acid catalysts is part of what allows zeolites to be widely used for catalytic cracking. However, it should be noted that control of the Si/Al ratio is critical as the stability of a zeolite partially depends on this ratio. For example, as the Si/Al ratio of zeolite Y decreases, overall stability decreases especially under low pH conditions as Al is removed from the framework[15, 16].

The surface of a zeolite is significantly modifiable. In addition to the anionic partners enabled by the cationic alumina species, numerous silanol groups exist on both the external and internal surfaces as depicted in Figure 4. These can be modified with the addition of functional groups to further modify the zeolite surface properties. For example, silane groups such as aminopropyltriethoxysilane (APTES) and 3-mercaptopropyltrimethoxysilane (MPTS) add biologically and chemically important amine and sulfur groups respectively to the zeolite surface [17, 18]. Typically, only the external surfaces of zeolites are functionalized because of their relatively small pore sizes which block large molecules from entering[19]. The controllable pore morphologies of synthetic zeolites also allow for size exclusion based functionalization of internal surface versus external surfaces which can be useful for catalytic applications and potentially drug delivery[20, 21].

The already high surface area and accessible pore volume inherent in a zeolite can be further improved by moving to the nanoscale. Nanocrystalline zeolites are defined as any zeolite that has at least one dimension of less than 100 nm. Nanoscale zeolites have a much larger external surface area compared to bulk zeolites which improves the availability of inner surfaces and makes them useful for certain applications such as those where catalytic reactions take place

on the surface[22]. In addition, nanoscale zeolites have decreased diffusion lengths as their size decreases[23]. These properties allow nanocrystalline zeolites to be useful materials especially for improving heterogeneous catalytic reactions in gas-solid and liquid solid systems[24]. Nanocrystalline zeolites are being investigated for applications including drug delivery, environmental remediation, and various forms of catalysis[25].

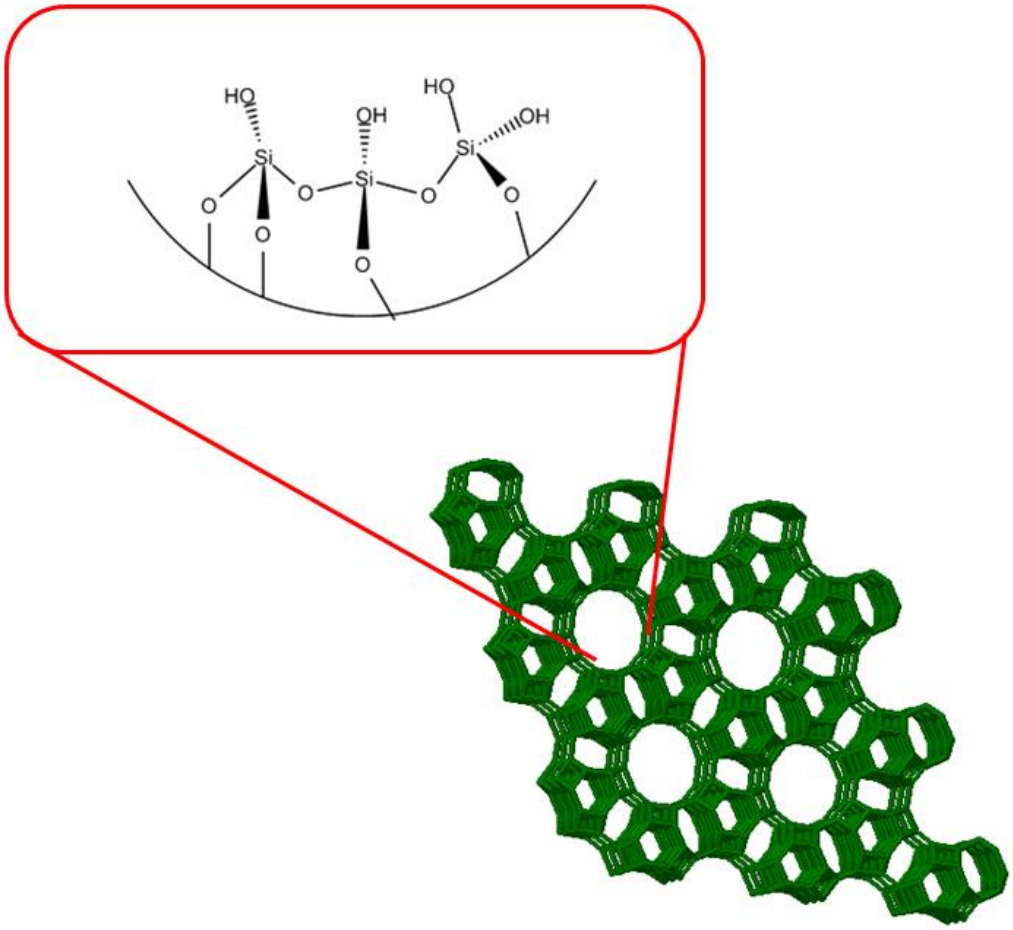

Figure 4 An illustration of the surface silanol groups on the surface of a zeolite. Generally, only the external silanol groups are accessible due to the small pore size.

1.2.3. Synthesis Strategies for Nanocrystalline Zeolites

Nanocrystalline zeolites are most frequently produced through bottom up approaches. Bottom up approaches typically offer improved control and increased crystal quality[22]. In a top down approach, a larger zeolite crystals are brought down to the nanoscale through the use of a techniques such as ball milling; however, the nanocrystalline zeolite produces produced in this way tend to be much more polydisperse compared to bottom up methods. In bottom up methods, nanocrystalline zeolite synthesis conditions can be carefully controlled from the start. Unfortunately, the bottom up methodology also generates a lower overall yield compared to the top down approach. However, efforts are being made to improve overall yield and will be discussed later. Ultimately, the large amount of experimental control afforded by the bottom up synthetic approach is sufficient to justify this approach in spite of the limitations.

The synthetic process for bottom up synthetic nanocrystalline zeolites generally utilizes a closed nutrient pool[26]. As such, the initial reaction conditions determine in very large part the final properties of the product. The initial reaction conditions typically favor nucleation over growth because as the number of nuclei in a closed nutrient pool increases, the ultimate crystal size decreases[26]. Besides controlling size, the initial reaction conditions can control such aspects of the final product as framework type, dimensions, elemental ratios, and initial surface functionality.

In general, nanocrystalline zeolites are synthesized in basic conditions and utilize a silica source, an alumina source, a structural directing agent (SDA) and a cation source to balance out the negative charges on the alumina tetrahedra. The mechanism of nanocrystalline zeolite formation includes hydrolysis, association, nucleation, and growth[27]. While the exact formation mechanism for zeolites is not completely understood, there are many proposed mechanisms based on experimental data which tend to agree on several key points[27]. A proposed mechanism of zeolite formation from a supersaturated closed nutrient pool appears in Figure 5. The general proposed mechanism involves a cationic species being surrounded by water which is subsequently replaced by anionic tetrahedra [27, 28]. These tetrahedra

surrounded cations can be SDAs such as tetra propyl ammonium hydroxide (TPAOH) and single elemental cations such as Na^+. The SDA cation/tetrahedra systems rearrange themselves based on hydrogen bonding gaining and ionic interaction gaining order to form secondary building units and subsequently nucleation sites [27, 28]. After the initial nucleation, the solution should no longer be supersaturated and thus subsequent nucleation should not occur. The proto crystals precede grow into full nanoscale zeolite crystals over a period of hours, days, or weeks.

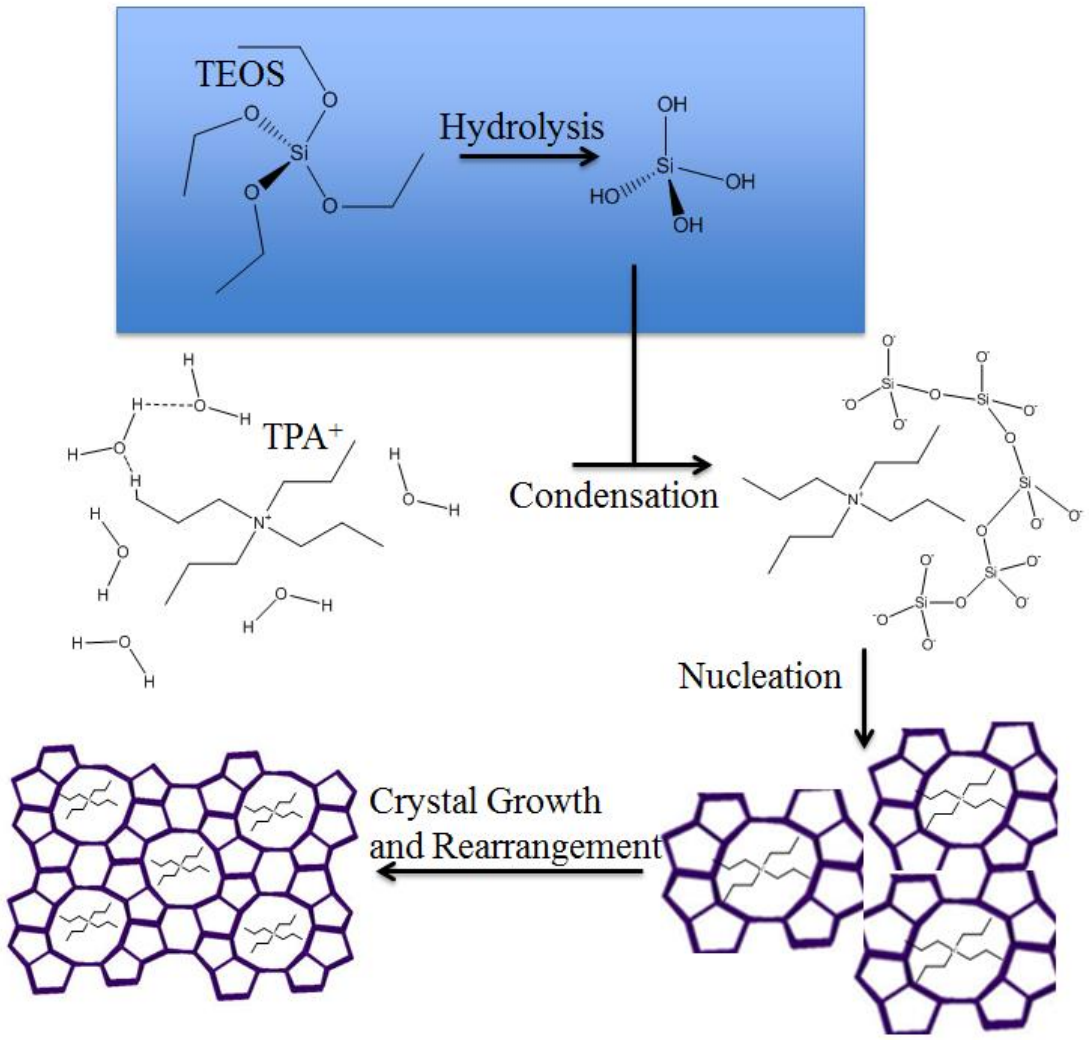

Figure 5 Formation of zeolite from using TPAOH in a supersaturated aqueous solution with TEOS as the silica source.

In order to generate homogeneous particles, the nucleation and growth phases must occur with as little overlap as possible; and ideally, be completely separate. Nucleation should be a burst process followed by a set period of growth that brings the zeolite nanocrystals to their desired size and crystallinity. Control of this process is accomplished through the temperature, time, and initial reaction concentrations.

One of the major components of the reaction mixture that determines the structure of the zeolite is the choice of template. As discussed above, the cationic and hydrogen bonding forces play a large role in zeolite formation and thus the template used is typically an organic cationic ammonia species. The bonding properties and physical shapes of the organic templates used dictates in large part the structure and dimensions of key zeolite building units. For example, TMAOH can lead to the formation of a secondary building unit known as a sodilite cage. In general, larger templates lead to larger pore sizes and vice versa. Figure 6 demonstrates the formation of the zeolite framework around an organic template, in this case, TPAOH, and subsequent removal of the template to create the pore structure. Additionally it is possible to synthesize zeolites without organic templates. Many zeolites have been synthesized without an organic template including Zeolite L, Zeolite X, and ZSM-5 [29-31].

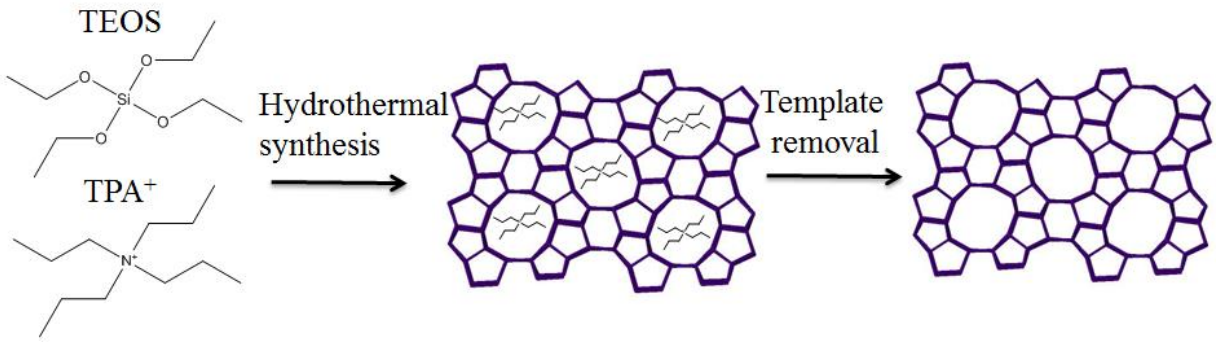

Figure 6 Synthesis procedure for TPAOH templated zeolite. The template is removed after synthesis resulting in a porous structure.

The initial silica and alumina tetrahedra concentrations of the reaction mixture also have an effect on the final nanocrystalline zeolite. There are a wide range of silica and alumina sources available and they vary widely in terms of hydrolysis rate in a given system and thus the amount and ratio of tetrahedra of available elements present in a solution at a given time. Different Si/Al ratios can produce zeolites with different dimensions and even different framework types. As previously alluded, sources of Ge, Fe, Ti and many other tetravalent and trivalent elemental sources can be utilized in the initial reaction mixture and can substitute for Si, Al, or both. This adds further dimensions to the possibilities of this class of material.

Furthermore, additional control can be established by use of seeding. In seeding, small nanocrystalline zeolites or nucleation sites are added to a zeolite producing reaction mixture. These seeds act as nucleation sites for zeolite crystal growth and tend to increase the overall reaction rate compared to non-seeded zeolite growth. This may be due to an increase in solid phase surface area for the solution nutrients to deposit and grow upon[32]. Seeding is also an important part of the process of recycling the zeolite reaction mixture for improving overall synthetic yield.

Due to the overall complexity of the zeolite reaction mixture, the exact mechanisms of zeolite growth and the explanations of why certain control techniques work is still being studied. Aspects of the zeolite growth process are still debated. As deeper understanding of the formation reactions would allow for greater control, much research is being done in this area. Despite the introduction of various other highly porous materials to the field of materials chemistry, zeolites remain relevant.

1.3. Synthesis and Structural Properties of Mesoporous Silica

1.3.1. Applications of Mesoporous Silica

Like zeolites, mesoporous silica has a porous structure; however, unlike silica, this material is amorphous. Additionally, as named, mesoporous silica contains mesopores which are pores between 2-50 nm in size. This is much larger than the microporous structure of zeolites which have pores < 1 nm in size. Mesoporous silica is currently being investigated for

many potential applications, notably in areas such as healthcare, sensing, environmental remediation, catalysis, and optics. These applications are made possible by the general stability, inert nature, porous structure, and tunable structures. Like zeolites, the large amount of functionalizable surface area in mesoporous silica can be functionalized with a variety of functional groups in order to selectively absorb environmental contaminants or control solution affinity. Mesoporous silica was originally developed as a catalyst but this material is of considerable interest in many diverse fields.

Numerous studies have demonstrated the possibility of utilizing mesoporous silica for use in healthcare [33-37]. Most frequently, this class of materials appears in studies involving drug delivery and biomedical imaging [33, 38]. The large pore volume of mesoporous silica allows this class of materials to contain large quantities of drug molecules. Mesoporous silica has been used to develop intelligent drug delivery systems which are able to release the drugs based on external triggers such as pH [34]. Medical imaging is usually accomplished by combining mesoporous silica nanoparticles with magnetically active material such as gadolinium or manganese oxide[38, 39]. There is also the potential to combine imaging and drug delivery into a single therapeutic platform[40].

1.3.2. Structural Properties of Mesoporous Silica

Mesoporous silica has an amorphous and tunable silica structure. This type of silica shows much less structural order than a crystalline structure such as a zeolite as can be seen in Figure 7. The amorphous nature of mesoporous silica allows the material a degree of flexiblity in regards to the overall structural properties as the framework is not crystalline allowing for a wider range of pore shapes and sizes compared to zeolites. Mesoporous silica can also have a wide range of morphologies and dimensions. The flexibility of this material allows for a wide range of properties and uses.

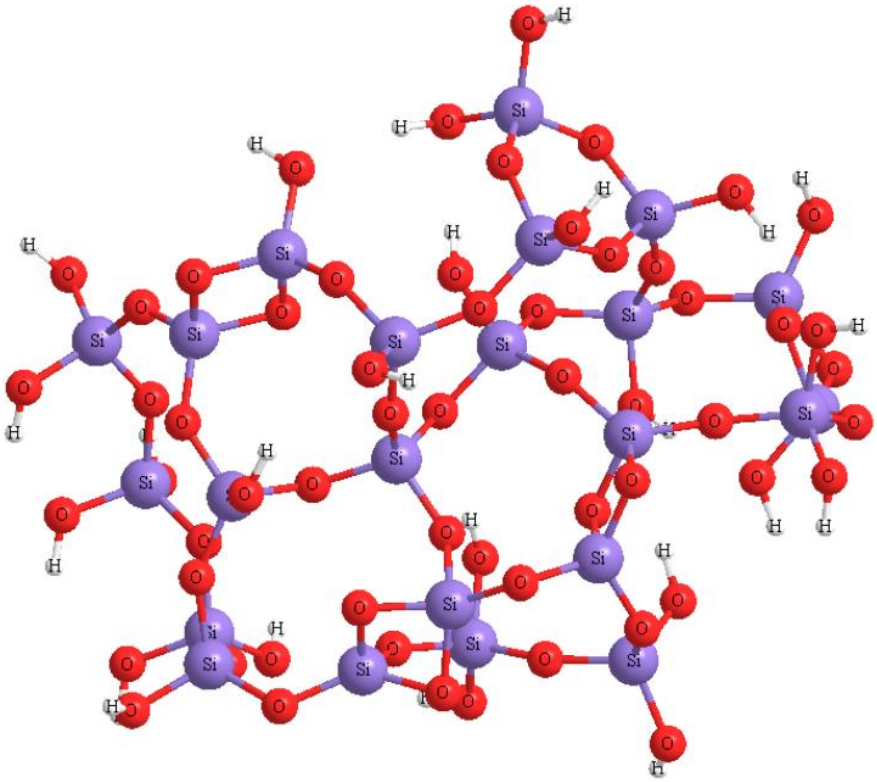

Figure 7 Ball and stick model of the amorphous structure of silica.

Like zeolites, a major draw of this material class is due to versatility. Mesoporous silica can to be tailored to a wide range of tasks. Key physical parameters such as pore dimensions, pore volume, wall thickness, size, and morphology can be controlled synthetically. In another important similarity to zeolites, mesoporous silica is covered in silanol groups allowing for a wide range of surface chemistry applications. As previously mentioned, an important distinction between zeolites and mesoporous silica is pore size and the silanol groups on the mesopores of mesoporous silica are easily accessible. As such, both the internal and external surface area can be functionalized allowing the surfaces to be covered a wide variety of functional groups such as reactive amines. Figure 8 shows the functionalization of the silanol groups of a mesoporous silica pore with APTES forming a surface amine which could be used as is or further functionalized for a variety of applications.

As befitting a material originally developed for catalysis, mesoporous silica is stable under a wide range of conditions. Mesoporous silica has been shown to be stable at temperatures up to 850 °C in air and 800 °C under 8 torr of water vapor [41, 42]. Mesoporous silica has good long term stability in saline conditions [43]. However, this class of materials tends to be incompatible with basic aqueous conditions [44, 45]. Additionally, while stable in slightly acidic conditions, mesoporous silica begins to lose surface area and degrade under extremely acidic conditions[45]. The stability of a given mesoporous silica structure depends on such factors as silica pore size and wall thickness with smaller pores and thicker walls granting the material greater stability in extreme conditions[45].

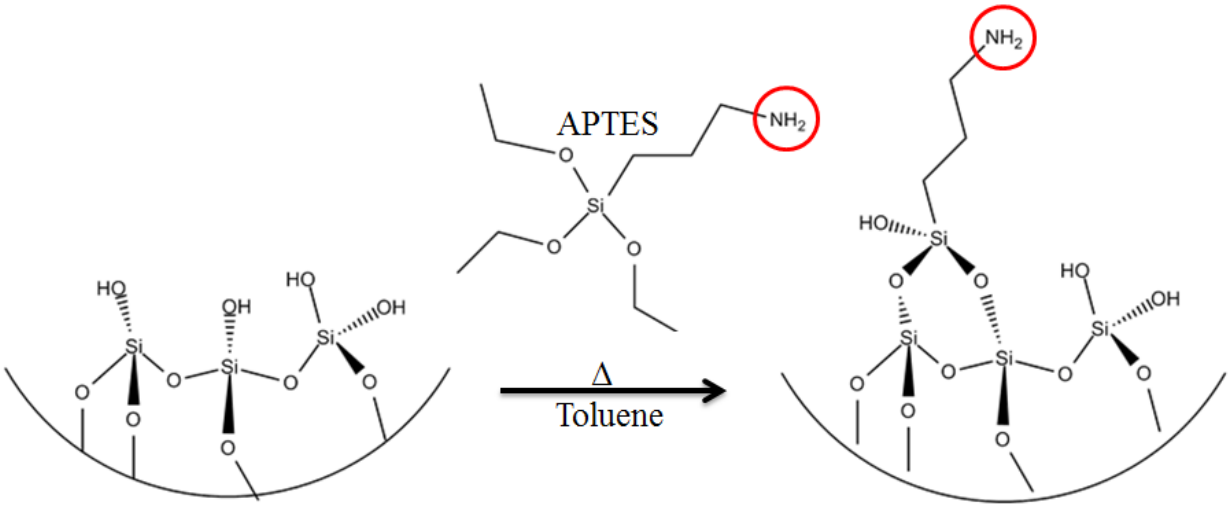

Figure 8 Surface functionalization silanol groups with APTES. This reaction adds a reactive amine group to the internal or external surface of the material. APTES is one of many silanes commonly used with silanol groups to add surface functionality to mesoporous silica.

Unlike zeolites, there are no known naturally occurring mesoporous silica species; all known forms are synthetic. However, like zeolites, there are multiple types of mesoporous silica that are classified based on their pore structure. Mesoporous silica can possess a wide variety of different mesostructures including disordered, wormhole, cubic, and hexagonal[44]. Within

these pore arrangements; there exist multiple pore sizes and wall thicknesses. While countless combinations of these characteristics exist to form many mesoporous silicas, several of the more well-studied permutations are named. Among the more well known of these mesoporous silica materials are SBA-15, HMM-33, MCM-41, and Wormhole (WO). A TEM of the well-ordered pore structure of MCM-41 is compared to the disordered structure of WO silica in Figure 9 to illustrate the wide range of pore topology possible.

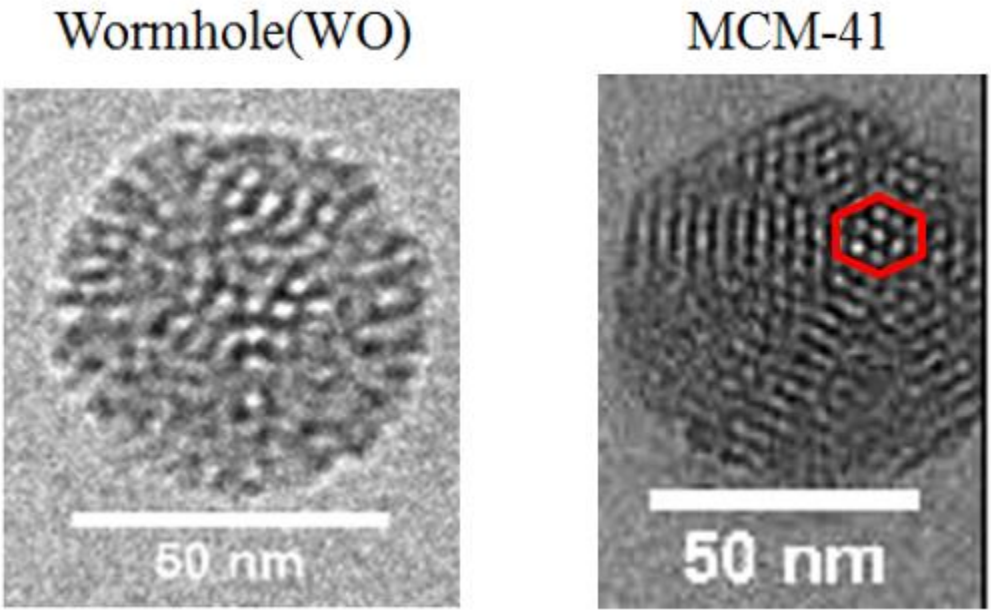

Figure 9 TEM images of 50 nm mesoporous silica with the wormhole (WO) (left) and MCM-41(right) pore topology. MCM-41 displays an ordered hexagonal pore structure while WO displays a disordered pore topology.

1.3.3. Synthesis of Mesoporous Silica

The basis of the formation of mesoporous silica relies on the hydrolysis and condensation of a silica source or sources. Mesoporous silica can be synthesized in both basic and acidic environments and typically relies on a surfactant template to produce their mesostructures. Additional additives are typically employed to adjust the properties of the material toward a

desired structure. There are many factors that control the formation of mesoporous silica species and a great deal of mesoporous silica related research has focused on the systematic variation of synthesis conditions to probe formation mechanisms and develop more rational synthetic methodologies.

The formation of mesoporous silica can be controlled through control of the reaction system. There are numerous factors that determine the final form of the mesoporous silica. This offers many opportunities to tailor the properties of the final product for specific applications. For example, the dimensions of the templating micelles which control the final pore size, shape, and morphology can be altered in numerous ways with temperature, additives, and stirring conditions. Because one of the major draws of mesoporous silica are is materials ability to be structurally tuned to various applications and thus central to mesoporous silica research is the search for methodologies that allow for greater structural control. The mesoporous silicas central to the research presented in this thesis are surfactant templated and are synthesized in basic conditions. The major known factors that are vital to the structural and size control are reagent choice, reagent concentration, pH, temperature, and synthesis time.

The general synthetic mechanism of mesoporous silica is fairly well understood and an example a synthesis is shown in Figure 10. In a typical surfactant based synthesis of mesoporous silica, a surfactant is added to an aqueous solution until the critical micelle concentration is reached and the surfactant molecules associate to form micelles. A base is added along with a silica source which is hydrolyzed and self organizes with the surfactant. The hydrolyzed silica source proceeds to condense forming the mesoporous silica. Finally, the surfactant and any additional organic species are then removed to open the pores. The template removal step can be accomplished through calcination or by solvent assisted template extraction.

The major components of a basic mesoporous silica reaction mixture are water, surfactant, base, and a silica source. There are many potential surfactants, bases, and silica sources that can be employed. In addition, there are many additives that can offer supplementary control including pore expanding agents such as *N*,*N*-dimethyldecylamine (DMDA) and alkane

as well as organic solvents such as ethanol which lowers the rate of hydrolysis [46-48]. A common class of additives that appear in Figure 11 are small organic amines (SOAs) which besides acting as a base source can act as chelating agent to control rate of silica formation as well as an encapsulating agent to prevent particle intergrowth and limit particle size. By making effective use of the tools available, a great deal of synthetic control is possible.

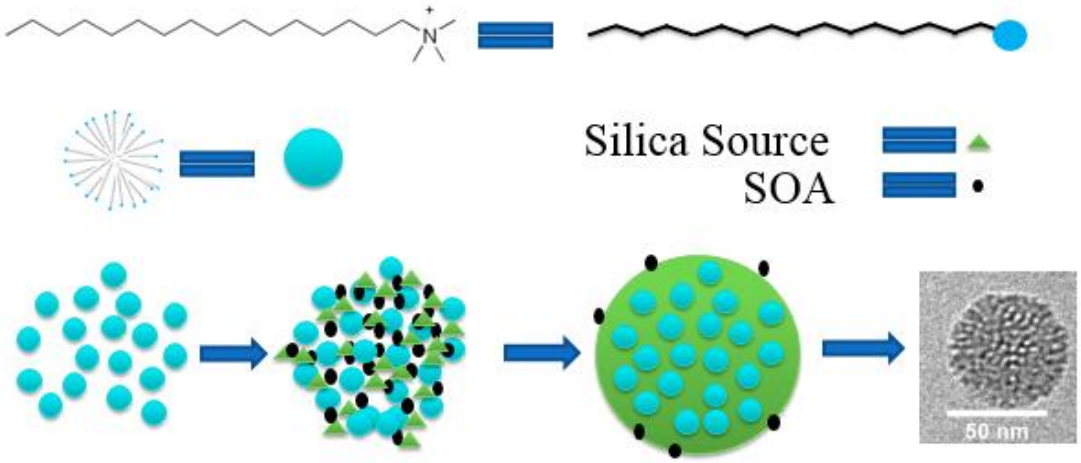

Figure 10 Synthesis of mesoporous silica utilizing a small organic amine (SOA) as a base and CTA^+ based surfactant in an aqueous solution. In the process shown, the CTA^+ molecules form micelle in the aqueous solution. Ionic attraction of the negatively charged hydrolyzed silica source to the cationic micelles causes association. The hydrolyzed silica condenses to form a silica shell around the micelles. The SOAs interact with the silica source to slow hydrolysis and condensation. As particle formation and condensation occur, acts as encapsulating agents to prevent further particle growth and intergrowth.

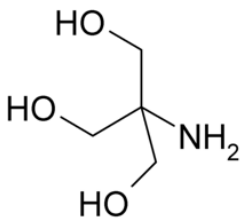

tris(hydroxymethyl)aminomethane (Tris buffer)

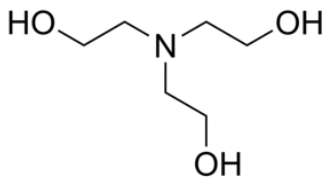

Triethanolamine (TEA)

Figure 11 Commonly used small organic amines (SOAs).

1.4. Iron Oxide Nanoparticles

1.4.1. Applications of Iron oxide Nanoparticles

Iron oxide nanoparticles are one of the most used types of nanoparticles. Iron oxide nanoparticles are used in numerous and varied fields including optics, healthcare, catalysis, environmental remediation, batteries, sensing, and magnetic storage [49-53]. Iron oxide nanoparticles are able to adsorb contaminants such as arsenic from water, are able to form highly conductive networks for battery applications, and are gaining increasing interest as MRI contrast agents. Iron oxide nanoparticles not only have many potential applications, but are a vital component of current technologies. Among other applications, high density magnetic storage devices containing iron oxide nanoparticles are already on the market, and Feraheme, a drug utilizing magnetite (Fe_3O_4), is used in the treatment of anemia.

Iron oxide nanoparticles are widely used because of their many advantageous properties. Like the bulk, Iron oxide nanoparticles are crystalline as can be seen in the p-XRD pattern of Fe_3O_4 nanoparticles shown in Figure 12. Iron oxide nanoparticles have considerably different properties from the bulk. Besides the increase in surface area that is observed for all nanoparticles, the magnetic properties of iron oxide nanoparticles can vary considerably compared to the bulk. In Fe_3O_4 nanoparticles, magnetic domain changes can result in superparamagnetic behavior. This is because while bulk Fe_3O_4 has multiple domains, nanoparticles below a critical size (about 20 nm at room temperature) contain only a single

domain[54]. Furthermore, the size and morphology of iron oxides can be controlled to an ever increasing degree[55]. In general, iron oxide nanoparticles are simple and inexpensive to produce in large quantities and are easy to purify and separate from solution due to their magnetic properties. While there is some concern about the effect of large concentrations of iron oxide nanoparticles on the body, generally, iron oxide nanoparticles are considered biocompatible because the they can be easily dissolved and digested by the human body[53, 56, 57]. Like all nanomaterials however, a larger body of research including long term exposure effects will be necessary to determine the overall safety of this nanomaterial.

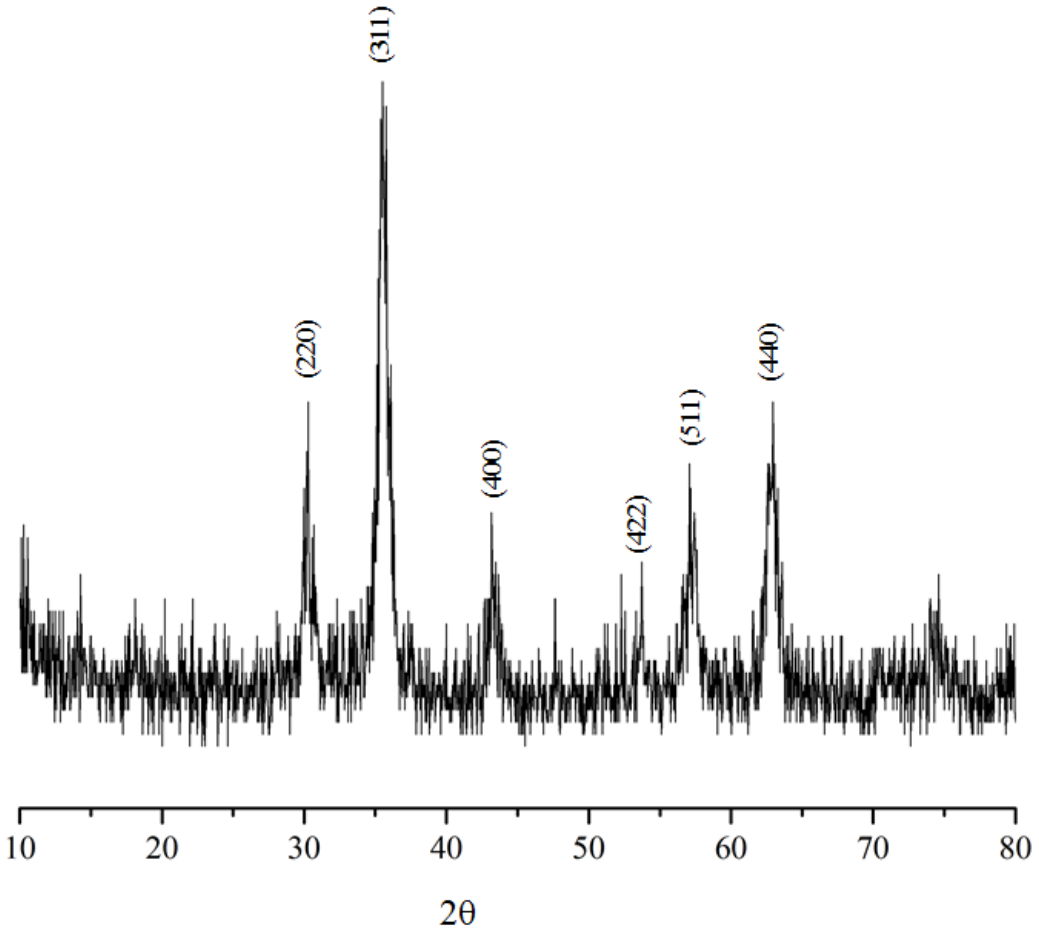

Figure 12 p-XRD of Fe_3O_4 nanoparticles of about 13±2 nm in diameter. Characteristic miller indices appear over the diffraction peaks.

1.4.2. Synthesis of iron oxide nanoparticles

As previously mentioned, the synthesis of iron oxide nanoparticles is a fairly simple and straightforward process. While many methods of iron oxide synthesis are known, the most common utilize coprecipitation. Coprecipitation methods are popular because these methods allow for the production of large quantities of iron oxide nanoparticles with a moderate degree of particle uniformity. The major disadvantage of coprecipitation is the lack of fine particle size control as size is primarily determined by kinetic factors[55]. These reactions are typically preformed in aqueous environments and utilize a base to initiate the reaction.

The coprecipitation method of iron oxide nanoparticles has a fairly well understood mechanism. The initial solution consists of iron sources dissolved in an aqueous solution. The iron sources are typically iron salts such as $FeCl_3$ or organic complexes such as $Fe(acac)_2$ which are able to easily dissociate in solution forming Fe cations. These cations react in a basic environment to form an iron oxide. For example, Fe_3O_4 is formed according to the reaction: $Fe^{2+}+2Fe^{3+}+8OH \rightarrow Fe_3O_4+4H_2O$ and is illustrated in Figure 13. Like zeolites, the quality of the final product depends on a quick burst of nucleation followed by a growth phase where these two phases have little or no overlap. If these phases are not well separated, control of particle size will be severely hindered.

The type and properties of the iron oxide nanoparticles produced can be controlled by varying the reaction conditions. One of the most important conditions to control during the synthesis of iron oxides is the oxygen content of the reaction mixture. Synthesis of Fe_3O_4 is typically preformed in oxygen controlled environments due to the inherent instability of Fe_3O_4 in oxygen[55]. Moreover, Fe^{2+} is really oxidized to Fe^{3+} in aqueous solutions, altering Fe^{2+}/ Fe^{3+} ratio the reaction mixture resulting in the potential formation of unwanted species of iron oxides. Thus, nitrogen or argon gas is typically used to purge the reaction mixture. Control over particle size, morphology, and uniformity is achieved by altering such factors as the Fe^{2+}/ Fe^{3+} ratio, temperature, time, and stir speed[50, 55, 58, 59].

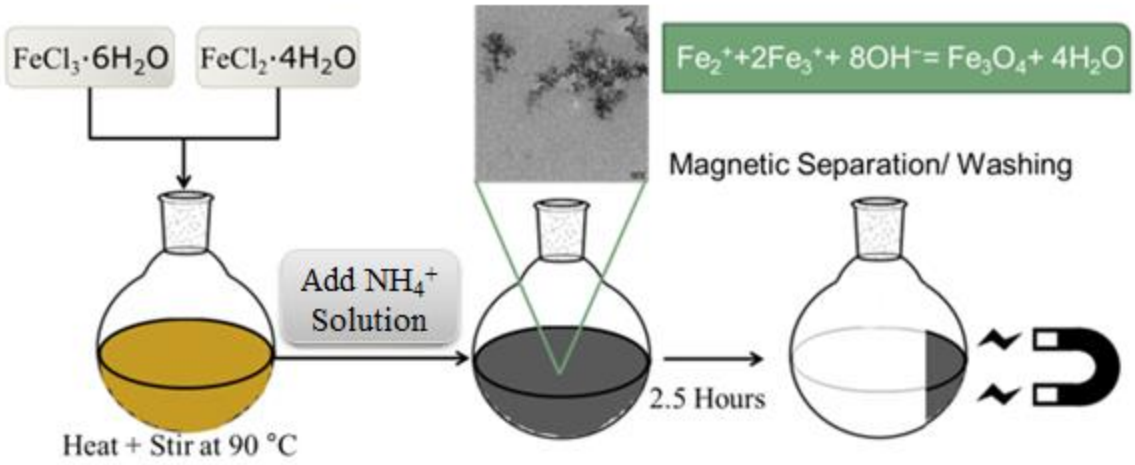

Figure 13 Synthesis of iron oxide nanoparticles. This procedure generates 13±2 nm Fe_3O_4 nanoparticles.

1.5. Iron Oxide Core/Shell Mesoporous Silica Nanocomposites

1.5.1. Structural Properties of Iron Oxide Core/Shell Mesoporous Silica Nanocomposites

In materials chemistry, new combinations of properties allow for new applications. One way to obtain the combination of properties desired is to combine two materials together to form a composite material. Iron oxide nanoparticles and mesoporous silica have been combined in such various ways to produce a variety of iron oxide core/shell mesoporous silica nanocomposite materials. A nanocomposite is a composite material that incorporates at least one material with dimensions less than 100 nm. In the case of iron oxide core/shell mesoporous silica nanocomposites, most literature focuses on the synthesis of nanocomposites with total particle dimensions of near or less than 100 nm. These materials typically consist of one or more iron oxide nanoparticles embedded in a mesoporous silica shell.

Iron oxide core/shell mesoporous silica nanocomposites combine the high, functionalizable surface area of mesoporous silica with the magnetic properties of iron oxide

nanoparticles. These particles have a large amount of tunability including pore size, amount of iron incorporation, particle size, and shell thickness. Additionally, both the internal and external surface of the mesoporous silica shell can be functionalized. Perhaps the most coveted property of these materials is their magnetic susceptibility which allows composites such as Fe_3O_4 core/shell mesoporous silica to be manipulated by magnetic fields both in and out of solution as demonstrated in Figure 14.

1.5.2. Applications of Iron Oxide core/shell Mesoporous Silica Nanocomposites

Like their component materials, the potential applications for iron oxide core/shell mesoporous silica nanoparticles are numerous. Fields including healthcare, catalysis, and optics are able to make use of their previously mentioned properties [60-62].

Within the field of healthcare, iron oxide core/shell mesoporous silica nanoparticles are a true emerging technology. Their tunable magnetic susceptibility coupled with the ability to functionalize their internal and external surfaces with fluorescent or radiolabeled functional groups makes them very attractive as imaging agents[63, 64]. They are also exciting candidates for new drug delivery systems, especially for drugs with high toxicities as magnetic fields could potentially be used to localize the drug loaded system to a target area thus mitigating harmful side effects[65].

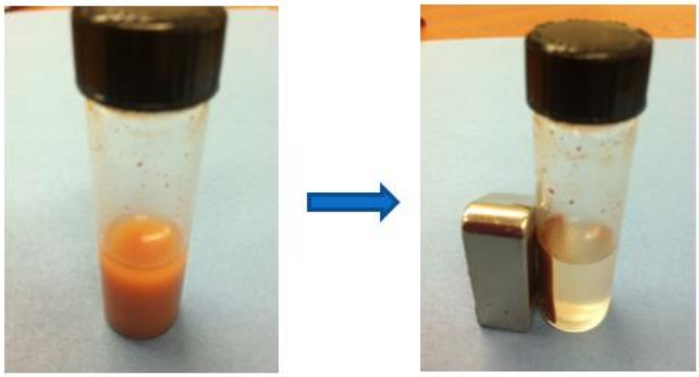

Figure 14 Magnetic susceptibility of Fe_3O_4 core/shell mesoporous silica nanocomposite in aqueous solution.

These materials are exceptionally well suited to catalysis. The mesoporous shell can be functionalized to with a variety of catalytically active groups to form a robust catalysis platform. After the reaction, the particles could be magnetically recovered from solution. Furthermore, the tunable pore sizes allow for size exclusion capabilities[66].

1.5.3 Synthesis of Iron Oxide Core/Shell Mesoporous Silica Nanocomposites

A large part of the draw of these materials is that in general, iron oxide core/shell mesoporous silica nanoparticles can be synthesized fairly quickly, easily, and inexpensively. In a basic synthesis, iron oxide nanoparticles are added to a reaction mixture similar to one that would produce mesoporous silica. In most cases, the iron oxide nanoparticles are surface treated prior to addition in order to maximize dispersibility [54, 62, 67]. Sonication is typically employed to fully disperse the iron nanoparticles in solution prior to the addition of the silica source. The synthesis procedure varies considerably depending on the desired final product. The general process as well as individual synthetic mechanisms is coved in depth later in this thesis.

1.6. Thesis Overview

The work presented in this thesis focuses primarily on the synthesis and characterization of silica based nanomaterials, including zeolites and mesoporous silica, as well as core/shell nanomaterials. Chapter 1 focuses on introducing the materials used in this work. This includes synthesis conditions, physical properties, and applications of each major class of material. Chapter 2 focuses on the synthesis of both nonporous and mesoporous silica for use in toxicology and NMR studies as well as the functionalization of these materials. Chapter 2 also contains a short discussion on the use of nitrogen adsorption as a characterization technique for mesoporous silica based materials. Chapter 3 concerns the synthesis of a germanium substituted zeolite of the framework class FAU. Also included in Chapter 3 are strategies towards improving the yield of this material and zeolites in general. The synthesis of iron oxide core/shell mesoporous silica nanocomposite nanoparticles is discussed in Chapter 4.

Specifically, Chapter 4 details greener methods for synthesis which result in higher yields of nanocomposite with less waste. This is particularly important as many applications of iron oxide core/shell mesoporous silica require large amounts of this material. Chapter 5 illustrates a true one pot synthesis of iron oxide core/shell mesoporous silica nanocomposites using only inexpensive, commercially available precursors. While iron oxide nanoparticles are usually treated as a reagent in the literature of the synthesis of iron oxide core/shell mesoporous silica nanocomposites, in the synthetic procedures outlined in Chapter 5 of this thesis the iron oxide nanoparticles are synthesized in solution en route to the final product. Finally, the conclusions drawn from this thesis work as well as future work are detailed in Chapter 6.

CHAPTER 2: SYNTHESIS OF NONPOROUS AND MESOPOROUS SILICA MATERIALS FOR APPLICATIONS IN HEALTH AND THE ENVIRONMENT

2.1. Introduction

Many fields of science and industry target mesoporous silica as a material of intense interest. Among other applications, mesoporous silica is a key player in aspects of both health and environmental remediation research. The versatility of mesoporous silica is important in these fields as these areas as they demand a high degree of tunability and flexibility.

Increased industrialization and production across the planet has resulted in many direct environmental effects. One of the more worrying consequences of this increase is an accompanying increase in the number and amount of contaminants released into the water table. These contaminants pose serious health and environmental threats and their removal from the water supply is of great importance. Mesoporous silica has emerged as a viable material for the adsorption of contaminants due to the materials modifiable surface chemistry, high surface area, and relatively low cost[26]. Mesoporous silica is covered in silanol groups which impart a negative surface charge giving many cationic contaminants an affinity to the material resulting in high adsorption[68, 69]. While this surface charge has intrinsic difficulties with the adsorption of anionic species, the readily modifiable surface of the silica allows for functionalization with a wide variety of surface groups [68, 70]. This allows for a surface that can be altered to have affinity and even selective adsorption towards many different contaminant species.

Controlled release of drugs is important particularly in the case of cytotoxic drugs like those used in cancer treatment[36]. By limiting the dosage and the area of effect to a particular target, side effects can be minimalized and the effectiveness of the treatment can be maximized. Mesoporous silica has also shown promise as a drug delivery agent due to the material's flexible properties, modifiable surface chemistry, high surface area, and expected low toxicity[34-36, 71]. The pore structure of mesoporous silica nanomaterials can be altered to accommodate a wide variety of drug sizes and loading methodologies. The structure of the mesoporous silica

nanomaterial can even be synthesized in such a way as to control the diffusion rate of a stored drug[72]. Additionally surface of the material can be coated in a number of functional groups to aid in biocompatibility and targeting of specific tissues and cells[34, 73].

For many applications of mesoporous silica to be seriously and widely implemented, the overall impact of these materials must be carefully studied. These materials would frequently come into contact with humans or be used within the human body, therefore, toxicology studies must be performed to determine the overall safety of these materials. The Food and Drug Administration recognizes silica as a Generally Recognized As Safe (GRAS) compound[74]. Bulk silica powders see use in industrial applications such as in paint, coatings, and lubricants and are also used as food additives, mainly as anticaking agents[75-78]. While both mesoporous and nonporous silica are amorphous in nature, crystalline silica has been implicated as a factor in numerous respiratory illnesses[79]. Coupled with the fact that nanoparticles are generally more reactive then their bulk counterparts, the toxicity of these materials is of critical importance. There have been several studies on the toxicity of sub 100 nm nanoparticles that make the beginning of the large body of research necessary to determine application specific safety of these materials[79, 80].

The continued outlook for mesoporous silica in both health and in the environment is promising. In order for these applications to move forward, there is still extensive research to be done regarding many aspects of mesoporous silica. In order to more fully understand and tune the structural and chemical properties of mesoporous silica to optimize the material for various applications, a wide variety of sizes and types of silica and mesoporous silica nanoparticles must be synthesized and tested. This chapter describes the synthesis and characterization of ~50 nm solid silica nanoparticles and wormhole type mesoporous silica nanoparticles.

2.2. Experimental Section

2.2.1. Materials

Triethanolamine, tetraethyl orthosilicate (TEOS), and a 25% Cetyltrimethylammonium chloride (CTACl) solution were obtained from Sigma Adrich and used without any further purification. Water purified with a Millipore CDF01205 Milli-Q 4-Carterage water purification system was used in all reactions. Absolute ethanol was used in all reactions involving ethanol.

2.2.2. Synthesis of Wormhole Type Mesoporous Silica

In a typical synthesis of ~50 nm diameter wormhole type mesoporous silica, 200 ml of water was combined with 33 ml of ethanol and 33 ml of 25% CTACl solution. The resulting solution was stirred for 20 mins. 13 ml of TEA was added and the solution was stirred an additional 30 mins at room temperature. The solution was then heated to 60 C° and stirred for 10 mins and 20.4 ml of TEOS was added rapidly under stirring at 500 RPM. The reaction mixture was allowed to heat and stir at 60 C° for 2 hours. The resulting 50 nm mesoporous silica nanoparticles were collected with high speed centrifuge at 8000 G for 30 mins. The product was then washed with water three times and ethanol once before being dried overnight (18h) at 80 C°. The nanoparticles were calcined at 600 C° for 6 hours resulting in a total yield of 4.01g. The product was then characterized by Powder X-Ray Diffraction (p-XRD), Transmission Electron Microscopy (TEM), Dynamic Light Scattering (DLS), and Nitrogen adsorption Isotherm (BET and BJH methods).

2.2.3. Synthesis of Nonporous Silica

Nonporous silica nanoparticles were obtained from a modified Stöber synthesis[81]. In the synthesis of 50 nm diameter nanoparticles, 120 ml absolute ethanol was combined with 6 ml of 28% by volume aqueous ammonia and stirred 24 hours at room temperature. The nanoparticles were collected by high speed centrifuge at 8000 G for 20 mins and washed with water and ethanol. The product was dried at 80 C° for 18 hours. The resulting nonporous silica nanoparticles were then characterized with DLS, BET, and TEM.

2.2.4. Functionalization

Portions of both nonporous and mesoporous silica were functionalized with (3-Aminopropyl)triethoxysilane (APTES). In a typical APTES functionalization, 2.5 grams of either mesoporous or nonporous silica nanoparticles were dried at 120 for 18 hours. The dry powder was then immediately suspended in a solution of 125 ml toluene 2.5 ml APTES. The suspension was heated to 120 °C and stirred at 500 RPM for 6 hours. The suspension was allowed to cool to room temperature and the product collected by centrifuge. The pellet was washed with toluene twice followed by two rinses with a 50:50 mixture of diethyl either and dichloromethane. The APTES functionalized mesoporous or nonporous silica product was then dried in an oven at 80 °C. The products were then characterized by BET and Thermogravimetric Analysis (TGA).

2.2.5. Characterization

A QuantaChrome Nova 1200 was used to measure both 7 point and full adsorption/desorption nitrogen isotherms. Using the 7 point and full isotherms respectively, Brunauer-Emmett-Teller (BET) and Barrett-Joyner-Halenda (BJH)/Density Functional Theory (DFT) were used to determine total surface area and pore size/volume. While BET is and has been the trusted standard model for determination of surface area the standard model for the pore size/volume determination is clear. Both BJH and DFT models are used in literature with materials containing mesopores (2-50 nm). Each model makes assumptions that must be takes into account when utilizing each model. BJH is based on the Kelvin equation which predicts pressures that condense/evaporate in a cylindrical pore[82]. The core assumptions of the theory is that the pore is cylindrical, that the adsorbate is evenly distributed over the entire surface area, and that the pores are filled layer by layer as the relative pressure increases in such a way that the small pores are filled before large pores[83]. DFT is a slightly more recent technique that is based on a combination of statistical mechanics and experimental isotherm data [82, 84, 85]. These mathematical models have been generated for how gases including nitrogen, argon, and

helium interact with a variety of solids including carbon and silica. Mathematical models for the behavior of gas-liquid and solid-gas interactions in confined geometries are compared to and calibrated with isotherm data from the interactions of target gases on target nonporous surfaces[84, 86]. This makes the DFT method very versatile as both the material of interest and adsorbate can be directly incorporated into the model used to determine pore size/diameter. Because the DFT method is slightly more recent, mesoporous silica literature generally reports pore size/volume using BJH for comparative purposes. Also, whereas the assumptions and parameters used in BJH calculations are fairly constant, DFT calculations have many parameters that must be selected and reported.

A Malvern Instruments Nano-ZS Zetasizer (DLS/zeta potential) was used to determine size for the nonporous spherical silica nanoparticles. DLS was used to estimate size of the mesoporous silica nanoparticles as interparticle aggregation made fine estimation of size using this technique unreliable. TEM was utilized with both nonporous and mesoporous silica nanoparticles to determine size and morphology. Image-J was used with the resultant TEM images to determine size in a quantitative manner by measurement of 50 individual particles. Finally, p-XRD gave information regarding the order and crystallinity of the materials.

2.3. Results and Discussion

The resulting nonporous and mesoporous silica nanoparticles were characterized by p-XRD (for mesoporous silica), nitrogen adsorption and TEM. The results are tabulated in Table 1. The mesoporous silica particles had a large surface area of 1122 m^2/g compared to the 66 m^2/g surface area of the nonporous silica particles. This high surface area is due to the mesoporous structure of the material as well as the small particle size. The pore volume appears virtually unchanged by functionalization remaining a steady 0.4 cm^3/g and a small decrease in pore diameter from 3.2 to 3.1 was observed by BJH. This disordered mesoporous structure was further confirmed by the p-XRD pattern (Figure 15) which showed a broad peak around 2.1 2θ. It should be noted that the peak typically broadens as particle size decreases. Functionalization

of the mesoporous silica nanoparticles resulted in a slight shifting and broadening of the peak in the p-XRD spectrum. TEM (Figure 16) indicated 49(5) nm spherical particles with a disordered WO pore structure.

Nonporous silica was shown to have an approximate size of 47(7) nm by TEM (Figure 16) and 49(4) nm by DLS. TEM indicated that the particles were roughly spherical. The surface area of the nonporous silica decreased from 66 to 42 m^2/g upon functionalization with APTES. Because of the material's lack of pore structure and long range order, p-XRD was not used.

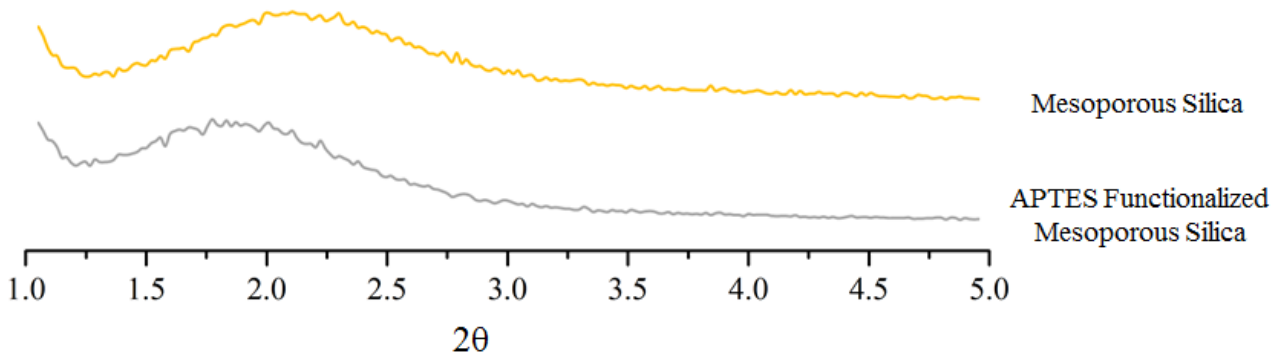

Figure 15 p-XRD of WO mesoporous silica before and after functionalization with APTES.

2.4. Conclusions

Both nonporous and mesoporous silica nanoparticles with dimensions of ~50 nm were successfully synthesized and functionalized with APTES. These nanoparticles will be used for toxicology studies to determine the viability of these materials for use in such areas as drug delivery and medical imaging. In order to generate a more complete body of knowledge regarding the toxicological effects of these materials, more particle sizes, morphologies and functionalization procedures may need to be studied.

Table 1 Characterization of functionalized and non-functionalized mesoporous silica and nonporous silica nanoparticles.

Sample	Surface Area (m^2/g)	Pore Volume (cm^3/g)	Pore Diameter (nm)	Size (nm)
MS-WO	1122(8)	0.4(0)	3.2(0.04)	49(5)
MS-WO APTES	699(5)	0.4(0)	3.1(0.02)	49(5)
Solid Silica	66(0)	N/A	N/A	47(7)
Solid Silica APTES	42(0)	N/A	N/A	47(7)

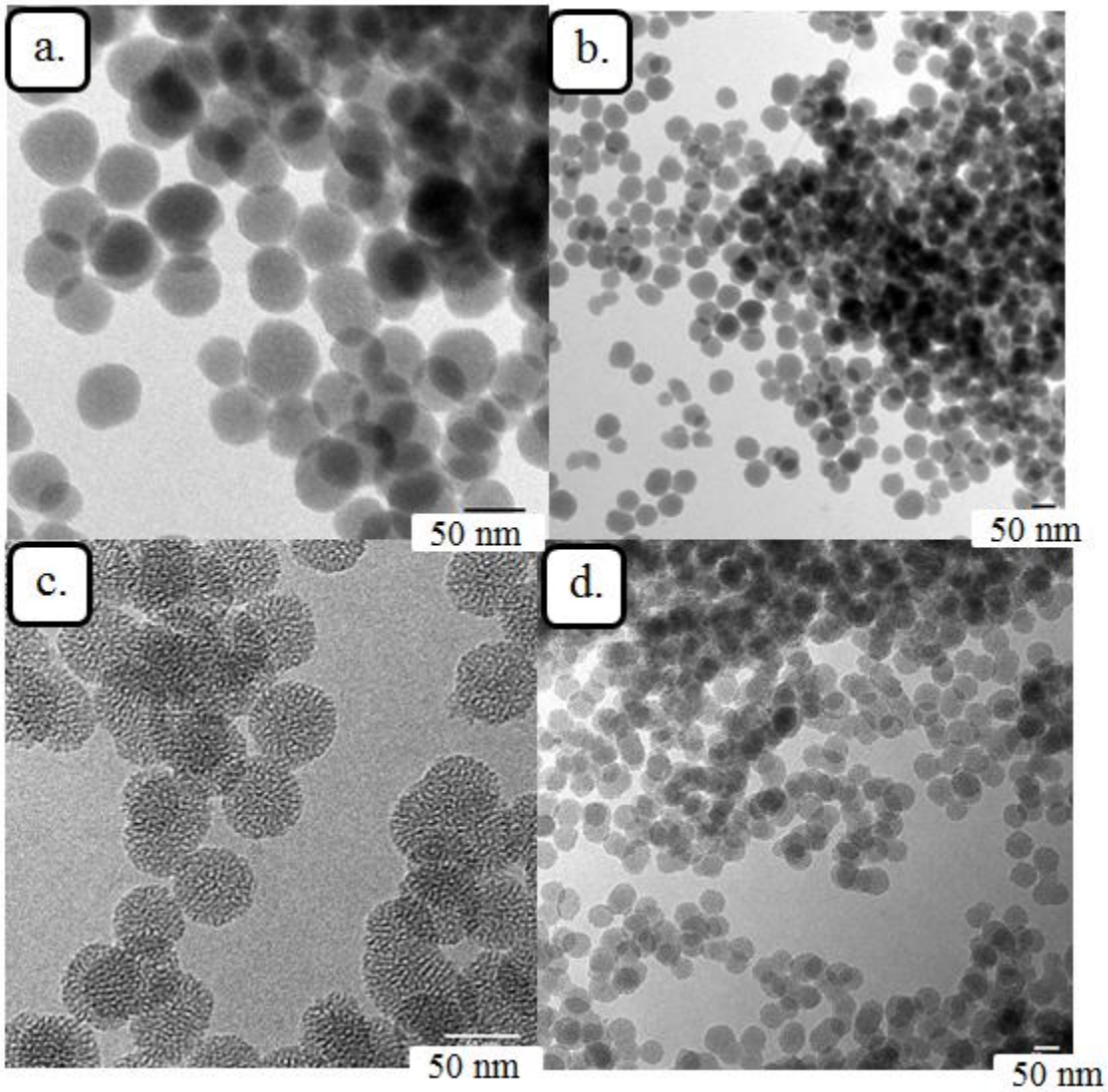

Figure 16 TEM images of nonporous silica (a,b) and mesoporous silica (c,d). The wormhole pore structure can clearly be seen in image c.

CHAPTER 3: INCORPORATION OF GERMANIUM INTO THE FRAMEWORK OF NANOCRYSTALLINE FAUJASITE

3.1. Introduction

Zeolites are well-studied microporous materials with numerous applications due to their highly customizable properties such as acidity, ion exchange capacity, and selectivity [87]. While a number of zeolites are naturally occurring, many more have been synthesized in the laboratory. Zeolites have a framework consisting of SiO_4 and AlO_4 tetrahedra that can be arranged in different ways giving rise to a large range of framework types. In addition to aluminosilicate zeolites, additional zeolites can be created by incorporating other elements, such as germanium, gallium, phosphorous and transition metals, such as titanium, into the framework.

Faujasite (FAU) type zeolites have a pore size of 7.4 Å and have many practical applications as adsorbents, ion exchangers, and catalysts. The FAU framework is shown in Figure 17. Zeolites X and Y are FAU type zeolites which differ in Si/Al ratio. Zeolite X has a Si/Al between 1 and 1.5 and zeolite Y has a Si/Al greater than 1.5. Zeolite A has the LTA (Linde Type A) structure and a 4.2 Å pore diameter. In the last decade, much research has focused on synthesizing zeolite crystals with nanoscale dimensions[88, 89]. Nanocrystalline zeolites have improved catalytic activity, increased external surface areas, and decreased diffusion path lengths relative to conventional micron sized zeolites. FAU nanocrystals are synthesized in a clear aluminosilicate gel in the presence of an organic template and a sodium cation source. In order to favor conditions that lead to nanocrystalline FAU zeolite growth, a supersaturated solution is utilized in order to generate the maximum number of nucleation sites. This is because, as the number of viable nuclei in a closed nutrient pool increases, crystal size decreases. The synthesis of pure zeolite X is complicated by the fact that zeolite A forms under similar reaction conditions, so that typically a mixture of zeolites X and A results[90]. A recycling procedure has been implemented to improve the nanocrystalline FAU zeolite yield[91-93].

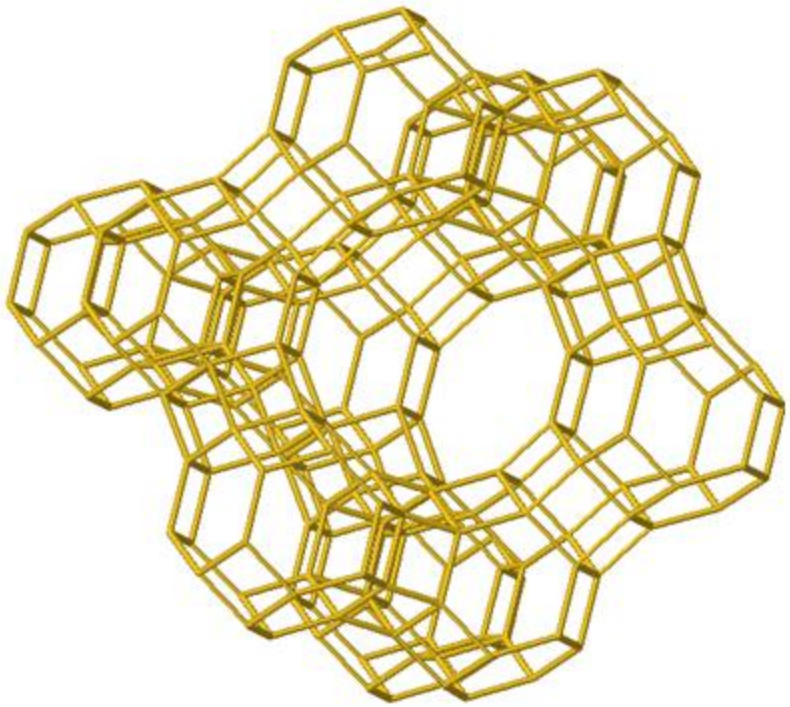

Figure 17 FAU framework type zeolite. Each intersection represents a tetravalent silicon or aluminum atom connected by oxygen atoms to form the aluminosilicate framework. The oxygen atoms are not shown.

Studies involving germanium substitution in zeolites have primarily focused on the role of germanium as a structure directing heteroatom towards forming new zeolite structures and modifying the dimensions of well-known zeolites (eg. framework expansion)[94-105]. The incorporation of germanium allows for the stabilization of zeolite structural units with acute bond angles, such as double three and four membered rings and this has been used in unison with novel organic structural directing agents to produce the ITQ zeolites[98, 99, 106]. In addition to the role of germanium as a structural directing agent, germanium incorporation into the framework of zeolites has been shown to facilitate the photochemical generation of electrons and holes, and therefore the possibility of using such zeolites in photovoltaic cells, light sensitive catalysts, and photoresponsive materials[107].

In the study reported here, a method for the formation of nanocrystalline FAU zeolite with framework germanium was investigated. The greater atomic radius of germanium compared to silicon allows for a higher degree of framework flexibility. The synthesis strategy utilized in this chapter demonstrates that it is possible to recycle the zeolite reaction mixture in order to generate low silica FAU type nanocrystalline zeolites with crystal sizes of approximately 50 nm, consistent germanium incorporation and high purity as shown in the schematic in Figure 18. This work represents the first synthesis of germanium containing nanocrystalline FAU type zeolites from clear solutions utilizing recycling to increase product yield and improve the environmental impact of the synthesis.

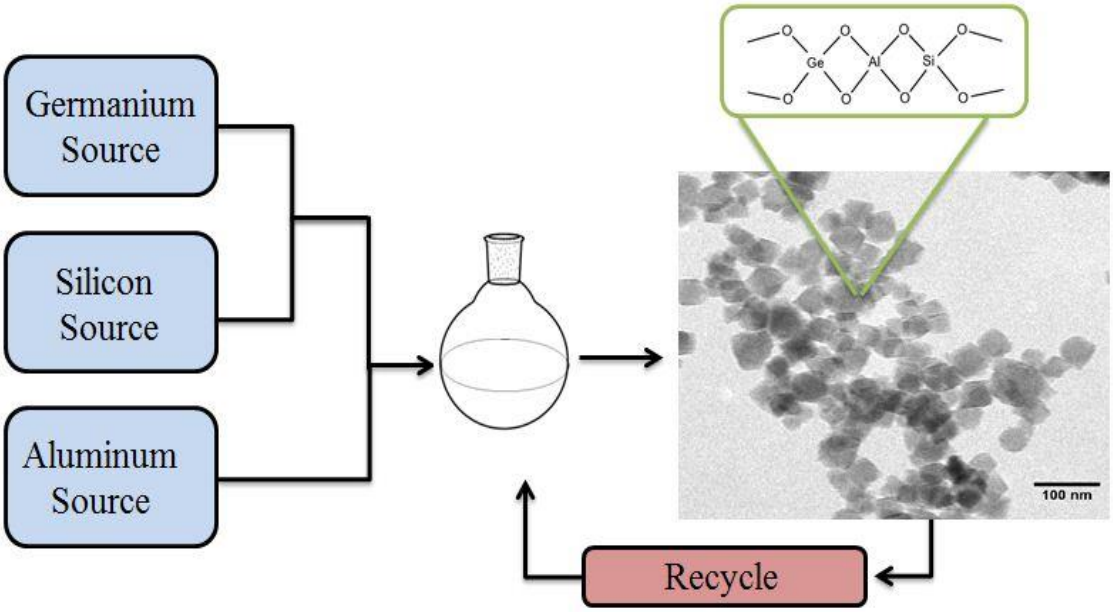

Figure 18 General procedure for the production of germanium incorporated FAU type zeolite utilizing recycling to increase the overall yield

3.2. Experimental Section

3.2.1. Synthesis of Germanium Substituted Zeolite X

Tetraethyl orthosilicate (TEOS), tetramethylammonium hydroxide (TMAOH), germanium dioxide, sodium hydroxide, and aluminum isopropoxide (AIP) were purchased from Sigma Aldrich. Nanoscale zeolites were prepared from clear reaction mixtures with and without germanium as depicted schematically in Figure 19 and using the molar ratios provided in Table 2. Solutions containing silicon, aluminum, and germanium were prepared separately and were then mixed to form a clear reaction mixture that was aged and heated to give a crystalline zeolite product. In a typical synthesis of germanium containing FAU zeolite, germanium dioxide was mixed with TMAOH. A silicon source solution was prepared by combining TEOS and TMAOH and an aluminum source solution was prepared by mixing AIP with water, sodium hydroxide, and TMAOH with stirring until the solution was clear. The germanium and silicon source solutions were combined and stirred for 10 mins before being added to the aluminum solution to form a clear reaction mixture that was aged for 12 h with stirring. The resulting solution was heated in an oil bath equipped with a water-jacketed condenser at 97 °C for 72 hours until the solution became slightly opaque. A control batch prepared without any germanium was synthesized as a control for comparison with the germanium-containing products.

The solid product was collected with centrifugation at 20800 rcf and the supernatant was recovered. The solids were resuspended in water and then centrifuged again followed by washing with water and then ethanol before being dried at 105 °C overnight. The solid product was calcined at 550 °C for 8 hours in air. Meanwhile, the supernatant was recycled in two separate series by either adding: A) 1 M NaOH (0.04 ml/ml reaction mixture) or B) both 1 M NaOH (0.04 ml/ml reaction mixture) and germanium dioxide (1 mg/ml reaction mixture) to the supernatant and stirring for one hour. The recycled reaction mixture was then heated to 97 °C for 18 hours until the solution became opaque. The solid product was collected as described above and the supernatant was recycled several more times. Cumulative product yield is

calculated by dividing the dry/calcined yield by the theoretical yield with the silicon source as the limiting reagent.

Table 2 Molar ratios of solutions in initial reaction mixture

	Solution	TEOS	GeO_2	AIP	Water	NaOH	TMAOH
Germanium Containing	Ge Solution	--	0.096	--	--	--	0.58
	Si Solution	2.34	--	--	--	--	1.5
	Al Solution	--	--	1.41	261.25	0.045	1.5
Control	Si Solution	2.34	--	--	--	--	1.74
	Al Solution	--	--	1.41	261.25	0.045	1.74

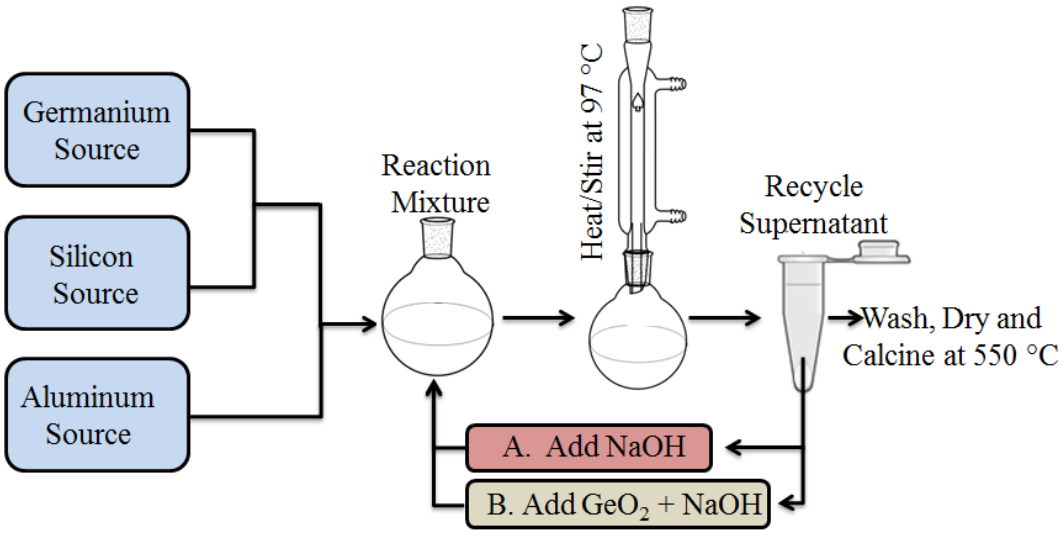

Figure 19 Synthesis of FAU type zeolites. In the recycling step, either A) NaOH or B) both GeO_2 and NaOH were added to the collected supernatant and stirred before being heated at 97 °C. This recycling is repeated several times.

The initial solid product is labeled as GeX-AB0 and the supernatant from this experiment was divided into two separate series, A and B, in which the germanium containing zeolites were recycled by A) adding NaOH or B) adding both NaOH and germanium oxide. These two series are referred to as *GeX-A#* and *GeX-B#*, respectively, where the number refers to the recycle batch number and A and B refer the the two series. The control sample was synthesized without any added germanium and is labeled as *Control*.

3.2.2 Characterization

Elemental analysis by Inductively Coupled Plasma-Optical Emission Spectroscopy (ICP-OES) was performed with a Varian 720-ES instrument. The samples were digested by adding ~5 mg of dry/calcined product to a 30:70 solution of concentrated HF:HCl (1.6 ml). The solution was sonicated until clear. Nitric acid (0.4 ml) and 5% boric acid (6 mL) were added and the total volume was brought to 10 ml with deionized water. The samples were then analyzed by ICP-OES (1.0 kW, argon flow 0.05 L/min) and the elemental ratios were calculated. Powder X-ray diffraction (XRD) patterns were collected over a range of $2\theta = 5\text{-}55°$ on a Siemens D500 X-ray diffractometer (0.04 step size with a step time of 1 second per step). The powder XRD patterns were used to determine relative crystallinity and purity. The samples were imaged using Transmission Electron Microscopy (TEM) with a JEOL 1230. The dry products were suspended in ethanol and sonicated for 30 min before being dropped onto formvar-coated 400 mesh copper grids. The particle sizes were analyzed with Image-J software. Surface area analysis was accomplished using a Quantachrome NOVA 1200 Surface Area Analyzer with the samples being outgassed at 120 °C for 4 hours prior to analysis. Silicon and aluminum nuclear magnetic resonance (NMR) experiments were conducted on a Bruker Avance III-500 MHz spectrometer using 4.0 mm and 2.5 mm double resonance CP/MAS probes, respectively. ^{27}Al and ^{29}Si Magic Angle Spinning (MAS) NMR experiments were conducted on representative zeolite samples. $AlCl_3$ was used as a chemical shift reference for ^{27}Al NMR. The magic angle spinning speeds were 30 kHz and 10 kHz for ^{27}Al and ^{29}Si experiments, respectively.

Table 3 Elemental analysis, surface area, and size of germanium containing zeolites

Sample	Recycling Batch	Si/Ge Ratio[a]	Si/Al Ratio[a]	S_A (m^2/g)[b]	Size (nm)[c]	Cumulative Product Yield (%)	Purity (% FAU)[d]
GeX	0	24(0)	1.4(0.0)	393(3)	35(9)	2	96
GeX-A1	1	19(0)	1.3(0.0)	683(5)	33(8)	15	100
GeX-A2	2	25(0)	1.3(0.0)	572(4)		35	95
GeX-A3	3	29(0)	1.3(0.0)	458(3)		51	96
GeX-A4	4	45(0)	1.3(0.0)	439(3)		61	41
GeX-A5	5	97(0)	1.3(0.0)	248(2)		62	32
GeX-B1	1	16(0)	1.3(0.0)	500(4)	34(8)	9	100
GeX-B2	2	19(0)	1.3(0.0)	641(4)		24	94
GeX-B3	3	17(0)	1.3(0.0)	534(4)		37	100
GeX-B4	4	18(0)	1.3(0.0)	416(3)		44	80
GeX-B5	5	23(0)	1.3(0.0)	293(2)		47	40
Control	1	N/A	1.5(0.0)	547(4)	36(12)	12	12

a. measured by ICP-OES

b. measured by nitrogen adsorption and the BET method; error given in parenthesis

c. determined from TEM; standard deviation given in parenthesis

d. determined from pXRD calibration

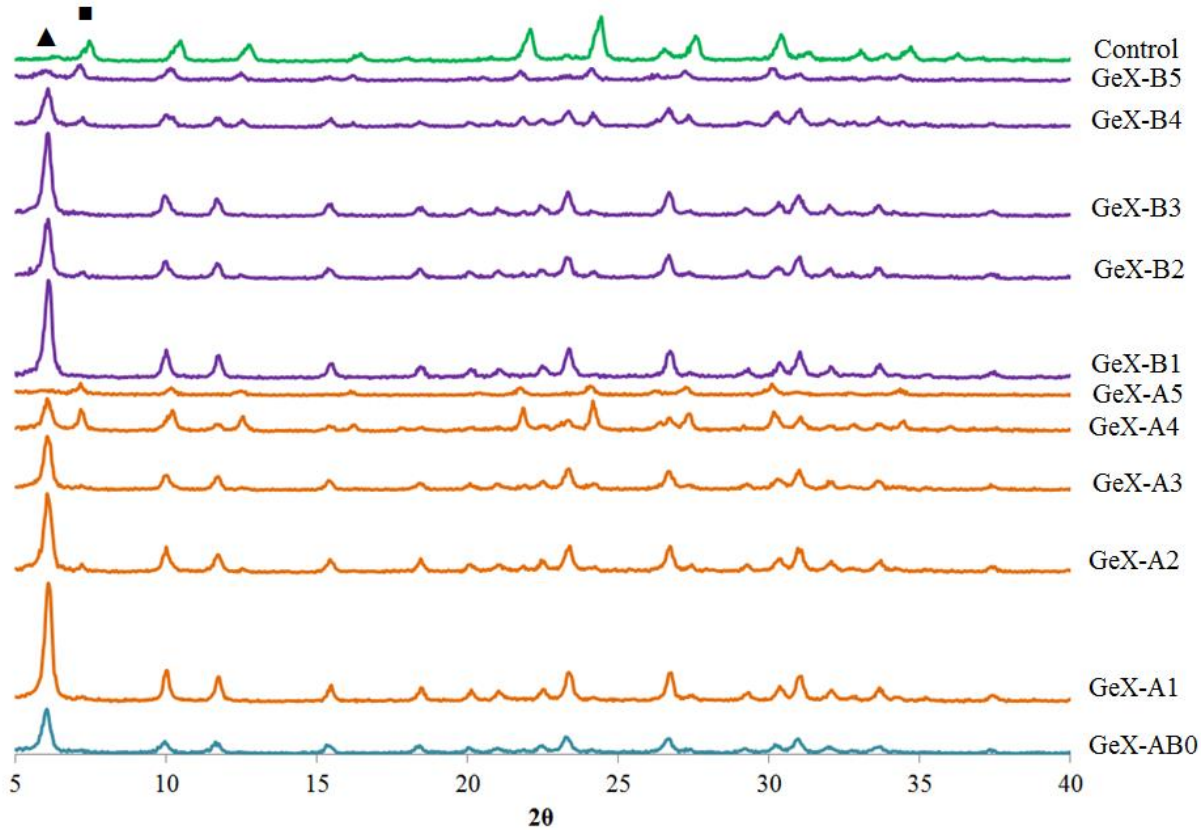

Figure 20 p-XRD patterns of the initial product and the A) NaOH recycled zeolites (GeX-A#) and B) GeO_2+NaOH (GeX-B#) recycled zeolites where #=batch number. A p-xrd of the control synthesized without any added germanium is also included as the top patter. They symbol ▲ represents a major XRD peak from FAU framework type zeolite and ■ indicates xrd peaks indicative of LTA.

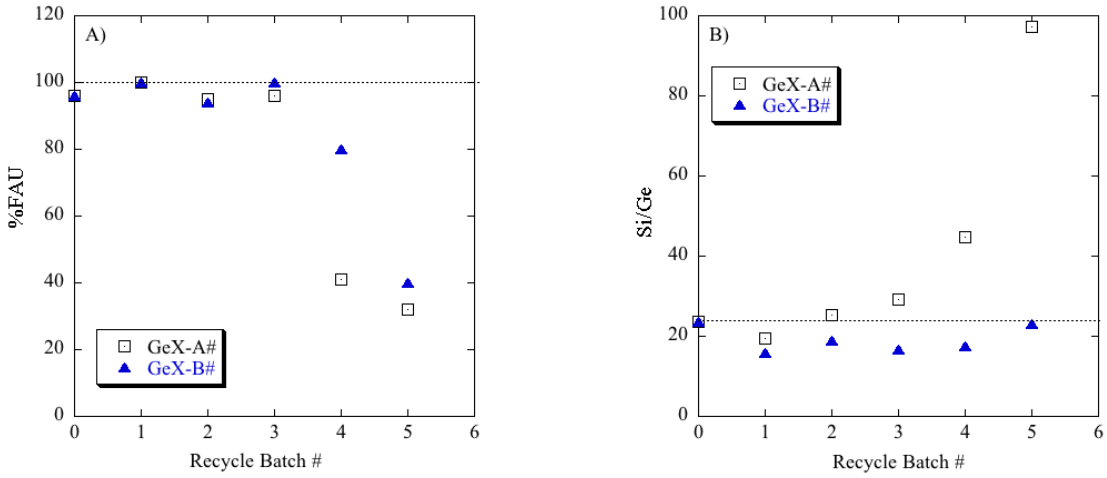

Figure 21 Graph showing A) the % FAU and B) the Si/Ge in the product both as a function of the batch # and series. In series A, only NaOH was added to subsequent batches and in series B, both GeO_2 and NaOH were added to subsequent batches. The series were synthesized in parallel by splitting the first recycle into two separate series. The dashed line indicates A) 100% FAU and B) initial Si/Ge ratio.

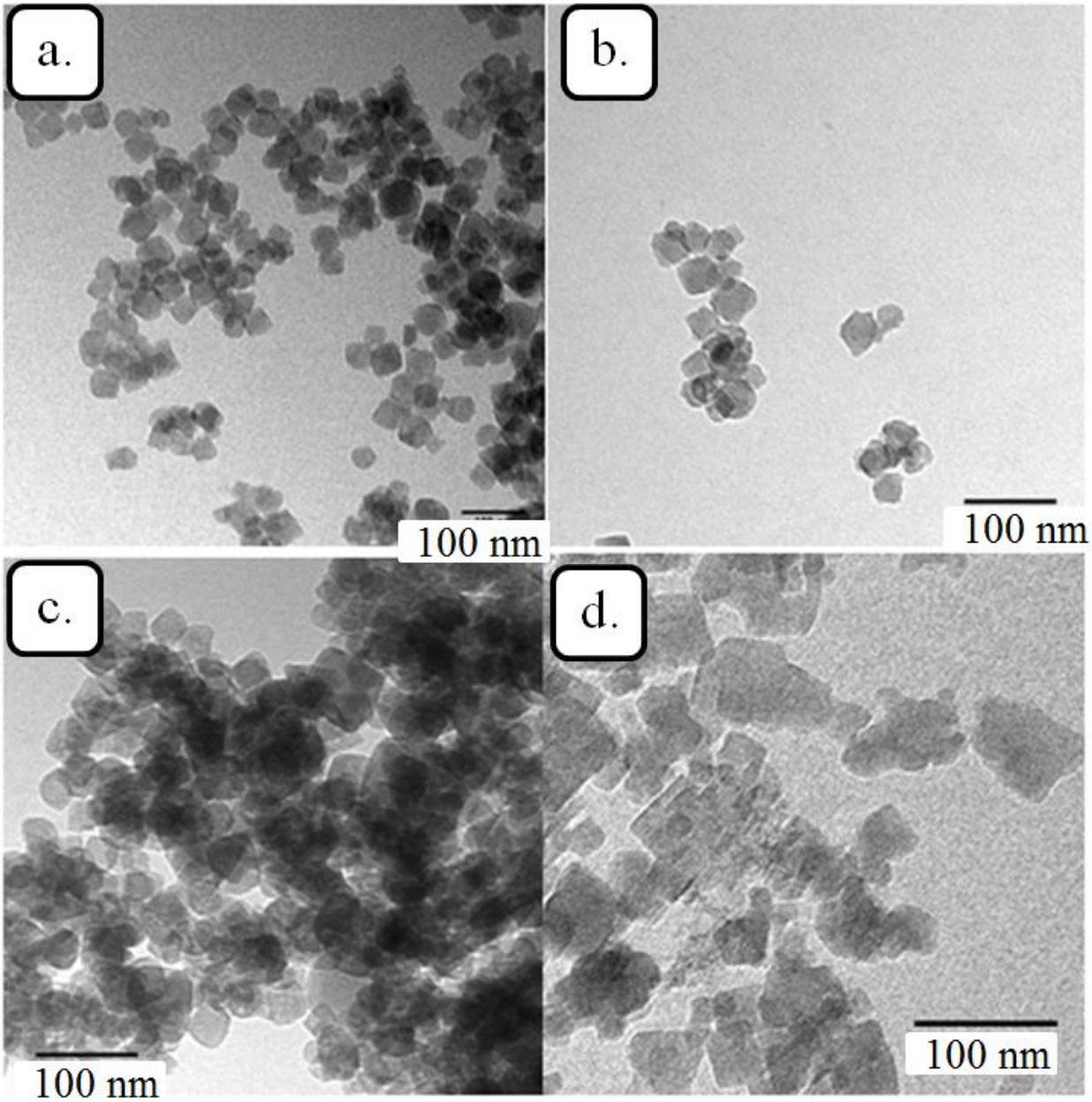

Figure 22 Representative TEM images of GeX-A1 (top left), GeX-B1 (top right), Parent (bottom left), and the control (bottom right)

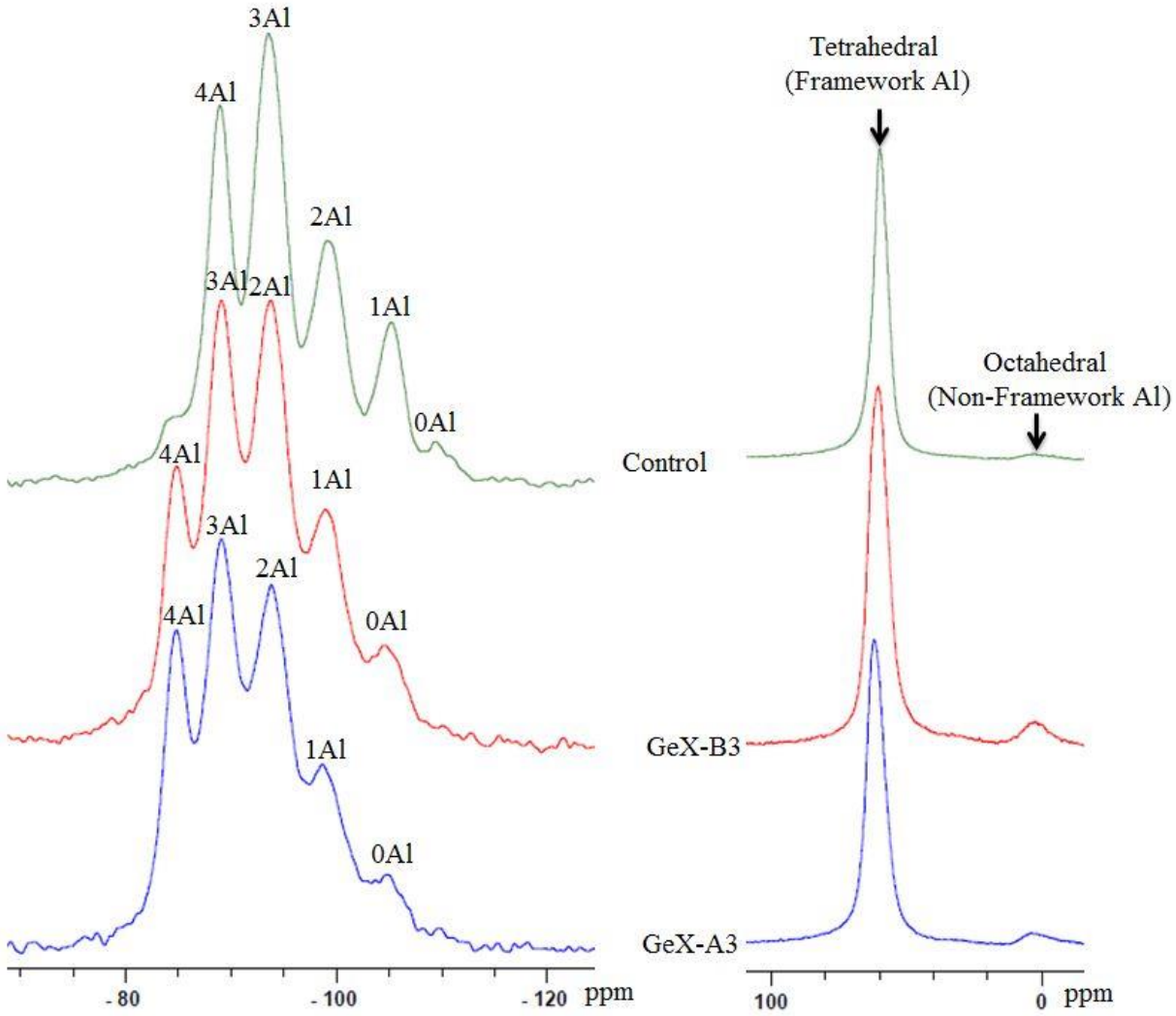

Figure 23 ^{29}Si (left) and ^{27}Al NMR (right) spectra of representative samples from GeX-A, GeX-B3, and Control-C2 respectively from bottom to top.

Table 4 ^{29}Si MAS NMR Peak Assignments

Sample	Si(4Al)	Si(3Al)	Si(2Al)	Si(1Al)	Si(0Al)
GeX-A	-85.2	-89.1	-93.9	-98.8	-105.0
GeX-B	-85.1	-89.1	-94.0	-99.0	-105.0
Control	-88.0	-93.9	-98.8	-105.1	-108.9

3.3. Results and Discussion

Nanocrystalline germanium-substituted X zeolites were prepared using a modified recycling procedure as depicted in Figure 19 and originally developed for synthesis of nanocrystalline NaY[89, 91]. After the first batch of zeolite was separated by centrifugation, the supernatant was recycled and used in subsequent batches. NaOH or both NaOH and germanium oxide were added to the recycled supernatant and are labeled as samples A and B, respectively. A control batch without any germanium was also synthesized for comparison. Each batch was characterized by powder XRD (p-XRD) and ICP-OES. Selected batches were also analyzed by solid state NMR, TEM, and nitrogen adsorption.

p-XRD patterns for the germanium-containing zeolites and the control zeolites are shown in Figure 20. A common impurity in the syntheses of FAU zeolites, X and Y, is zeolite LTA. Both FAU and LTA type zeolites share similar but slightly offset p-XRD peaks. The characteristic peaks used for identification of the FAU and LTA phases are indicated with filled triangles and squares, respectively, in Figure 21. FAU type zeolite has a major characteristic peak at 2θ~6.10° indicated by a triangle symbol and LTA has a major characteristic peak 2θ~7.20° indicated by a square symbol. Qualitatively, it was observed that the germanium containing samples, A1-A4 and B1-B5 contain mainly the FAU phase along with a smaller but variable amount of LTA. Alternatively, the control samples prepared without germanium contained primarily LTA zeolite.

In order to quantify the relative amounts of FAU and LTA phases, physical mixtures of standard samples of FAU and LTA type zeolites were prepared and analyzed by p-XRD. A calibration plot was constructed to relate the characteristic p-XRD peak intensities to relative FAU/LTA composition by weight percent. The least squares best fit linear parameters were used to calculate the relative percentage of FAU produced in each batch of the synthesized samples as presented in Table 3 and graphed in Figure 21. Based on this calibration, the initial zeolite product in both germanium containing zeolite batches (A1 and B1) predominantly contained ~100% FAU type zeolite as can be seen from the major peak at 2θ~6.10° and the absence of the

LTA peak at 2θ~7.20°. In the subsequent recycling, the GeX-A4 and A5 and GeX-B4 and B5 samples showed a marked decrease in FAU phase relative to LTA as can be clearly seen in Table 3. In the control sample synthesized without germanium, the product was primarily LTA zeolite with only ~12% FAU as shown by the pXRD pattern in Figure 20. For the first batch of nanocrystalline zeolite, the presence of germanium in the reaction mixture leads to 96% FAU compared to 12% in the absence of germanium for an otherwise identical reaction mixture. However, for subsequent batches the trend is not so clear in that a decrease in FAU purity is observed for both series A and B. Other factors such as the declining concentration of template also effect the FAU purity but were not investigated in this study.

ICP-OES was used to determine the relative amounts of silicon, aluminum and germanium in the zeolite samples. The results are listed in Table 3 and graphed in Figure 22. For the A series, as the germanium containing reaction mixture is recycled with only added NaOH, the Si/Ge ratio increases from 24 to 97 indicating a decrease in the germanium content for subsequent recycled batches. This was remedied in the B series by adding small quantities of germanium oxide to the reaction mixture before each recycling. This addition of germanium results in a Ge/Si ratio ranging from 16 to 24 with an average value of 20. The Si/Al ratio as calculated by ICP-OES ranges from 1.3 to 1.4 which is in the range of Zeolite X (Si/Al of 1-1.5).

The BET method was used to calculate the specific surface area of the samples. The majority of the calcined GeX-A and GeX-B zeolites had surface areas ranging from 293-683 m^2/g as listed in Table 3. These high surface areas are typical of crystalline zeolite materials as reported elsewhere[91, 108].

The overall yield listed in Table 3 is approximately 62% and 47% after 5 recycles for both the A and B series, respectively. In general, the amount of zeolite product obtained from the initial synthesis was negligible and only yielded a small (<3%) amount of product. Subsequent recyclings typically yielded significantly more product (usually >10% total theoretical yield per recycling). These results are similar to those observed in the synthesis of nanocrystalline zeolite Y by recycling [91].

TEM images were acquired for several of the zeolite samples to determine the crystal size and morphology. Representative TEM images are shown in Figure 21. The sizes determined from the TEM images using image analysis software are provided in Table 3 along with the standard deviations. The sizes for the samples analyzed by TEM are 35(9), 33(8) and 34(8) nm for GeX-AB0, GeX-A1 and GeX-B1, respectively, which are similar when taking into account the standard deviations of the measurements. For the sample prepared in the absence of germanium, the crystal size from TEM was 36(12) nm.

The ^{27}Al and ^{29}Si MAS NMR of representative samples from the A and B series and the Control sample are shown in Figure 22. The ^{27}Al MAS NMR spectra all contain a large peak at ~60 ppm assigned to tetrahedrally coordinated aluminum species and a very small peak at 0 ppm assigned to octahedrally coordinated aluminum. Taken together, these spectral peaks indicate that the majority of aluminum in the crystalline zeolite material is in tetrahedral coordination within the zeolite framework while there is a relatively small amount of octahedrally coordinated extraframework aluminum. The ^{29}Si NMR spectra of the zeolite products contain peaks which are assigned to Q4(4Al), Q4(3Al), Q4(2Al), Q4(1Al), and Q4(0Al) as listed in Table 4 [109, 110]. Both GeX zeolites studied had similar peak assignments for Q4(4Al) through Q4(0Al) while the peaks for the control sample were slightly shifted. This is mainly attributed to the fact that the control sample had mainly the LTA type framework with only ~12% FAU [111, 112] . The small shoulder at ~-85 is attributed to Q4(4Al) for FAU whereas the other peaks are assigned to Q4 peaks for LTA as listed in Table 4. Using the peak assignments in Table 4 and the peak intensities from the ^{29}Si MAS NMR spectra in Figure 22, the Si/Al ratio of the samples was calculated using equation 1 below.

$$\frac{Si}{Al} = \frac{\sum_{n=0}^{4} I_{\mathrm{Si}(n\mathrm{Al})}}{\sum_{n=0}^{4} 0.25n\, I_{\mathrm{Si}(n\mathrm{Al})}} \quad [1]$$

In Equation 1, I is the signal intensity of the specific resonance of framework silica and n is the number of Al tetrahedra that are coordinated to that resonance of silica [110]. For the control,

the equation agrees well with the ICP-OES data, giving a Si/Al ratio of 1.5. However this calculation based on the Si NMR data gives a Si/Al ratio of 1.7 for GeX-A and 1.6 for GeX-B as compared to 1.4 and 1.3, respectively, as determined by ICP-OES. This variation could be due to the fact that the germanium containing zeolites appear to have slightly more extraframework or octahedral aluminum than the control sample leading to a higher Si/Al ratio based on the concentrations of tetrahedral silicon and aluminum only. It is also possible that the presence of germanium changes the relative intensities of the silicon NMR peaks and/or shifts the peaks due to the influence of germanium on the silicon chemical shift. This could lead to an underestimation of the tetrahedral aluminum in a germanium-containing sample which results in a higher calculated Si/Al value.

The addition method was most effective for the addition of germanium into the zeolite framework. It appears that the germanium stabilizes the formation of FAU type zeolite as the FAU purity of the product is seen to drop when the silica/germanium ratio increases. Germanium seems to have an important role in the formation of FAU type zeolite under these conditions.

The stabilizing influence of the Ge could be in part due to the larger atomic radii as compared to Si. This increased radii allows Ge atoms to stabilize smaller X-O-X angles (where X=Ge, Al, or Si) [100]. Energetically, the formation of 6 membered rings are favored and these rings connect form double 6 membered rings (D6Rs); however, at high levels Al atoms double 4 member ring formation is increasingly favored which results in LTA zeolites. Ge could be expected to further promote the formation of LTA over FAU because, as previously mentioned, Ge is known to stabilize smaller angles such as those found in four membered rings. However, from Figure 17, 4 membered rings are also a part of the FAU framework. The presence of germanium could allow the energetically favored 6 membered rings to more easily form the double 6 membered rings. As LTA depends on the presence of D4Rs which form more slowly and are energetically unfavorable compared to D6Rs, the germanium can stabilize the formation of the D6Rs preferentially in the initial solution. The sodelite cages in figure 17 are formed of

the four membered rings in solution joining into 6 membered rings. Together, these steps deplete the supply of 4 membered rings in solution required to form the unwanted D4Rs and promote the formation of FAU over LTA in the initial synthesis conditions.

3.4. Conclusions

While germanium has been previously substituted for silicon in FAU type zeolites, this work represents the first time germanium containing FAU type zeolites with nanoscale crystal sizes were obtained through recycling of a clear reaction mixture. The recycling method with replenishment of NaOH and GeO_2 was demonstrated to be an efficient method for preparing germanium substituted faujasite zeolites with high crystallinity, good product yields, and consistent batch to batch germanium substitution. Nanocrystalline zeolites synthesized with the same Si/Al ratio with the same reaction conditions but in the absence of germanium produced a mixture of zeolite X and zeolite A, indicating that germanium substitution allows for an increased number of Al sites within nanocrystalline FAU type zeolite synthesized from clear reaction mixtures.

CHAPTER 4: HIGH YIELD SYNTHESIS OF IRON OXIDE/MESOPOROUS SILICA CORE/SHELL NANOPARTICLES

4.1. Introduction

Mesoporous silica has proven an incredibly useful material with applications in areas such as catalysis, environmental remediation, medical imaging, adsorption, and drug delivery [35, 36, 60, 74, 113-119]. These applications are made possible by the large surface area, controllable pore diameter, low toxicity, and readily modifiable surface chemistry of mesoporous silica materials. Mesoporous silica nanoparticles have gained much attention due to their larger and more accessible surface area, as well as improved biocompatibility relative to mesoporous silica with micron particle sizes [120, 121]. Of particular interest has been the combination of mesoporous silica nanoparticles and other metal or metal oxide nanoparticles to create core/shell nanomaterials [61, 116, 120, 122, 123].

In this study, various conditions for the synthesis of magnetic iron oxide core/shell mesoporous silica nanoparticles were explored. Iron oxide in the form of magnetite (Fe_3O_4) was chosen as the core because magnetite nanoparticles have been and continue to be a topic of interest in the materials research community [55, 62, 124, 125]. Magnetite nanoparticles are among the most well studied owing to their interesting magnetic properties, relatively simple synthesis conditions, and low cost. The magnetic susceptibility of iron oxide nanoparticles is one of the material's most important properties, allowing the nanoparticles to be readily manipulated and recovered using magnetic fields[55, 126], as well as imparting great potential for drug delivery and medical imaging applications[55, 65]. However, magnetic iron oxide nanoparticles also tend to suffer from aggregation resulting in loss of magnetic capacity, accessible surface area, and dispersibility. Consequently this has led to the development of stabilization strategies such as coating the iron oxide nanoparticles with mesoporous silica [61, 65, 116, 127, 128]. This class of core/shell nanomaterials has many useful qualities and has quickly become a focus of materials research.

Iron oxide/mesoporous silica core/shell nanoparticles are composed of an iron oxide core embedded within a shell of mesoporous silica. These nanoparticles combine the useful properties of mesoporous silica with those of iron oxide resulting in a truly versatile material. These iron oxide/mesoporous silica core/shell nanoparticles have many potential applications in drug delivery, medical imaging, catalysis, and environmental remediation [38, 60-62, 65, 67]. The properties of the iron oxide core/shell mesoporous silica nanoparticles can be tuned for a specific application by modifying mesoporous silica properties, such as silica shell thickness, pore size, pore wall thickness, and size of the nanoparticles. Many applications benefit from a total particle diameter of less than 100 nm. For example, studies have shown that for biomedical applications including drug delivery, maximum uptake is achieved for mesoporous silica nanoparticles having a total particle size of less than 100 nm[38, 120, 129].

There have been many studies on the synthesis and application of iron oxide/mesoporous silica core/shell nanomaterials [67, 74]. In general, prior research has gravitated towards improving control of the size and shape of the pores, incorporating different shapes or forms of iron oxide, and probing potential applications of the core/shell nanoparticles. Notably, Lin and Haynes demonstrated that it was possible to incorporate Fe_3O_4 nanoparticles into mesoporous silica in a one pot synthesis[120]. More recently, Nikola and coworkers demonstrated that the pore structure (radial vs hexagonal) of core/shell mesoporous silica could be tuned by controlling the rate of addition of tetraethylorthosilicate (TEOS) added to the reaction mixture during synthesis [116]. Aerosol assisted synthesis has also been utilized resulting in a high efficiency in terms of iron oxide loading [130, 131]. The resulting core/shell nanoparticles have a homogeneous distribution of iron oxide nanoparticles but a heterogeneous distribution of particle sizes [130, 131]. Zhang and coworkers recently showed that pseudo-cubic iron oxide nanoparticles embedded in mesoporous silica spheres could be synthesized with controlled core/shell thickness and surface area [62]. While there have been many advances in the synthesis of iron oxide core/shell mesoporous silica nanocomposites, previous studies generally use dilute synthesis conditions which limit the amount of product produced and generate large

amounts of waste[120, 127]. Additionally, previously reported methods tend to require surface modified or pre-coated iron oxide nanoparticles[120, 127]. A major problem still facing this area of research is the scaling up of the process to produce large amounts of uniform core/shell nanocomposites, thereby improving the environmental impact by reducing waste and decreasing the cost and time required.

In this study, a scalable, high yield, and greener synthesis of sub 100 nm core-shell iron-oxide mesoporous silica nanocomposites with wormlike (WO) pore morphology was developed. The starting point for the synthesis conditions was a recent study in which large quantities of monodisperse WO mesoporous silica nanoparticles were produced using various secondary organic amines (SOAs) [132]. These synthesis conditions were modified to include an iron oxide core in a one-pot synthesis that produced multi-gram scale yields of discrete, monodisperse, and easily dispersible iron oxide/mesoporous silica core/shell nanoparticles starting from dry unmodified iron oxide nanoparticles. The role of the SOA in the synthesis of the core/shell nanomaterials was investigated by varying the amount as well as the identity of the SOA. This research works toward a simple, high yield synthesis of large quantities of monodisperse, sub 100 nm iron oxide/mesoporous silica core/shell nanoparticles with high surface area, controllable size, and well-formed mesopores with wormlike (WO) morphology.

4.2. Experimental Section

4.2.1. Synthesis of Fe_3O_4 Nanoparticles

Spherical Fe_3O_4 nanoparticles ~13 nm in size were synthesized using a modified version of a previously reported method[120, 133]. 4.80 g of iron(III) chloride hexahydrate and 2.00 g iron(II) chloride tetrahydrate were added to 30 ml of nitrogen purged water. The solution was stirred and heated to 90 C° under a nitrogen atmosphere with magnetic stirring at 500 rpm. 20 ml of 14% aqueous ammonia was added to the amber solution which then turned black, and the reaction was allowed to continue stirring and heating at 500 rpm and 90 C° respectively for 2.5 hours. The product was collected with a magnet and washed with water until the pH of the rinse

water was approximately 7.0. The product was dried at 100 C° for 4 hours and stored in a glass vial. The product is magnetic and was used in the following reactions with no further modification.

4.2.2. Synthesis of Iron oxide Core/Shell Mesoporous Silica Nanoparticles

Using a co-precipitation method, either cetyltrimethylammonium chloride (CTACl) or cetyltrimethylammonium bromide (CTAB) was added to water as a surfactant and stirred before adding a small organic amine (SOA). The SOA used was either triethanolamine (TEA) or 2-amino-2-(hydroxymethyl)propane-1,3-diol (Tris). The dry Fe_3O_4 nanoparticles were added to this solution without any post-synthesis surface treatment. The TEOS was used as received without any additional purification or distillation. The identity and amounts of reactants used are listed in Table 5.

Table 5 Reaction conditions of samples described in text as molar concentrations of reagents

Name	TEOS	SOA	Surfactant	Water	Ethanol	Fe_3O_4
M-MSN-1	1	0.5(TEA)	0.3(CTACl)	151	8	0.04
M-MSN-2	1	0.7(TEA)	0.3(CTACl)	144	8	0.04
M-MSN-3	1	1(TEA)	0.4(CTACl)	198	10	0.11
M-MSN-B	1	0.1(TEA)	0.1 (CTAB)	81	0	0.07
M-MSN-T	1	1(Tris)	0.1(CTACl)	165	0	0.05

In a typical synthesis, 360 ml water, 60 ml ethanol (EtOH) and 59 ml of a 25% by weight CTACl solution were combined and stirred for 10 mins. 9 ml of TEA was added to the solution and stirred for 2 hours. 1.18 g Fe_3O_4 nanoparticles were added to the solution and the resulting suspension was sonicated 1 hour at 42 kHz. The resulting suspension was then mechanically stirred and heated to 60 C° and 29.6 ml of TEOS was rapidly added. The reaction mixture was mechanically stirred at 500 rpm for 2 hours at 60 C° resulting in a deep brown suspension. The

slightly viscous suspension was then allowed to cool before the core-shell product was separated by large scale high speed centrifuge. The post-centrifuged product was washed with water and separated with a magnet until the pH of the rinse water was approximately 7.0. The resulting product was dried at 100 C° in an oven and calcined with air flow at 550 C° for 5 hours yielding approximately 2.2 grams of iron oxide core/shell worm-like (WO) mesoporous silica nanoparticles.

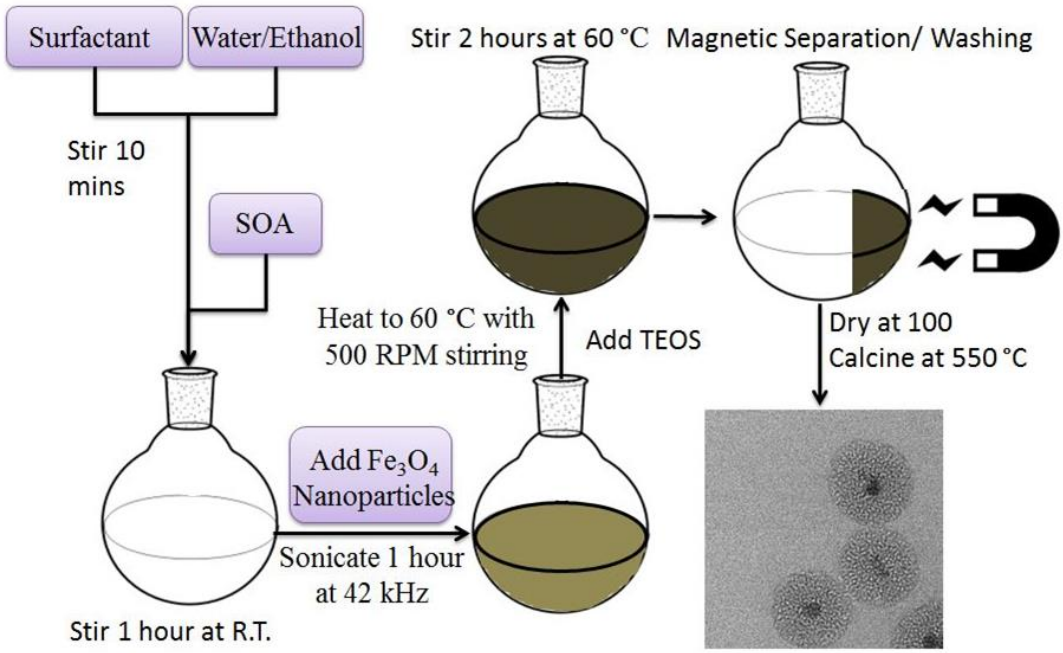

Figure 24 Flow chart of synthesis procedure for M-MSN core-shell nanoparticles.

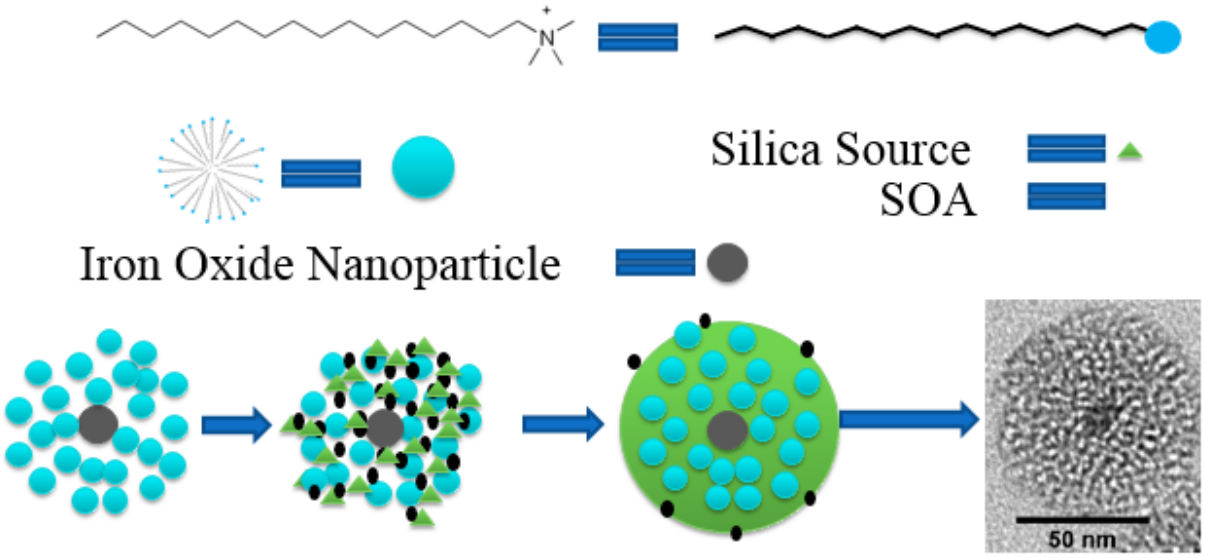

Figure 25 Schematic diagram of the formation of M-MSN core-shell nanoparticles with WO pore morphology.

Several variations of the above procedure were employed to generate variants of the core/shell product. The samples were labeled as M-MSN-# for magnetic iron oxide with a WO type mesoporous silica shell synthesized using CTACl as the surfactant, TEA as the SOA, and an ethanol/water solvent system with the # representing a variation of reactant concentrations. M-MSN-B and M-MSN-T were synthesized similarly except that CTAB was used as the surfactant and Tris as the SOA, respectively. The resulting products were characterized with BET, powder X-ray Diffraction (p-XRD), transmission electron microscopy (TEM), and Inductively Coupled Plasma-Optical Emission Spectroscopy (ICP-OES)

4.2.3. Characterization

Elemental analysis by ICP-OES was performed with a Varian 720-ES instrument and was used to determine % Fe in the core-shell materials. The samples were digested by adding ~7.5 mg of dry/calcined product to a 30:70 solution of concentrated HF:HCl (1.6 ml). The solution

was sonicated until clear and 0.4 ml of nitric acid followed by 6 ml of 5% boric acid were added and the total volume was brought to 10 ml with deionized water. The samples were then analyzed by ICP-OES (1.0 kW, argon flow 15 L/min), and the concentration of the sample solutions were calculated. The % Fe was determined by comparing the digested sample masses to the concentrations of the sample solutions. p-XRD patterns were collected at both low and high angles. Low angle and high angle powder patterns were collected over a range of $2\theta = 1\text{-}5°$ and 10-80° respectively on a Siemens D500 X-ray diffractometer (0.04 step size with a step time of 1 second per step). The low angle p-XRD patterns were used to observe the order of the mesoporous silica shell and the high angle was used to observe the iron oxide cores. The samples were imaged using Transmission Electron Microscopy with a JEOL 1230. The dry products were suspended in ethanol and sonicated for 30 min before being deposited onto formvar-coated 400 mesh copper grids. The particle sizes were analyzed with Image-J software using sample sizes of 100 particles. Surface area, pore volume, and pore size were determined by applying BET *(*Brunauer–Emmett–Teller) and BJH (Barrett, Joyner and Halenda) mathematical models to the absorption desorption data from a Quantachrome NOVA 1200 Surface Area Analyzer. The samples were outgassed at 120 °C for 18 hours prior to analysis.

4.3. Results

In this study, sub 100 nm magnetic iron oxide/mesoporous silica core/shell nanoparticles were successfully synthesized from Fe_3O_4 nanoparticles in a one-pot reaction. The schematic diagram of the synthesis procedure is shown in Figure 24 and the complete set of synthesis conditions are listed in Table 5. First, iron oxide (Fe_3O_4), nanoparticles with a diameter of 13±2 nm were synthesized and used in the preparation of the core/shell nanomaterials. Next, gram scale quantities of the iron oxide/mesoporous silica core/shell nanoparticles were quickly and easily produced using relatively inexpensive reagents and co-precipitation methods for the generation of the WO mesoporous silica shell around the iron oxide nanoparticle cores as depicted in Figure 25. This method was modified from a recent study in which large quantities

of monodisperse WO mesoporous silica nanoparticles were produced using various SOAs [132]. The reaction conditions were systematically varied to investigate the effect of changing the amounts of SOA, surfactant, TEOS and iron oxide nanoparticles. In addition, the effects of different SOAs, such as TEA and Tris, were investigated. For the first three samples (M-MSN-1, M-MSN -2 and M-MSN -3), the ratios of TEOS/SOA/surfactant were varied and the amount of iron added was increased for M-MSN-3 relative to M-MSN-1 and M-MSN-2. For the next two samples, the surfactant and the SOA were changed from CTACl to CTAB and TEA to Tris, respectively. A summary of the physicochemical characterization of these materials is provided in Table 6.

Table 6 Physicochemical characterization of samples described in text

Name	TEOS/ SOA	TEOS /Fe_3O_4	%Fe[a]	BET S_A (m^2/g)	BJH_v (cm^3/g)	BJH P_d (nm)	Size TEM	Yield[b] (mg/ml)
M-MSN-1	2.0(TEA)	27	8.1(.2)	812(6)	0.194(.002)	3.2(0.1)	81(14)	4.3
M-MSN-2	1.4(TEA)	27	8.0(.4)	845(6)	0.365(.003)	3.2(0.1)	82(13)	7.8
M-MSN-3	1(TEA)	9	9.5(.3)	794(6)	0.479(.003)	3.2(0.1)	57(8)	13.1
M-MSN-B	37.5(TEA)	76	4.0(.1)	369(3)	0.185(.001)	3.2(0.0)	130(18)	8.7
M-MSN-T	1(Tris)	20.7	8.8(.3)	843(6)	0.381(.003)	3.2(0.1)	87(13)	13.5

[a] % by mass determined by ICP-OES

[b] yield is measured by mg product per ml reaction mixture

The nitrogen adsorption isotherms are shown in Figure 26 and are assigned as type IV isotherms which are indicative of mesoporous materials [134]. Analysis of the nitrogen adsorption/desorption branches of the M-MSN-1,2,3 series and M-MSN-T gave surface areas greater than 790 m^2/g and consistent pore sizes of ~3.2-3.3 nm in diameter as calculated by the desorption branch of nitrogen isotherms utilizing the BJH method (Table 6). Elemental analysis by ICP-OES indicates that the amount of iron in the M-MSN-1,2,3 series and M-MSN-T series of samples ranged from ~8-9.5% as listed in Table 6. The outlier sample was M-MSN-B which

had a substantially lower surface area of 369 m^2/g and a lower Fe content of 4% by weight relative to the other samples.

Low angle p-XRD patterns (Figure 27 top) indicate the presence of mesoporous silica by virtue of broad peaks at ~1.9 2θ [120]. The broadness of the peaks is due a lack of long range order which is indicative of both small particle size and disordered pore structure that is present in WO type mesoporous silica. The effect of particle size on the p-XRD patters is apparent in the increased broadening in M-MSN-3 compared M-MSN series products having larger particles sizes. As the high angle p-XRD patterns in Figure 27 indicate, iron oxide is clearly present in all M-MSN series samples.

The TEM images for representative particles from each sample are shown in Figure 28 and were used to determine the size and morphology of the nanoparticles. From inspection of the TEM images, the samples are spherical in shape and the iron oxide nanoparticles are incorporated near the centers of the particles. In general, there seem to be multiple iron oxide particles incorporated within each particle. As can be seen in the TEM images and as summarized in the size measurements in Table 6, the size of the core-shell nanoparticles ranged from 57-130 nm. The only sample that appears to have iron oxide that is not incorporated into the mesoporous silica shell material is M-MSN-3 as seen in Figure 28 which also had the smallest particles and the largest amount of added iron oxide nanoparticles. The size was controlled to some extent by the amount of iron oxide used in the reaction mixture such that increasing the iron oxide content of the reaction mixture lead to a smaller particle size for sample M-MSN-3.

Another aspect of this study that was investigated is the product yield, which is reported in mg product/ml reaction mixture in Table 6. The yields ranged from ~4-13 mg/ml with the core/shell sample prepared with Tris (M-MSN-T) resulting in the highest yield.

4.4. Discussion

In the synthesis process investigated here, the synthesis parameters were adjusted to maximize yield and minimize particle size. One of the first factors varied was the ratio of TEOS to TEA and TEA to surfactant (compare M-MSN-1 and M-MSN-2). The effect of this ratio on the particle size of these core-shell nanomaterials was hypothesized to be similar to the effect observed in WO type mesoporous silica nanoparticles which under similar reaction conditions demonstrated a decrease in particle size as the amount of TEA used in the reaction mixture decreased[135]. However, when the amount of TEA was varied, as shown in Table 6 when comparing M-MSN-1 and M-MSN-2, the particle size remained ~81-82 nm as measured by TEM suggesting that the size is invariant to the TEOS/TEA ratio in this range of synthesis conditions but the yield is nearly doubled as the amount of TEA in the solution decreases. Likely this is because, as has been previously suggested, TEA can slow and inhibit the growth of mesoporous silica[136]. When the amount of iron oxide nanoparticles in the reaction mixture was increased (compare M-MSN-3 to M-MSN-1 and M-MSN-2), the particle size decreased to ~57 nm. This decrease in size with increasing iron oxide content is consistent with what has been observed previously in the synthesis of mesoporous silica iron oxide core/shell nanomaterials[120]. However for this sample, M-MSN-3, excess agglomerated iron oxide without a mesoporous silica shell was observed in the TEM images leading to the conclusion that these parameters are not optimal for the preparation of homogeneous core/shell nanoparticles. This was further supported by preparing a sample identical to M-MSN-2 in every way except for the iron content which was increased to be the same as in M-MSN-3. This resulted in large aggregates of iron oxide nanoparticles in the sample (not shown).

Alteration of the TEOS/TEA ratio of the reaction mixture is seen to have an effect on both the pore volume and surface area of the nanomaterial. BJH measurements indicate that decreasing the amount of TEA relative to TEOS resulted in a slight increase in surface area (~4%) and a large increase in pore volume (nearly doubled) between M-MSN-1 and M-MSN-2

with the particle size remaining approximately the same. As will be discussed in more detail below, the yield increased from 4.3 to 7.8 mg/ml as the amount of TEA was decreased.

In addition to altering the relative ratios of the reactants, reactions utilizing alternative reactants were attempted. In M-MSN-B, CTAB was used as a surfactant and the reaction conditions were designed to promote high yield of sub-100 nm WO MSNs. These conditions are a modification of a previously published procedure for large scale mesoporous silica syntheses [132] in the absence of iron oxide cores. This modified procedure produced slightly larger than expected core-shell particles with an average size of 130 nm as seen in Table 6. The BJH pore volume and BET surface areas were significantly lower than other M-MSN synthesis methods suggesting that the use of CTAB is not optimal for producing sub-100 nm particles under these conditions. In the M-MSN-T synthesis, relatively inexpensive Tris buffer was used as the SOA yielding a high quality M-MSN product with similar properties to the MSN-1,2. While the pore volume was lower than the M-MSN-2 and M-MSN-3 batches but comparable to M-MSN-1, the pore diameter was only slightly smaller (3.2 nm compared to 3.3 nm) and the surface area was >800 m^2/g.

The product yields in this study range from 4.3 to 13.5 mg product /ml reaction mixture with the highest yield found for the sample prepared with the Tri buffer (M-MSN-T). This work has shown that high yields of WO type M-MSNs can be synthesized using uncoated iron oxide nanoparticles and utilizing a fast and relatively inexpensive procedure. While this procedure is not as efficient as the one reported by Zhang and coworkers (no core/shell)[132] which produced up to approximately 52 mg of mesoporous silica nanoparticles per ml of reaction mixture, the amount of core/shell nanoparticles generates on the order of 10 mg/ml reaction material for the most efficient conditions reported here. The synthesized iron oxide/mesoporous silica core/shell nanoparticles, particularly M-MSN-2 and M-MSN-T, have high surface areas and particle sizes of ~80 nm. This work has also demonstrated that relatively inexpensive Tris buffer can be used to produce high quality core-shell M-MSN particles.

Tris buffer is somewhat similar to TEA structurally and have similar pKa values of 8.07 and 7.74 respectively. The increased yield of product resulting from the use of Tris vs. TEA is suspected to be due to chelation effects. While both of these small organic amines are known chelating agents, TEA is a more efficient chelating agent than Tris and thus the rate of silica formation in the Tris based solution will be higher than when TEA is used. This increased rate of silica formation is thought to result in greater yields due the initial burst nucleation of stable silica nuclei.

4.5. Conclusions

Efficient, high yield, and greener synthesis of sub 100 nm iron oxide/mesoporous silica core/shell nanoparticles with wormlike (WO) pore morphology was demonstrated. The procedures presented here utilize relatively inexpensive materials and are scalable, which are important steps towards improving the viability of these materials. The product consists of a shell of wormhole like mesoporous silica with two or more iron oxide nanoparticles in the center of the particle which has an overall size of ~80 nm. The use of Tris buffer as an SOA yielded uniform ~87 nanoparticles with high surface area and pore volume and a high product yield. The results presented here are critically important in that a myriad of future applications for iron oxide/mesoporous silica core/shell nanocomposites are being investigated that will require large quantities of these materials.

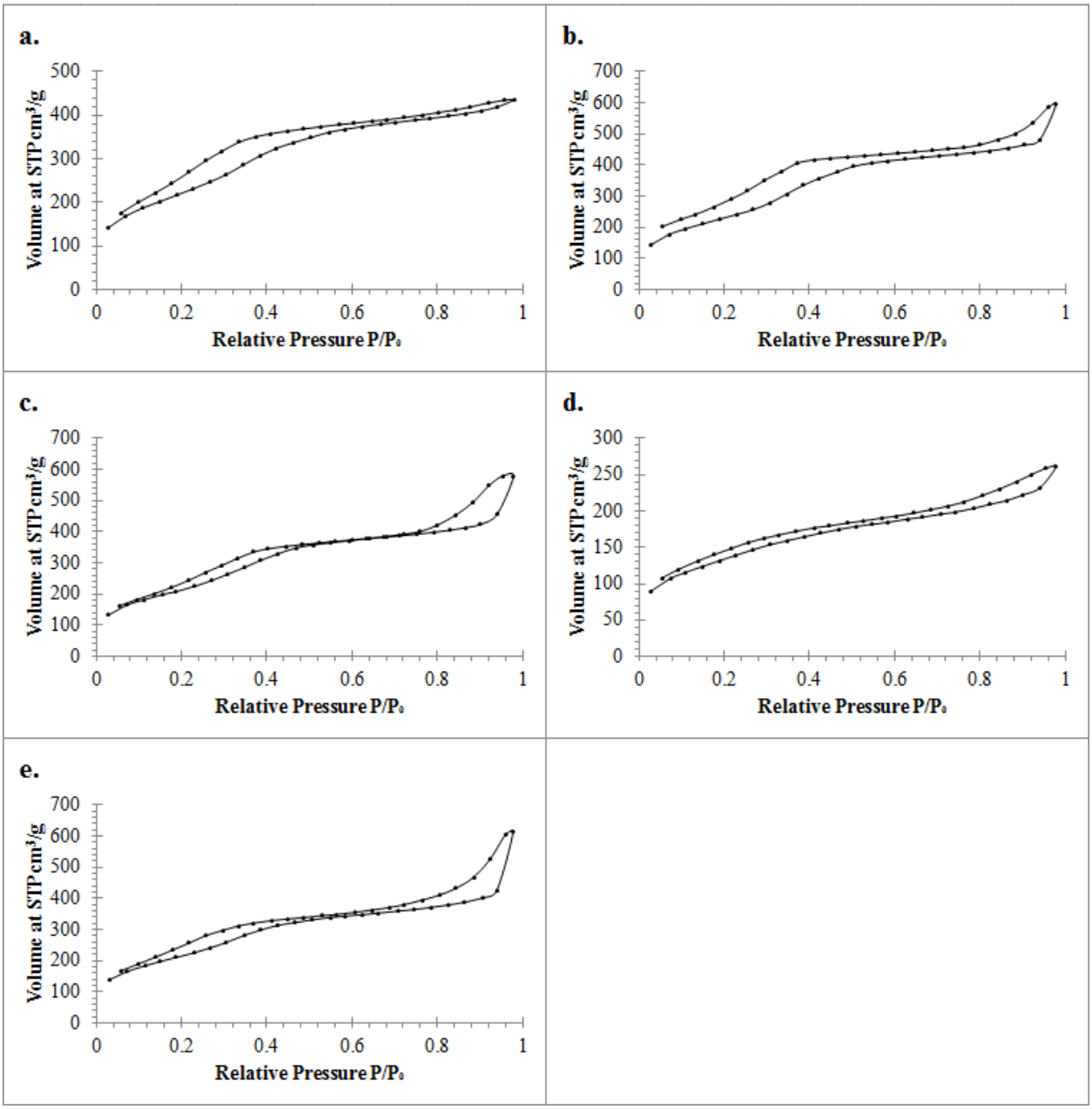

Figure 26 BET isotherms of a) M-MSN-1, b) M-MSN-2, c) M-MSN-3, d) M-MSN-B, and e) M-MSN-T.

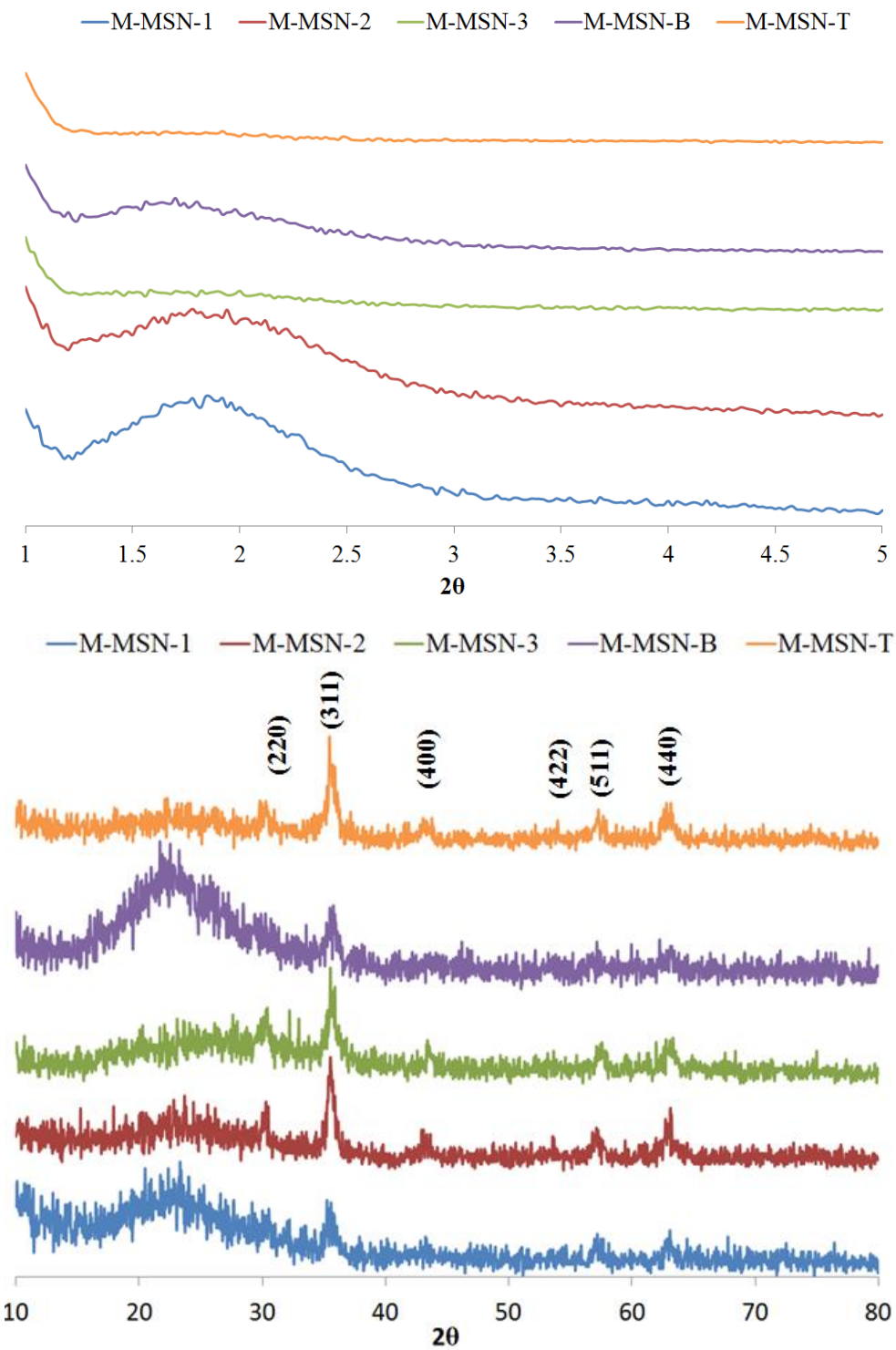

Figure 27 Low (top) and high (bottom) p-XRD patterns from each sample. Miller indices corresponding characteristic Fe_3O_4 planes to are shown above the high angle p-XRD.

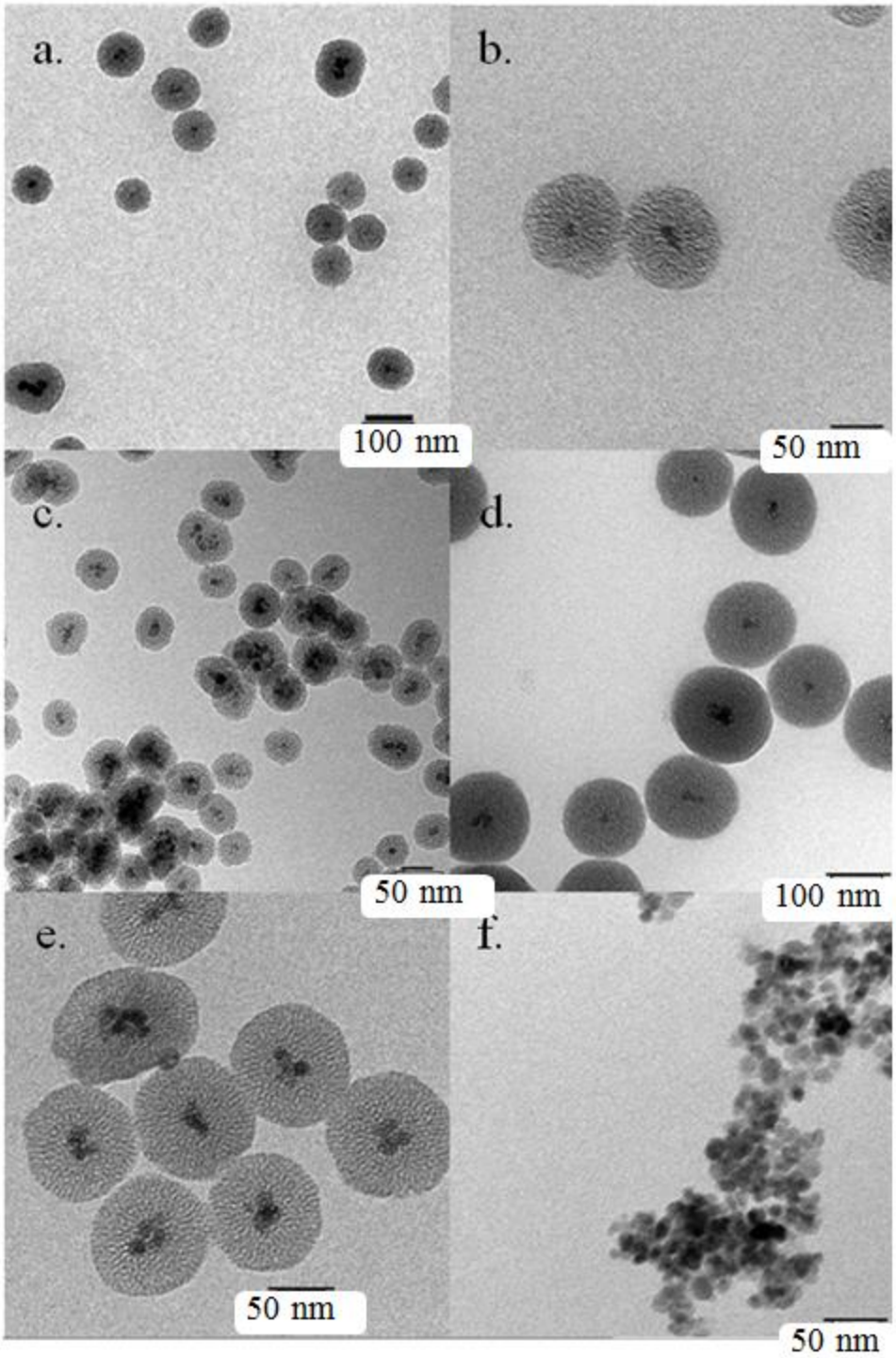

Figure 28 TEM images of a) M-MSN-1 (scale bar 100 nm), b) M-MSN-2 (scale bar 50 nm), c) M-MSN-3 (scale bar 50 nm), d) M-MSN-B (scale bar 100 nm), e) M-MSN-T (scale bar 50 nm), and f) uncoated Fe_3O_4 nanoparticles (scale bar 50 nm).

CHAPTER 5: ONE-POT SYNTHESIS OF IRON OXIDE CORE/SHELL MESOPOROUS SILICA NANOCOMPOSITES

5.1. Introduction

Mesoporous silica-metal oxide nanocomposites have many potential applications and are widely studied. One class of these nanocomposites; mesoporous silica coated Fe_3O_4 nanoparticles, have been identified as an important material in many fields including healthcare, optics, catalysis, and environmental remediation [38, 62, 67, 123, 137, 138]. Discrete nanoparticles with core-shell structures are of particular interest due to their high surface areas, improved suspendibility, faster mass transport, and large amount of accessible pore volume[62, 122].

In recent years, core/shell magnetic nanoparticles have been used in a variety of applications. These applications depend on their magnetic nature, small particle size, and porous structure. A small particle size is necessary for biological applications as larger particles are rejected by the body[129]. The magnetic nature of the nanoparticles allows this material to have potential use as MRI contrast agents[139]. The large amount of functionalizable internal surface area pore volume allows for the adsorption of significant quantities of drug [65, 130, 140]. Additionally, as nanoparticles have a higher ratio of external to internal surface area compared to bulk, a large amount of functionalizable external surface area is a feature of these materials. These materials have the potential to be utilized as multifunctional drug delivery/imaging platforms by combining the above applications[139].

Recently, synthetic research related to mesoporous silica-iron oxide nanocomposites has focused on the tuning of the material's properties. Specifically, several studies have sought to devise methodologies to control the thickness of the mesoporous silica coating [72, 141]. Other studies have focused on increasing pore volumes and pore sizes in order to obtain better drug loading capabilities[142, 143]. Other studies seek a deeper understanding of the formation mechanism of the core-shell nanocomposites in the hope of establishing greater overall synthetic control. Ultimately, another important facet of synthetic research involving these materials will

involve discovery and application of more streamlined synthetic procedures. In one literature example, Jin Zhang and coworkers combined the synthesis of iron oxide nanoparticles with the formation of mesoporous silica resulting in large nanocomposites[144].

For iron oxide core/shell mesoporous silica nanocomposites to become a more fully realized technology there are certain concerns that must be addressed. One of these concerns involves the simplification of the methods by which these materials are synthesized. Simplification is necessary to reduce the quantity of waste produced, minimize synthesis time, and improve product consistency. The balance between product quality and efficiency of production is crucial and necessitates study of this remarkable class of materials if they are to wide use.

In this work, a one pot method for the synthesis of iron oxide- mesoporous silica nanocomposite nanoparticles is described. Previously published synthetic methods for the formation of these materials used Fe_3O_4 nanoparticles that were either purchased or synthesized as an initial reagent in the one pot synthesis. Fe_3O_4 nanoparticles are relatively costly if purchased as a reagent and while the synthesis of Fe_3O_4 nanoparticles is relatively simple and can result in high yields, they are typically purified and surface treated prior to being coated with mesoporous silica. In this work, Fe_3O_4 nanoparticles are formed in transit to the final product with no intermediate purification or surface treatment. Using a one pot method to sequentially synthesize the Fe_3O_4 nanoparticles and coat the surface of said particles with mesoporous silica limits both time and expense.

5.2. Experimental Section

5.2.1. Materials

Cetyltrimethylammonium chloride (CTACl) solution (25% by mass), Cetyltrimethylammonium bromide, iron(III) chloride hexahydrate, iron (II) chloride tetrahydrate, triethanolamine (TEA) tetraethyl orthosilicate (TEOS) were purchased from Sigma Aldrich.

These purchased reagents were used as is without any purification. Water purified with a Millipore CDF01205 Milli-Q 4-Carterage water purification system was used in all reactions.

5.2.2. One-Pot Synthesis of Magnetic Mesoporous Silica Nanocomposites

Mesoporous silica coated iron oxide nanocomposite nanomaterials were synthesized in a one-pot reaction as illustrated in Figure 29. No purification or separation of the iron oxide nanoparticles was performed prior to mesoporous silica coating. In a typical synthesis, 200 ml of water was purged with nitrogen for 30 mins. Iron (III) chloride hexahydrate and iron (II) chloride tetrahydrate were then added to the solution under a nitrogen atmosphere. The iron sources were allowed to dissolve approximately 10 mins after which a 28% by mass aqueous ammonia solution was added. The caramel tinted solution immediately turned black and opaque as the Fe_3O_4 nanoparticles formed. This reaction was allowed to continue under a nitrogen atmosphere for two hours. An amount of surfactant (either CTACl or CTAB) was then added and the reaction mixture allowed to stir for 10 mins before the addition of a small organic amine (SOA). The resulting reaction mixture was then sonicated for two hours and subsequently heated to 80 °C and mechanically stirred at 1000 RPM. TEOS was then added and the reaction was allowed to stir for two hours. The product was the collected through a combination of large scale centrifuge followed by magnetic separation. The nanocomposite product is then washed twice with water and once with absolute ethanol. The product was then either calcined or template extracted. Calcined samples were heated to 550° C over a period 6 hours and then held at that temperature for 6 hours before being allowed to cool to room temperature. Template extracted samples were suspended in a solution of 200 ml of a solution consisting of 1.0 g of ammonium nitrate dissolved in ethanol. The solution was heated to 60 °C and magnetically stirred for 16 hours. This was repeated thrice before the product was washed twice with ethanol and dried at 80 °C overnight. In either case, the resulting nanocomposites were characterized by Inductively Coupled Plasma-Optical Emission Spectroscopy (ICP-OES), Powder X-Ray Diffraction (p-XRD), Transmission Electron Microscopy (TEM), and by applying the

(Brunauer–Emmett–Teller) and BJH (Barrett, Joyner, and Halenda) mathematical models physical adsorption measurements. The yields of these syntheses ranged from about 0.3-0.6 g.

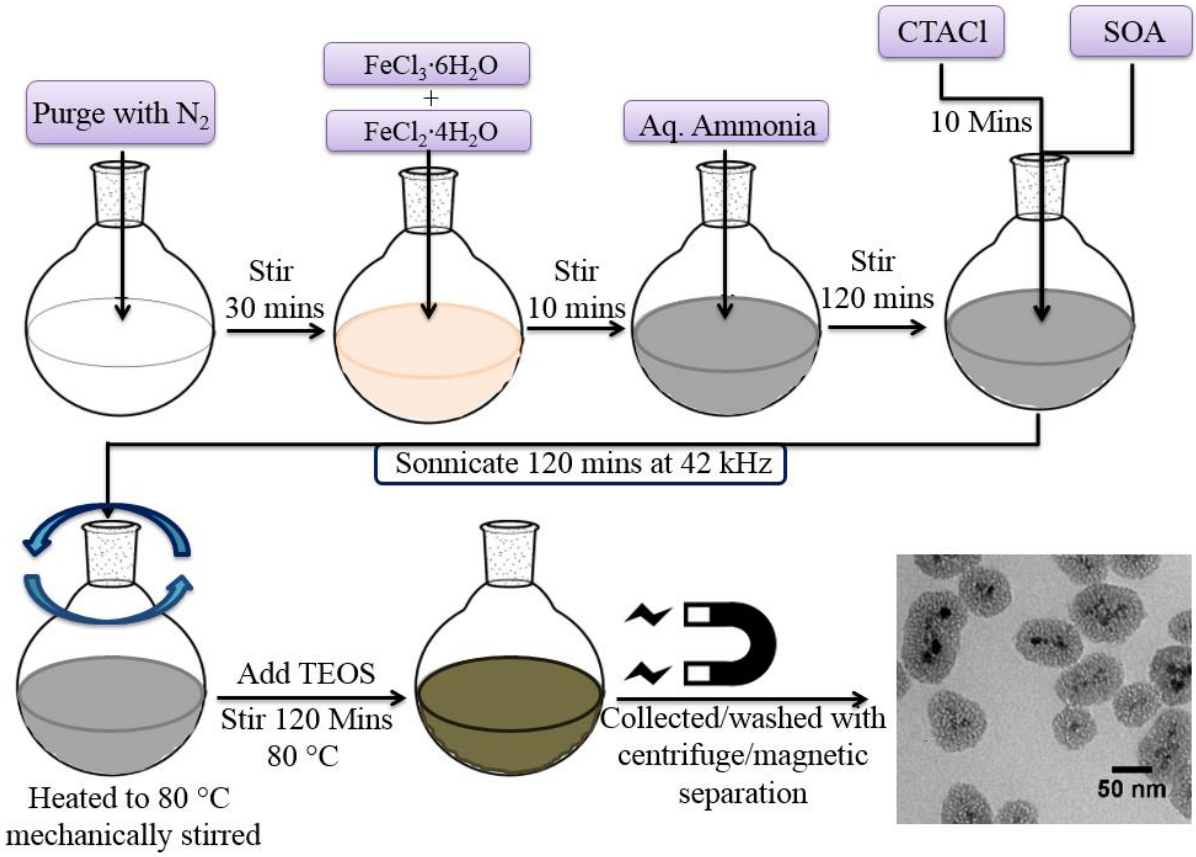

Figure 29 One pot synthetic procedure for the production of iron oxide core/shell mesoporous silica nanocomposite nanoparticles.

5.2.3. Characterization

Samples were outgassed for a period of 18 hours at 120 °C before being analyzed on a Quantachrome NOVA 1200 Surface Area Analyzer using nitrogen as the adsorption gas. Quantachrome NovaWin 2 software was used to apply BET and BJH mathematical models to the data to determine surface area and pore size/volume respectively. A portion of a given sample

was calcined and the other portion template extracted so that they could be directly compared with the surface area analyzer. Calcined samples analyzed by p-XRD with a Siemens D500 X-ray Diffractometer. Low angle and high angle powder patterns were collected over a range of 2θ = 1-5° and 10-80° respectively (0.04 step size with a step time of 1 second per step). Low angle p-XRD was used to compare the relative order/size of the nanocomposite nanoparticles and high angle was used to confirm iron oxide incorporation. A Varian 720-ES ICP-OES was used to determine the iron content of the nanocomposites. Massed samples were digested in an acid solution of concentrated HF/HCl/HNO_3 (20/60/20) under sonication. The digested samples were diluted with a 5% boric acid solution and water. A five point Fe standard curve was run and the digested samples were analyzed by ICP-OES (1.0 kW, argon flow 15 L/min). The % Fe by mass of the original nanocomposites was determined by comparing the digested sample mass to the iron concentrations of the digestions. The morphology and dimensions of the nanocomposites were determined using a JEOL 1230 TEM. The dry products were suspended in ethanol and sonicated before being deposited on a formvar-coated 300 mesh copper grid and allowed to dry at room temperature. Gatan Digital Micrograph and Image-J were used to measure the physical dimensions of the nanocomposites.

5.3. Results and Discussion

The overall goal of this work was to create a one pot method for the synthesis of discrete mesoporous silica coated core/shell iron oxide nanocomposite nanoparticles as shown in Figure 29. Specifically, synthesis of the Fe_3O_4 nanoparticles and coating of the nanoparticles was completed without the purification of any intermediates. This differs from the literature where iron oxide nanoparticles are typically synthesized and purified/surface modified prior to subsequent use in core/shell synthesis.

The two major events that occur in the reaction mixture are the formation of the Fe_3O_4 nanoparticles and the coating of said nanoparticles with mesoporous silica. The room temperature formation of iron oxide used in this synthesis typically employed a Fe^{3+}/Fe^{2+} ratio of

2:1 in order to favor the formation of Fe_3O_4 over Fe_2O_3 or other more highly oxidized forms of iron oxide. The nitrogen purge of the water with nitrogen aids in the removal of oxygen from the water that could lead to the oxidation of a Fe^{2+} to Fe^{3+}. However, because of the dilute nature of the synthesis in regards to Fe sources, an excess of Fe^{2+} was added under the assumption that there will be some degree of oxygenation occurring in the solution. The ratio employed was therefore 1.2:1 in order to be sure that the iron oxides nanoparticles formed were predominantly Fe_3O_4.

The experimental conditions were varied primarily after the formation of iron oxide nanoparticles and during the mesoporous silica coating process. Reaction conditions were systematically varied in order to obtain discrete core/shell structured nanoparticles.

The types and amounts of reagents used were varied systematically in pursuit of a core core/shell structure as listed in Table 7. Water/TEOS/Surfactant/Base systems are frequently used to produce mesoporous silica. Small organic amines (SOAs) are often employed as both bases and structural directing agents. The formation mechanism for the one pot mesoporous silica coated iron oxide nanoparticles produced by this method has several distinct phases. The first major event is the formation of Fe_3O_4 in a nitrogen protected aqueous environment. This step has a relatively well understood mechanism in which the Fe^{3+} and Fe^{2+} salt sourced cations present in solution form FeOOH and $Fe(OH)_2$ respectively upon the addition of a OH^- source(NH_4OH). These immediately react according to the formula $2FeOOH + Fe(OH)_2 + H_2O \rightarrow Fe_3O_4 + H_2O$ forming Fe_3O_4 nanoparticles with diameters of 11±2 nm. The exact formation mechanism of the mesoporous shell around the iron oxide nanoparticles is less clear; however, a potential mechanism can be theorized. The subsequently added cationic surfactant (CTA^+) reacts with the negatively charged surface of the nanoparticles as well as forming micelles. As a result, the iron oxide nanoparticles become surrounded by CTA^+ micelles. Heating of the system causes the micelles to assume rodlike shapes. Upon addition to the heated solution, the TEOS hydrolyzes and begins to form negatively charged tetrahedra, which associate with the CTA^+ micelles through electrostatic interactions. The hydrolyzed TEOS then condenses

to form a framework template by the micelles to form a mesoporous silica shell. The SOA is thought to act as both a base and a SDA. As a SDA, the SOA is thought to slow the formation of silica by chelating with the hydrolyzed TEOS thus slowing the condensation process. The SOAs used (Tris and TEA) are also believed to limit the growth and aggregate formation by acting as a encapsulation agents during the formation of the mesoporous shell[135].

The morphologies of the nanoparticles can be altered by varying the reaction conditions. Reaction conditions were varied in a rational and systematic manner in order to obtain discrete core/shell particles. As can be seen in Table 7, a range of conditions were tested in order to determine the optimal conditions for discrete sub 100 nm particle formation and small alteration of the reaction conditions produced notable differences in the final products. The physical characteristics selected products are summarized in Table 8.

Application of BET and BJH to the nitrogen isotherms verified the existence of the mesoporous silica shell. From Table 8, the iron oxide core/shell mesoporous silica nanocomposite products all exhibit high surface areas as determined by the BET method. The surface areas of these particles generally range between ~800 and 925 m^2/g with only the extremely aggregated and iron rich MMS-1P-1 demonstrating a sub 700 m^2/g surface area. With the same sample as an exception, pore size from BJH established a consistent 3.2 nm pore diameter for each sample indicating that the overall pore structure was unvarying between samples. From BJH, the less aggregated samples appear to have higher pore volume compared to the aggregated samples. This is not surprising as this increased pore volume demonstrates increased accessibility of the inner pore area as is typical of small porous particles. The difference between the aggregated/intergrown and dispersed nanocomposite nanoparticles is further established by the representative full nitrogen isotherms that appear in Figure 31. All surface areas, pore volumes, and pore diameters given in Table 8 are for calcined samples. Three template extractions were required for these values to be comparable for the template extracted portions of the samples.

From the p-XRD data in Figure 30, the Fe_3O_4 appears to be present in all of the products. The high angle p-XRD pattern of each of the spectra contain characteristic Miller indices indicative of Fe_3O_4 including values at approximately 30, 35.5, and 43 2θ which arise from the 220, 311, and 400 planes respectively. Low angle p-XRD patterns of the samples can provide information regarding the overall order of the pore structure of the particles. Generally a broad peak at 1.9 2θ is observed for WO type mesoporous silica materials. The broadness of the peak is due to the disordered nature of the WO mesoporous silica. This peak generally becomes more prominent as the particle size increases and smaller as it decreases due to the increase and decrease of long range order respectively. This effect can be magnified with core-shell particles lack of pore order contribution from the cores. In general the particles tested had very broad peaks at 1.9 in the low angle p-XRD. In the products with discrete particle formation, the peaks were very broad compared to the samples that resulted in larger aggregates. This is due to the lack of long range order due to the small particle size.

Elemental studies by ICP-OES demonstrate a wide range of % Fe loadings. In general, samples utilizing Tris as a surfactant tend to have the highest loading overall as seen in Table 8. Samples that utilized TEA as the SOA resulted in loadings of between 8 and 11%. The exceptions were MMS-1P-5, MMS-1P-11, and MMS-1P-12 which resulted in slightly elevated amounts of iron loading. This difference in samples MMS-1P-11 and MMS-1P-12 may be due to the higher pH conditions of these samples while MMS-1P-5 was due to the higher initial iron salt content of the reaction mixture.

TEM images were analyzed with Image-J and provide size and morphological information. Selected images appear in Figure 32 and the size distribution is shown in Table 8. Particle size and morphology are strongly dependent on the synthesis conditions and several size trends are observed. In general, large aggregates appeared at high concentrations of SOA. A similar trend was also observed in Bien et al. where higher concentrations of TEA resulted in larger particle sizes for mesoporous silica nanoparticles attributed to a decrease in the amount of rapidly hydrolysable TEOS available for the initial burst of nucleation resulting in fewer

seeds[135]. In this work, a similar process may be occurring in which a lack of hydrolysable TEOS results in less hydrolyzed silica associating with the iron oxide nanoparticle/surfactant sites at the point of initial TEOS addition. These silica poor iron oxide nanoparticle/surfactant/silica sites begin to associate through electrostatic interactions. As the SOA associated TEOS slowly hydrolyzes, the hydrolyzed silica is attracted to these aggregate sites and begins to cause particle intergrowth as they combine the proto mesoporous silica frameworks together. In conditions where sufficient quantities of hydrolysable TEOS are available in solution, sufficient hydrolyzed silica sources rapidly associate with iron oxide nanoparticle/surfactant sites and form proto-particles before particle intergrowth can occur. Figure 33 illustrates the mesoporous silica coating process proposed for this system. Interestingly, while still primarily consistent of individual nanoparticles, there was also a small increase in particle size of sample produced at TEOS/TEA ratios greater than 1:1. The sizes of these particles were comparable to those produced with no SOA.

One of the first parameters varied was the surfactant resulting in the observation that stoichiometrically equivalent amounts of CTAB and CTACl resulted in vastly different products. With all other ratios and reaction conditions remaining constant, the CTACl resulted in semi-discrete particles while CTAB resulted in large aggregates. The next parameter varied was the SOA used. The SOA in this reaction acts as an encapsulator and as a secondary base source. TEA and Tris were the two SOAs used in this study and have pKa values of 7.74 and 8.07 respectively and both resulted in iron oxide mesoporous silica nanocomposites. With all other conditions constant, an increase in TEOS results in the formation of large micrometer scale nanocomposites comprised of fused nanocomposite particles. This is likely due to particles aggregating and fusing in solution with the excess silica resulting in intergrowth. Interestingly, when no SOAs were utilized in the reaction leaving ammonia as the only source of base, discrete particles <100 nm were obtained. This further supports the theory that high concentrations of SOA are the primary cause of aggregate formation in this system. In order to determine the optimal concentration of TEA, once again holding all other reaction parameters constant, the

amount of TEA was varied with TEOS/TEA ratios of 0.27-4.76 (samples:MMS-1P-3, MMS-1P-7, MMS-1P-9, and MMS-1P-10). The smallest particle size and greatest particle uniformity were produced at a TEOS/TEA ratio of ~1:1. As previously discussed, similar trends have been previously observed in the formation of nanometer scale mesoporous silica where, as the ratio of TEOS/TEA is decreased through the addition of increasing amounts of TEA, aggregates begin to form. This trend also demonstrates that as the amount of TEA in the solution decreases below a TEOS/TEA value of 1:1, a slight increase (~25 nm) in particles size. The later trend was unexpected because as compared to a TEA free synthesis such as MMS-1-10, the reactions with TEOS/TEA ratios between 4.3 and 1 resulted in particle sizes of larger and less uniform than those of the TEA free synthesis. This data suggests that for this system, a 1:1 TEOS/TEA ratio results in discrete particles with the smallest diameter.

Another series of experiments in this series studied the effects of TEOS concentration (MMS-1P-4, and MMS-1P-6). MMS-1P-6 and MMS-1P-4 are directly comparable to MMS-1P-3 with the only difference being the amount of TEOS added. MMS-1P-3 used the standard amount of TEOS while MMS-1P-6 and MMS-1P-4 used 25% and 50% more TEOS respectively. All of these cases resulted in the formation of large aggregates; however, MMS-1P-6 resulted in a mixture of aggregates and discrete particles. This was most likely the result of sufficient TEOS concentration in MMS-1P-6 for the formation of discrete particles early in the reaction condition but the larger amount of TEOS caused subsequent intergrowth. A series of experiments were performed to probe the effect of the base type and quantity on the formation of the nanocomposite material both in terms of iron loading and particle formation. This set of experiments (MMS-1P-10, MMS-1P-11, MMS-1P-12) were performed without a SOA such that the only source of base during the addition of the Fe_3O_4 nanoparticle nanoparticles. As compared to the control (MMS-1P-10) the particle size and iron loading both MMS-1P-11 and MMS-1P-12 increased. This increase in iron loading is of particular interest as high iron loading is desirable for catalysis and drug delivery. A series of reactions with identical compositions to MMS-1P-10 demonstrated the expected trend that when sonication time is reduced (1 hour and

½ hour), aggregation and intergrowth increases (not shown). Also not shown, when CTAB is substituted for CTACl in conditions identical to MMS-1P-7, aggregates once again form indicating that CTACl is a better template for discrete particles under these conditions.

5.4. Conclusions

Iron oxide core/shell mesoporous silica nanocomposite nanoparticles were successfully synthesized through a one pot method. Iron oxide nanoparticles were synthesized en route to the final product. A variety of conditions were altered to study their effects of the final products including SOA type, SOA concentration, sonication time, base source, and silica concentration. By varying these conditions, it is possible to gain control of particle size, iron loading, and aggregation. This work represents a green, fast, and simple on demand method for the synthesis of iron oxide mesoporous silica core/shell nanocomposites. Further studies are currently underway to further control the properties of these materials and to increase the overall yields.

Table 7 One pot Synthesis Conditions[a]

Sample Name	TEOS/ SOA	SOA	TEOS/ Fe	TEOS/ Base	TEOS/ Surfactant	Surfactant
MMS-1P-1	0.27	Tris	9.8	2.8(NH_4^+)	1.48	CTAB
MMS-1P-2	0.27	Tris	9.8	2.8(NH_4^+)	1.48	CTAC
MMS-1P-3	0.27	TEA	9.8	2.8(NH_4^+)	1.48	CTAC
MMS-1P-4	0.34	TEA	12.2	3.5(NH_4^+)	1.85	CTAC
MMS-1P-5	0.41	TEA	9.7	4.2(NH_4^+)	2.22	CTAC
MMS-1P-6	0.41	TEA	14.7	4.2(NH_4^+)	2.22	CTAC
MMS-1P-7	0.99	TEA	9.8	2.8(NH_4^+)	1.48	CTAC
MMS-1P-8	2.38	TEA	9.8	2.8(NH_4^+)	1.48	CTAC
MMS-1P-9	4.76	TEA	9.8	2.8(NH_4^+)	1.48	CTAC
MMS-1P-10	N/A	None	9.8	2.8(NH_4^+)	1.48	CTAC
MMS-1P-11	N/A	None	9.8	0.5 (NH_4^+)	1.48	CTAC
MMS-1P-12	N/A	None	9.8	2.8(NaOH)	1.48	CTAC

[a]All ratios are scaled in terms of TEOS content for comparison.

Table 8 Physical Characterization Data

Sample Name	**Surface Area[a] (m^2/g)**	**Pore Diameter[b] (nm)**	**BJH Pore Volume[b] (cm^3/g)**	**%Fe by Mass[c]**	**Particle Size[d] (nm)**
MMS-1P-1	648(5)	3.1(0.0)	0.218(0.002)	31.2(2.1)	µm scale aggregates
MMS-1P-2	919(6)	3.2(0.1)	0.425(0.003)	22.7(0.1)	63(16)*
MMS-1P-3	924(6)	3.2(0.1)	0.170(0.001)	10.7(0.1)	µm scale aggregates
MMS-1P-4	921(6)	3.2(0.1)	0.132(0.001)	9.8(0.6)	µm scale aggregates
MMS-1P-5	907(6)	3.2(0.1)	0.184(0.001)	18.1(0.4)	µm scale aggregates
MMS-1P-6	885(6)	3.2(0.1)	0.244(0.002)	8.8(0.9)	98(14) + larger aggregates
MMS-1P-7	883(6)	3.2(0.1)	0.555(0.004)	10.0 (3.5)	62(13)
MMS-1P-8	882(6)	3.2(0.1)	0.530(0.004)	8.0 (0.0)	88(21)
MMS-1P-9	923(6)	3.2(0.1)	0.452(0.003)	10.2(1.0)	89(35)
MMS-1P-10	808(6)	3.2(0.1)	0.338(0.002)	9.6(0.5)	68(16)
MMS-1P-11	855(6)	3.2(0.1)	0.418(0.003)	19.3(3.9)	84(24)
MMS-1P-12	898(6)	3.2(0.1)	0.486(0.003)	14.0(1.8)	83(14)

a. Measured by nitrogen adsorption and the BET method

b. Measured by BJH method (Pore diameter reported above range of error bars)

c. Measured by ICP-OES

d. Determined from TEM; standard deviation given in parenthesis

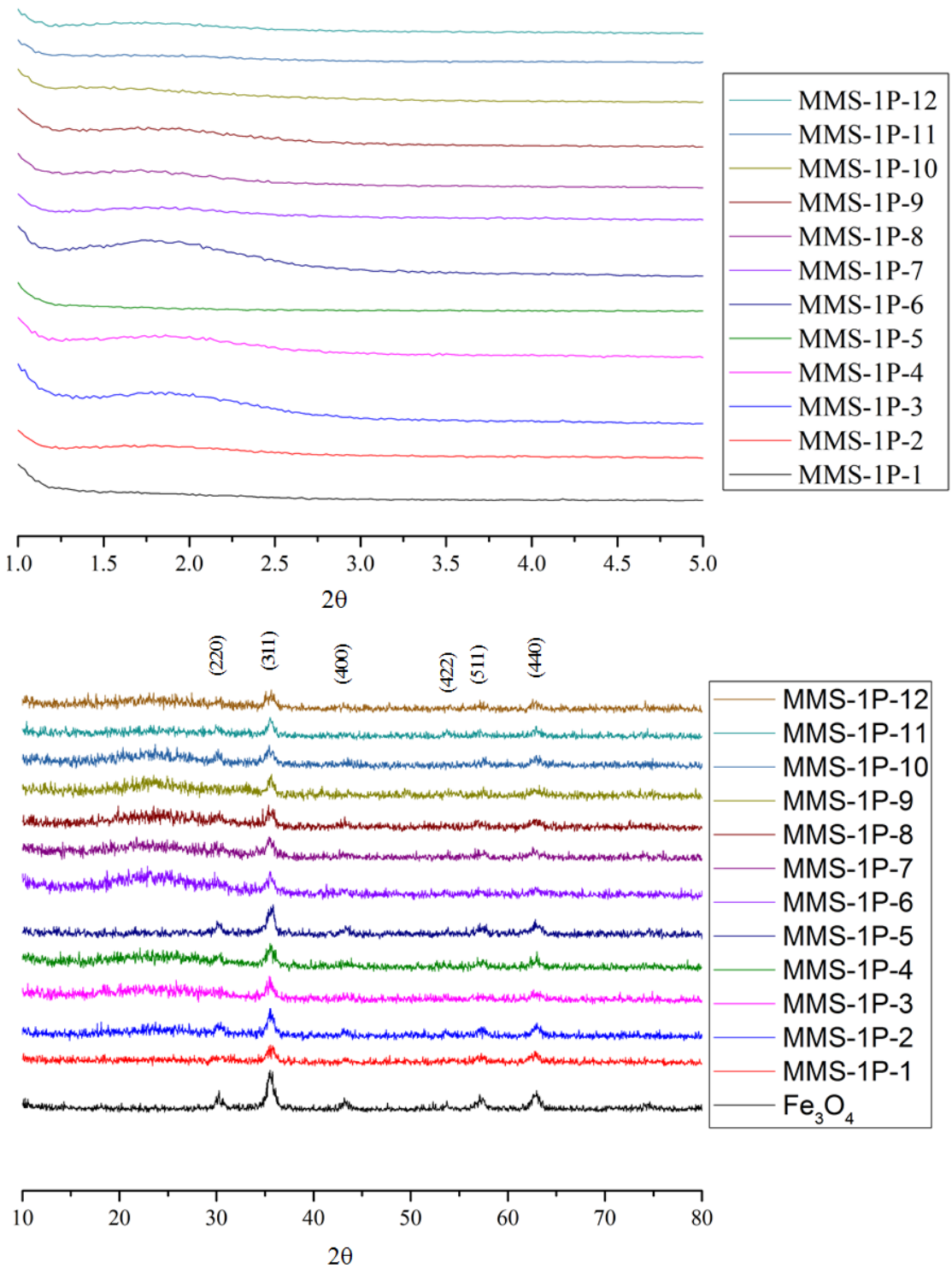

Figure 30 Low (top) and high angle (bottom) p-XRD patterns of products. Samples arranged sequentially with 1PMMS-1 at the bottom.

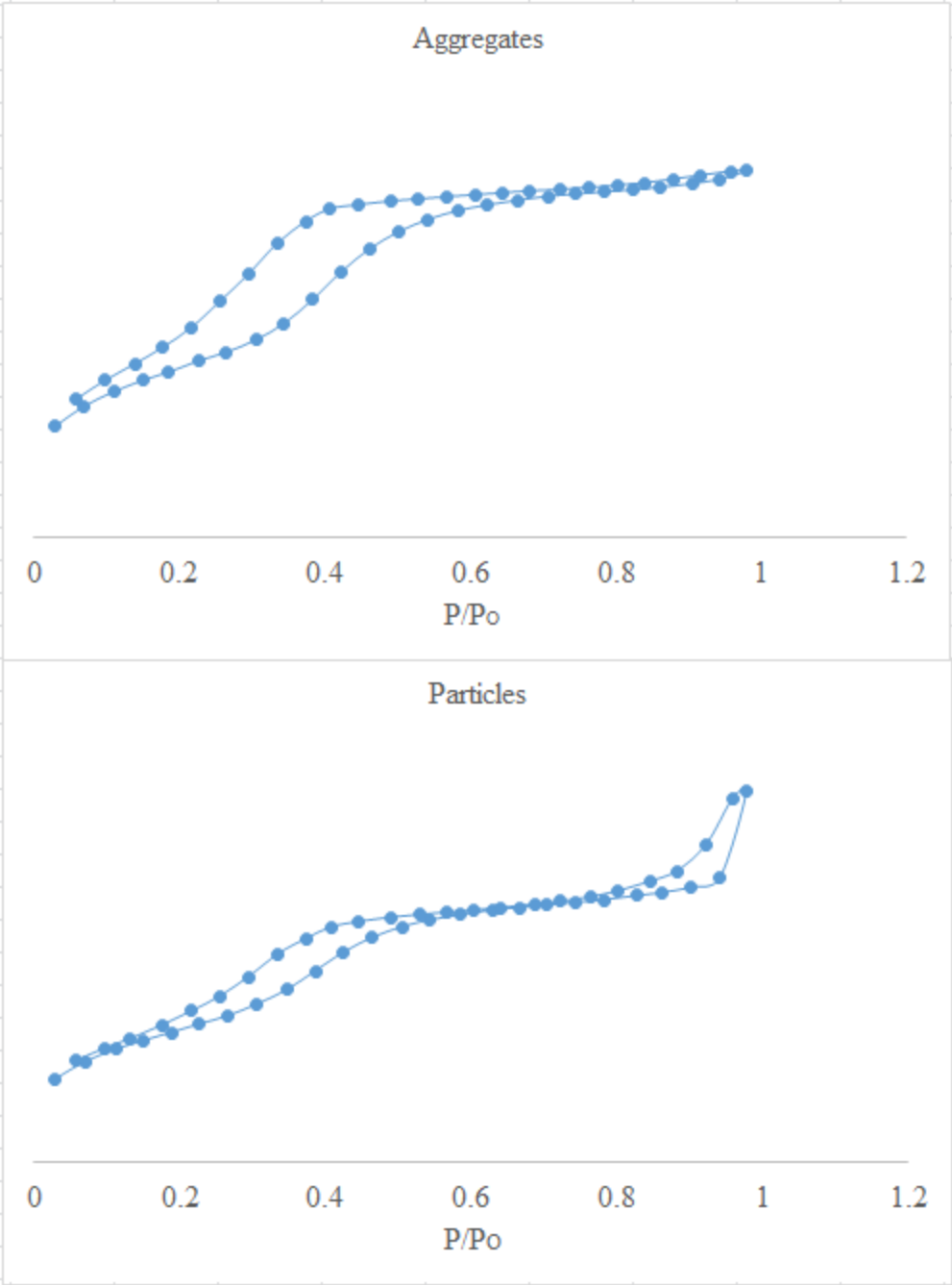

Figure 31 Representative adsorption/desorption isotherms products consisting mainly of large aggregated/intergrown particles (top MMS-1P-3) and individual nanoparticles (bottom MMS-1P-12).

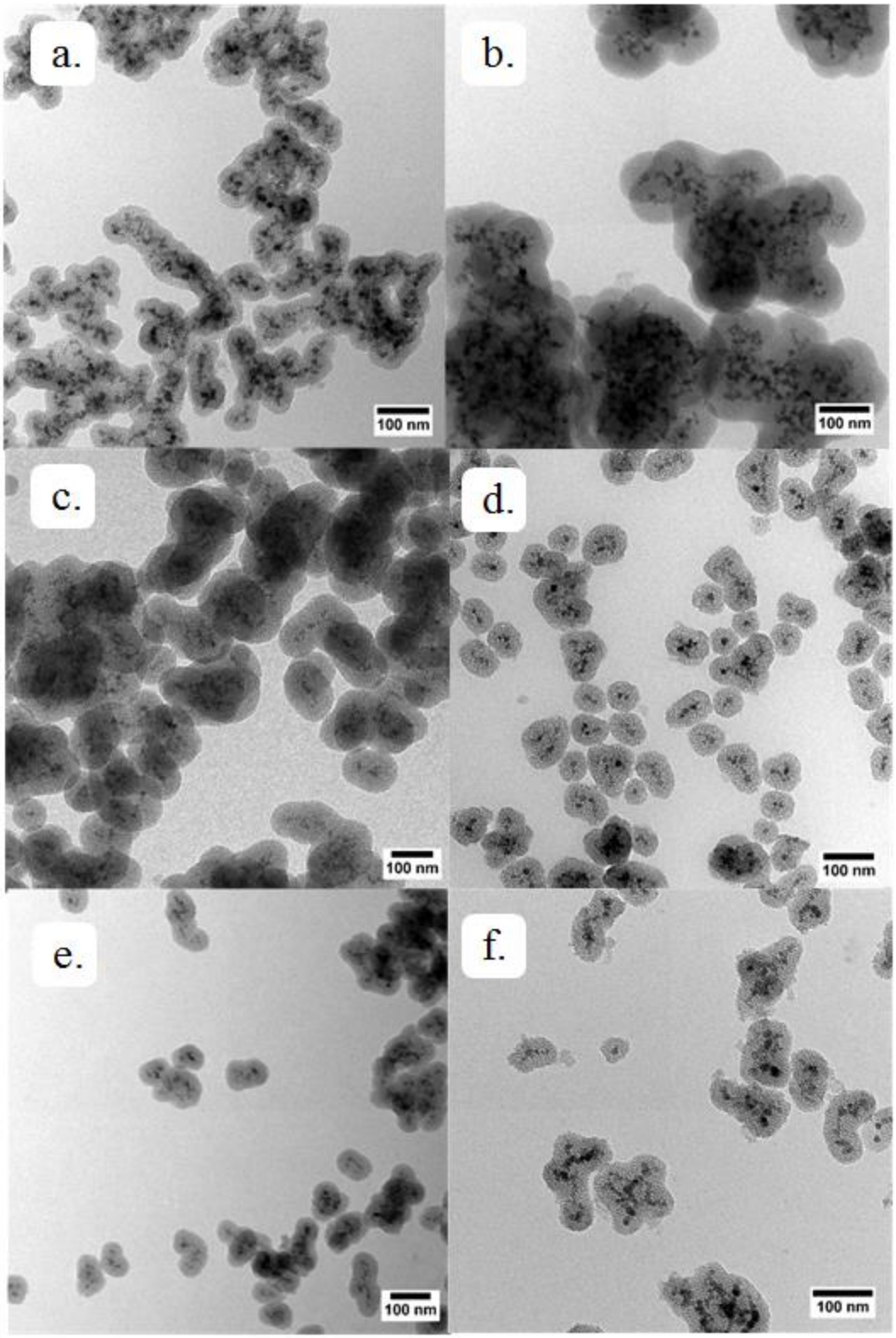

Figure 32 TEM images of selected synthetic products post calcination. In alphabetical order MMS1P--2 (a), MMS-1P-5 (b), MMS-1--6 (c), MMS-1P-7 (d), MMS-1P-8 (e), and MMS-1P-11(f).

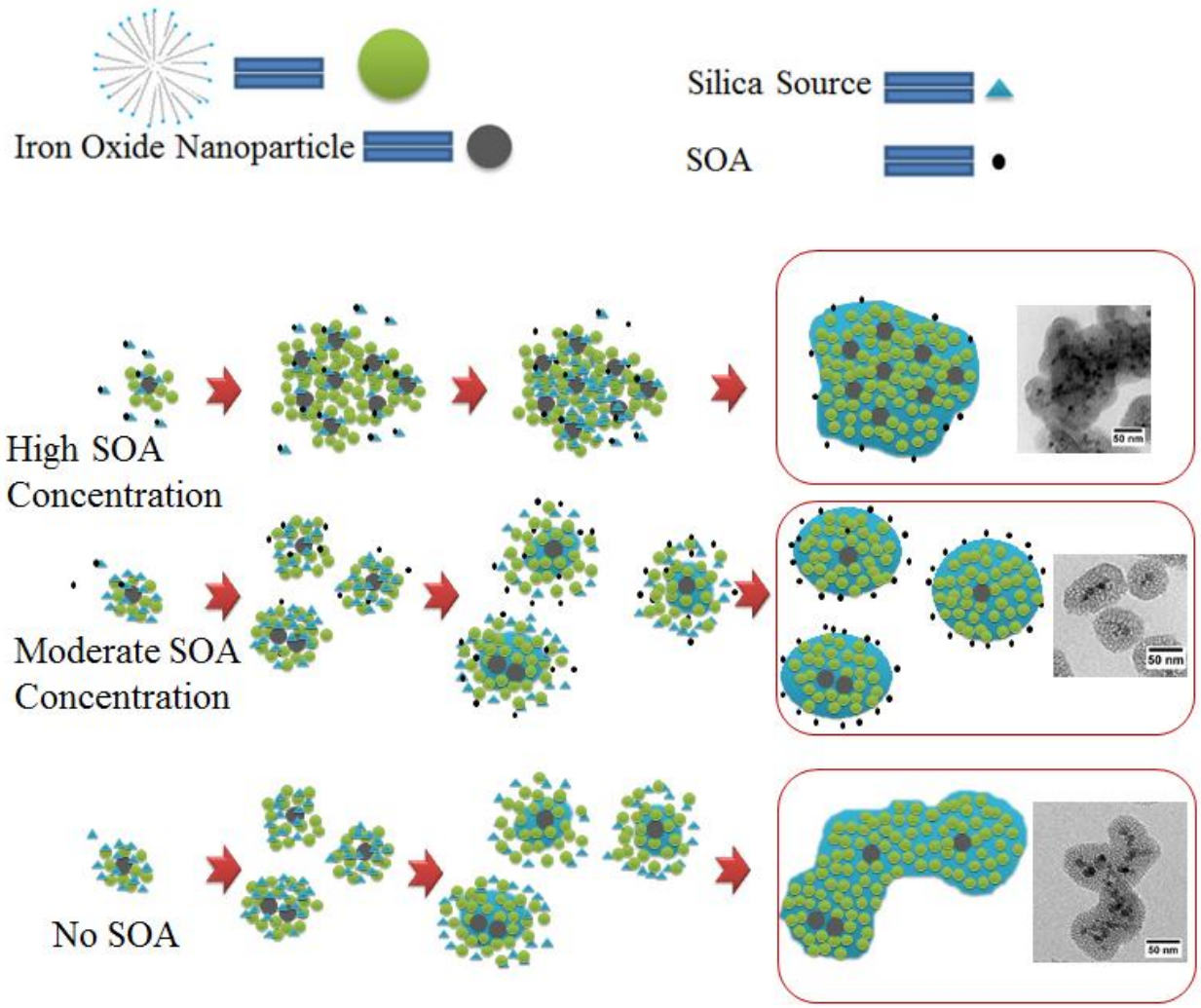

Figure 33 Hypothesized synthesis of iron oxide mesoporous silica core/shell nanocomposites

CHAPTER 6: CONCLUSIONS AND FUTURE WORK

The work highlighted in this thesis has focused primarily on the synthesis and characterization of porous silica based materials. Green chemistry is chemical methodology defined as the pursuit of processes designed to minimize hazardous waste production. By this definition, advances in green chemistry can include increases in efficiency as well as through the elimination of waste producing steps. The primary objectives of this work are motivated by a need for green, economical, and scalable synthesis of nanomaterials for use in applications. This general methodology is present throughout the thesis. The work in Chapter 2 resulted in the production of large quantities of nonporous and mesoporous silica nanoparticles needed for nanomaterial toxicology studies that are in progress. The work in Chapter 3 focused the synthesis of high yields of FAU type zeolite that utilized recycling of the reaction mixture in order to increase yield and decreased the waste produced during synthesis. The work in Chapter 4 explored high yield synthetic methods for the production of iron oxide core/shell mesoporous silica nanocomposite nanomaterials. Finally, a greener method for the production of iron oxide core/shell mesoporous silica nanoparticles was presented in Chapter 5. This was accomplished by combining the synthesis of iron oxide nanoparticles with the coating of these particles in a single one pot reaction mixture. The resulting synthesis is fast, simple, and efficient both in terms of time and waste production. The synthetic procedures are able to produce a range of iron oxide core/shell mesoporous silica nanoparticles with different sizes, iron loadings, and morphologies. The materials produced in this work are currently being evaluated for environmental remediation, drug delivery, and battery material applications.

For both of the iron oxide/core/shell mesoporous silica nanomaterial synthesis methodologies explored in this work, CTACl is seen to favor discrete particles as compared to CTAB which is seen frequently result in large aggregates of undergrown particles.

In order for nanomaterials to become a viable component of nanotechnologies, they must have the ability to be produced in a cost effective scalable manner. Many potentially exciting

new materials are not practical for applications because they are currently either cost prohibitive to manufacture in terms of materials or time required. Even currently used materials benefit from a reduction in cost and environmental impact and an increase in synthetic efficiency. Some of the most exciting challenges in the field of materials chemistry moving forward will involve not just discovery of novel materials, but moving towards synthesizing these materials safely, efficiently, and in an environmentally conscious manner.

Moving forward, the synthesis of synthetic zeolites will need to be scaled up. Recycling techniques like the one outlined in this thesis will be of greater importance as the current synthetic methods generate a considerable quantity of waste. In order for these recycling procedures to reach their maximum potential, studies of the reaction mixture after each recycling to determine the identities and quantities of the species present in solution will need to be performed. This could lead to processes by which additional quantities of the limiting species could be added to the solution in order to increase yield and maximize the effectiveness of each recycling. This will likely involve elemental analysis, mass spectroscopy, and NMR studies.

The future of iron oxide core/shell mesoporous silica nanomaterials will depend on improving the yields and minimizing waste as well as seeking out less expensive silica sources. Moving from to a one pot synthetic method as described in this thesis is an important step in increasing the viability of this material. The next step will involve increasing efficiency of the reaction. This will involve systematically increasing the quantities of certain reactants such as TEOS, $FeCl_3$, and $FeCl_2$ and applying the methodologies seen in chapter 4. Specifically, conditions will be altered to increase the amount of iron oxide nanoparticles synthesized in the first step.

REFERENCES

1. Wingenfelder, U., et al., *Removal of Heavy Metals from Mine Waters by Natural Zeolites.* Environmental Science & Technology, 2005. **39**(12): p. 4606-4613.

2. Kanthasamy, R. and S.C. Larsen, *Visible light photoreduction of Cr(VI) in aqueous solution using iron-containing zeolite tubes.* Microporous Mesoporous Mater., 2007. **100**(1-3): p. 340-349.

3. Mumpton, F.A., *La roca magica: Uses of natural zeolites in agriculture and industry.* Proceedings of the National Academy of Sciences, 1999. **96**(7): p. 3463-3470.

4. Virta, R., *Natural and Synthetic Zeolites*, in *Geotimes Mineral Resource of the Month*. 2008: Geotimes.

5. Fu, F. and Q. Wang, *Removal of heavy metal ions from wastewaters: A review.* Journal of Environmental Management, 2011. **92**(3): p. 407-418.

6. Maxwell, I.E., *Zeolite catalysis in hydroprocessing technology.* Catalysis Today, 1987. **1**(4): p. 385-413.

7. Datt, A., D. Fields, and S.C. Larsen, *An Experimental and Computational Study of the Loading and Release of Aspirin from Zeolite HY.* The Journal of Physical Chemistry C, 2012. **116**(40): p. 21382-21390.

8. Ndiege, N., et al., *Preparation of a Versatile Bifunctional Zeolite for Targeted Imaging Applications.* Langmuir, 2011. **27**(6): p. 2904-2909.

9. Storch, G., et al., *Hydrothermal stability of pelletized zeolite 13X for energy storage applications.* Adsorption, 2008. **14**(2-3): p. 275-281.

10. Mueller, P.S. and S.C. Larsen, *Incorporation of germanium into the framework of nanocrystalline faujasite.* Microporous and Mesoporous Materials, 2013. **180**(0): p. 229-234.

11. Tang, B., et al., *A procedure for the preparation of Ti-Beta zeolites for catalytic epoxidation with hydrogen peroxide.* Green Chemistry, 2014. **16**(4): p. 2281-2291.

12. Meng, X., F. Nawaz, and F.-S. Xiao, *Templating route for synthesizing mesoporous zeolites with improved catalytic properties.* Nano Today, 2009. **4**(4): p. 292-301.

13. Paillaud, J.-L., et al., *Extra-Large-Pore Zeolites with Two-Dimensional Channels Formed by 14 and 12 Rings.* Science, 2004. **304**(5673): p. 990-992.

14. Smith, L., et al., *On the Nature of Water Bound to a Solid Acid Catalyst.* Science, 1996. **271**(5250): p. 799-802.

15. Guisnet, M., et al., *Isomerization of n-hexane on platinum dealuminated mordenite catalysts I. Influence of the silicon-to-aluminium ratio of the zeolite.* Applied Catalysis, 1991. **71**(2): p. 283-293.

16. Petushkov, A., J. Freeman, and S.C. Larsen, *Framework Stability of Nanocrystalline NaY in Aqueous Solution at Varying pH.* Langmuir, 2010. **26**(9): p. 6695-6701.

17. Wu, H., et al., *Surface-modified Y zeolite-filled chitosan membrane for direct methanol fuel cell.* Journal of Power Sources, 2007. **173**(2): p. 842-852.

18. Nur, H., et al., *Organosulfonic acid functionalized zeolite ZSM-5 as temperature tolerant proton conducting material.* International Journal of Hydrogen Energy, 2012. **37**(17): p. 12513-12521.

19. Zhan, B.-Z., M.A. White, and M. Lumsden, *Bonding of Organic Amino, Vinyl, and Acryl Groups to Nanometer-Sized NaX Zeolite Crystal Surfaces.* Langmuir, 2003. **19**(10): p. 4205-4210.

20. Li, Z., C. Lai, and T.E. Mallouk, *Self-assembling trimolecular redox chains at zeolite Y modified electrodes.* Inorganic Chemistry, 1989. **28**(2): p. 178-182.

21. Huber, S. and G. Calzaferri, *Sequential Functionalization of the Channel Entrances of Zeolite L Crystals.* Angewandte Chemie International Edition, 2004. **43**(48): p. 6738-6742.

22. Mintova, S., J.-P. Gilson, and V. Valtchev, *Advances in nanosized zeolites.* Nanoscale, 2013. **5**(15): p. 6693-6703.

23. Song, W., et al., *Size-dependent properties of nanocrystalline silicalite synthesized with systematically varied crystal sizes.* Langmuir, 2004. **20**(11): p. 4696-702.

24. Teruoki Tango, H.K., Yuta Nakasaka, Takao Masuda, *Size-Controlled Synthesis of Nano-Zeolites and Their Application to Light Olefin Synthesis.* Catal Surv Asia, 2012. **16**.

25. Larsen, S.C., *Nanocrystalline Zeolites and Zeolite Structures: Synthesis, Characterization, and Applications.* The Journal of Physical Chemistry C, 2007. **111**(50): p. 18464-18474.

26. Valtchev, V. and L. Tosheva, *Porous Nanosized Particles: Preparation, Properties, and Applications.* Chemical Reviews, 2013. **113**(8): p. 6734-6760.

27. Cundy, C.S. and P.A. Cox, *The hydrothermal synthesis of zeolites: history and development from the earliest days to the present time.* Chemical Reviews, 2003. **103**(3): p. 663-702.

28. Chang, C. and A. Bell, *Studies on the mechanism of ZSM-5 formation.* Catalysis Letters, 1991. **8**(5-6): p. 305-316.

29. Ruiz, A.Z., et al., *Synthesis of Zeolite L. Tuning Size and Morphology.* Monatshefte für Chemie / Chemical Monthly, 2005. **136**(1): p. 77-89.

30. Wang, H., B.A. Holmberg, and Y. Yan, *Synthesis of Template-Free Zeolite Nanocrystals by Using in Situ Thermoreversible Polymer Hydrogels.* Journal of the American Chemical Society, 2003. **125**(33): p. 9928-9929.

31. Zhang, L., et al., *Organic template-free synthesis of ZSM-5/ZSM-11 co-crystalline zeolite.* Microporous and Mesoporous Materials, 2012. **147**(1): p. 117-126.

32. Robson, H., *Verified Syntheses of Zeolitic Materials Second Revised Edition*. 2001: Elsevier.

33. Vallet-Reg, et al., *Mesoporous Silica Nanoparticles: Their Projection in Nanomedicine.* ISRN Materials Science, 2012. **2012**: p. 20.

34. He, Q. and J. Shi, *Mesoporous silica nanoparticle based nano drug delivery systems: synthesis, controlled drug release and delivery, pharmacokinetics and biocompatibility.* Journal of Materials Chemistry, 2011. **21**(16): p. 5845-5855.

35. Slowing, I.I., et al., *Mesoporous Silica Nanoparticles for Drug Delivery and Biosensing Applications.* Advanced Functional Materials, 2007. **17**(8): p. 1225-1236.

36. Slowing, I.I., et al., *Mesoporous silica nanoparticles as controlled release drug delivery and gene transfection carriers.* Advanced Drug Delivery Reviews, 2008. **60**(11): p. 1278-1288.

37. Datt, A., I. El-Maazawi, and S.C. Larsen, *Aspirin Loading and Release from MCM-41 Functionalized with Aminopropyl Groups via Co-condensation or Postsynthesis Modification Methods.* The Journal of Physical Chemistry C, 2012. **116**(34): p. 18358-18366.

38. Taylor, K.M.L., et al., *Mesoporous Silica Nanospheres as Highly Efficient MRI Contrast Agents.* Journal of the American Chemical Society, 2008. **130**(7): p. 2154-2155.

39. Kim, T., et al., *Mesoporous Silica-Coated Hollow Manganese Oxide Nanoparticles as Positive T1 Contrast Agents for Labeling and MRI Tracking of Adipose-Derived Mesenchymal Stem Cells.* Journal of the American Chemical Society, 2011. **133**(9): p. 2955-2961.

40. M Rosenholm, J., C. Sahlgren, and M. Linden, *Multifunctional mesoporous silica nanoparticles for combined therapeutic, diagnostic and targeted action in cancer treatment.* Current drug targets, 2011. **12**(8): p. 1166-1186.

41. Chen, C.-Y., H.-X. Li, and M.E. Davis, *Studies on mesoporous materials: I. Synthesis and characterization of MCM-41.* Microporous Materials, 1993. **2**(1): p. 17-26.

42. Mokaya, R., *Improving the Stability of Mesoporous MCM-41 Silica via Thicker More Highly Condensed Pore Walls.* The Journal of Physical Chemistry B, 1999. **103**(46): p. 10204-10208.

43. Elma, M., et al., *Performance and Long Term Stability of Mesoporous Silica Membranes for Desalination.* Membranes, 2013. **3**(3): p. 136-150.

44. Wu, S.-H., C.-Y. Mou, and H.-P. Lin, *Synthesis of mesoporous silica nanoparticles.* Chemical Society Reviews, 2013. **42**(9): p. 3862-3875.

45. El Mourabit, S., et al., *Stability of mesoporous silica under acidic conditions.* RSC Advances, 2012. **2**(29): p. 10916-10924.

46. Sayari, A., S. Hamoudi, and Y. Yang, *Applications of Pore-Expanded Mesoporous Silica. 1. Removal of Heavy Metal Cations and Organic Pollutants from Wastewater.* Chemistry of Materials, 2004. **17**(1): p. 212-216.

47. Kao, K.-C. and C.-Y. Mou, *Pore-expanded mesoporous silica nanoparticles with alkanes/ethanol as pore expanding agent.* Microporous and Mesoporous Materials, 2013. **169**(0): p. 7-15.

48. Yang, H., et al., *Hybrid surfactant-templated mesoporous silica formed in ethanol and its application for heavy metal removal.* Journal of Hazardous Materials, 2008. **152**(2): p. 690-698.

49. Bomati-Miguel, O., et al., *Ex vivo assessment of polyol coated-iron oxide nanoparticles for MRI diagnosis applications: toxicological and MRI contrast enhancement effects.* Journal of Nanoparticle Research, 2014. **16**(3): p. 1-13.

50. Gupta, A.K. and M. Gupta, *Synthesis and surface engineering of iron oxide nanoparticles for biomedical applications.* Biomaterials, 2005. **26**(18): p. 3995-4021.

51. Fei, H., et al., *Preparation of carbon-coated iron oxide nanoparticles dispersed on graphene sheets and applications as advanced anode materials for lithium-ion batteries.* Nano Research, 2014. **7**(4): p. 1-9.

52. Rahim Pouran, S., A.A. Abdul Raman, and W.M.A. Wan Daud, *Review on the application of modified iron oxides as heterogeneous catalysts in Fenton reactions.* Journal of Cleaner Production, 2014. **64**(0): p. 24-35.

53. Weinstein, J.S., et al., *Superparamagnetic iron oxide nanoparticles: diagnostic magnetic resonance imaging and potential therapeutic applications in neurooncology and central nervous system inflammatory pathologies, a review.* Journal of Cerebral Blood Flow & Metabolism, 2010. **30**(1): p. 15-35.

54. Teja, A.S. and P.-Y. Koh, *Synthesis, properties, and applications of magnetic iron oxide nanoparticles.* Progress in Crystal Growth and Characterization of Materials, 2009. **55**(1–2): p. 22-45.

55. Laurent, S., et al., *Magnetic iron oxide nanoparticles: synthesis, stabilization, vectorization, physicochemical characterizations, and biological applications.* Chemical reviews, 2008. **108**(6): p. 2064-2110.

56. Pisanic Ii, T.R., et al., *Nanotoxicity of iron oxide nanoparticle internalization in growing neurons.* Biomaterials, 2007. **28**(16): p. 2572-2581.

57. Kim, J.S., et al., *Toxicity and Tissue Distribution of Magnetic Nanoparticles in Mice.* Toxicological Sciences, 2006. **89**(1): p. 338-347.

58. Jeong, J.-R., et al., *Magnetic properties of γ-Fe2O3 nanoparticles made by coprecipitation method.* physica status solidi (b), 2004. **241**(7): p. 1593-1596.

59. Zhu, P., et al., *Nucleation Features of the Magnetite Fe3O4 Nanoparticles with the Size of 30-40 Nm for the Hyperthermia Applications.* Advanced Materials Research, 2011. **287**: p. 77-80.

60. Chen, X., et al., *Synthesis of Highly Selective Magnetic Mesoporous Adsorbent.* J. Phys. Chem. C, 2009. **113**(22): p. 9804-9813.

61. Liu, J., et al., *Magnetic Nanocomposites with Mesoporous Structures: Synthesis and Applications.* Small, 2011. **7**(4): p. 425-443.

62. Zhang, M., et al., *Controlled Fabrication of Iron Oxide/Mesoporous Silica Core–Shell Nanostructures.* The Journal of Physical Chemistry C, 2013. **117**(41): p. 21529-21538.

63. Chen, F., et al., *In Vivo Tumor Targeting and Image-Guided Drug Delivery with Antibody-Conjugated, Radiolabeled Mesoporous Silica Nanoparticles.* ACS Nano, 2013. **7**(10): p. 9027-9039.

64. Deng, Y., et al., *Superparamagnetic high-magnetization microspheres with an Fe3O4@ SiO2 core and perpendicularly aligned mesoporous SiO2 shell for removal of microcystins.* Journal of the American Chemical Society, 2008. **130**(1): p. 28-29.

65. Knezevic, N.Z., Slowing, II, and V.S.Y. Lin, *Tuning the Release of Anticancer Drugs from Magnetic Iron Oxide/Mesoporous Silica Core/Shell Nanoparticles.* Chempluschem, 2012. **77**(1): p. 48-55.

66. MacLachlan, M. and G. Ozin, *Periodic mesoporous organosilicas, PMOs: fusion of organic and inorganic chemistry 'inside'the channel walls of hexagonal mesoporous silica.* Chemical Communications, 1999(24): p. 2539-2540.

67. Deng, Y., et al., *Superparamagnetic High-Magnetization Microspheres with an Fe3O4@SiO2 Core and Perpendicularly Aligned Mesoporous SiO2 Shell for Removal of Microcystins.* Journal of the American Chemical Society, 2007. **130**(1): p. 28-29.

68. Anbia, M. and S. Salehi, *Removal of acid dyes from aqueous media by adsorption onto amino-functionalized nanoporous silica SBA-3.* Dyes and Pigments, 2012. **94**(1): p. 1-9.

69. Behrens, S.H. and D.G. Grier, *The charge of glass and silica surfaces.* The Journal of Chemical Physics, 2001. **115**(14): p. 6716-6721.

70. Slowing, I., B.G. Trewyn, and V.S.Y. Lin, *Effect of Surface Functionalization of MCM-41-Type Mesoporous Silica Nanoparticles on the Endocytosis by Human Cancer Cells.* Journal of the American Chemical Society, 2006. **128**(46): p. 14792-14793.

71. Lin, Y.-S. and C.L. Haynes, *Impacts of Mesoporous Silica Nanoparticle Size, Pore Ordering, and Pore Integrity on Hemolytic Activity.* Journal of the American Chemical Society, 2010. **132**(13): p. 4834-4842.

72. Niu, D., et al., *Synthesis of Core−Shell Structured Dual-Mesoporous Silica Spheres with Tunable Pore Size and Controllable Shell Thickness.* Journal of the American Chemical Society, 2010. **132**(43): p. 15144-15147.

73. Tang, F., L. Li, and D. Chen, *Mesoporous Silica Nanoparticles: Synthesis, Biocompatibility and Drug Delivery.* Advanced Materials, 2012. **24**(12): p. 1504-1534.

74. Lee, J.E., et al., *Multifunctional Mesoporous Silica Nanocomposite Nanoparticles for Theranostic Applications.* Accounts of Chemical Research, 2011. **44**(10): p. 893-902.

75. Hollenbach, A.M., M. Peleg, and R. Rufner, *Effect of Four Anticaking Agents on the Bulk Characteristics of Ground Sugar.* Journal of Food Science, 1982. **47**(2): p. 538-544.

76. Ogihara, H., et al., *Simple Method for Preparing Superhydrophobic Paper: Spray-Deposited Hydrophobic Silica Nanoparticle Coatings Exhibit High Water-Repellency and Transparency.* Langmuir, 2012. **28**(10): p. 4605-4608.

77. Cushen, M., et al., *Nanotechnologies in the food industry – Recent developments, risks and regulation.* Trends in Food Science & Technology, 2012. **24**(1): p. 30-46.

78. Kaiser, J.-P., S. Zuin, and P. Wick, *Is nanotechnology revolutionizing the paint and lacquer industry? A critical opinion.* Science of The Total Environment, 2013. **442**(0): p. 282-289.

79. Lin, W., et al., *In vitro toxicity of silica nanoparticles in human lung cancer cells.* Toxicology and Applied Pharmacology, 2006. **217**(3): p. 252-259.

80. Huang, X., et al., *The Shape Effect of Mesoporous Silica Nanoparticles on Biodistribution, Clearance, and Biocompatibility in Vivo.* ACS Nano, 2011. **5**(7): p. 5390-5399.

81. Stöber, W., A. Fink, and E. Bohn, *Controlled growth of monodisperse silica spheres in the micron size range.* Journal of colloid and interface science, 1968. **26**(1): p. 62-69.

82. *AN INTRODUCTION TO CALCULATION METHODS FOR SURFACEAREA AND PORE SIZE FROM GAS SORPTION DATA*, in *Quantachrome Instruments Primer Series*. Quantachrome Instruments.

83. Luisa Ojeda, M., et al., *On comparing BJH and NLDFT pore-size distributions determined from N2 sorption on SBA-15 substrata.* Physical Chemistry Chemical Physics, 2003. **5**(9): p. 1859-1866.

84. Callaway, J. and N.H. March, *Density Functional Methods:Theory and Applications*, in *Solid State Physics*, D.T. Henry Ehrenreich and S. Frederick, Editors. 1984, Academic Press. p. 135-221.

85. Car, R. and M. Parrinello, *Unified approach for molecular dynamics and density-functional theory.* Physical review letters, 1985. **55**(22): p. 2471.

86. Ravikovitch, P.I., et al., *Capillary Hysteresis in Nanopores: Theoretical and Experimental Studies of Nitrogen Adsorption on MCM-41.* Langmuir, 1995. **11**(12): p. 4765-4772.

87. Breck, D.W., *Zeolite Molecular Sieves: Structure, Chemistry, and Use*. 1974, New York: Wiley-Interscience. 752 pp.

88. Tosheva, L. and V.P. Valtchev, *Nanozeolites: Synthesis, crystallization mechanism, and applications.* Chem. Mater., 2005. **17**(10): p. 2494-2513.

89. Larsen, S.C., *Nanocrystalline zeolites and zeolite structures: Synthesis, characterization, and applications.* J. Phys.Chem. C, 2007. **111**(50): p. 18464-18474.

90. Kosanovic, C., et al., *Study of the mechanism of formation of nano-crystalline zeolite X in heterogeneous system.* Microporous Mesoporous Mater., 2011. **142**(1): p. 139-146.

91. Song, W., V.H. Grassian, and S.C. Larsen, *High yield method for nanocrystalline zeolite synthesis.* Chem. Commun., 2005(23): p. 2951-2953.

92. Larlus, O., S. Mintova, and T. Bein, *Environmental syntheses of nanosized zeolites with high yield and monomodal particle size distribution.* Microporous Mesoporous Mater., 2006. **96**(1-3): p. 405-412.

93. Larsen, S., et al., *Synthesis and Use of Nanocrystalline Zeolites.* p. U.S. Patent No. 7,858,062.

94. Johnson, G.M., et al., *Structural studies of hydrated germanium X-type zeolite via Rietveld analysis of synchrotron powder X-ray diffraction data.* Microporous Mesoporous Mater., 1999. **31**(1-2): p. 195-204.

95. Johnson, G.M., A. Tripathi, and J.B. Parise, *Novel routes for the preparation of a range of germanium containing zeolites.* Chem. Mater., 1999. **11**(1): p. 10-+.

96. Concepcion-Heydorn, P., et al., *Structural and catalytic properties of sodium and cesium exchanged X and Y zeolites, and germanium-substituted X zeolite.* J. Mol. Catal. A: Chem., 2000. **162**(1-2): p. 227-246.

97. Johnson, G.M., P.J. Mead, and M.T. Weller, *Synthesis of a range of anion-containing gallium and germanium sodalites.* Microporous Mesoporous Mater., 2000. **38**(2-3): p. 445-460.

98. Vidal-Moya, J.A., et al., *Distribution of fluorine and germanium in a new zeolite structure ITQ-13 studied by F-19 nuclear magnetic resonance.* Chem. Mater., 2003. **15**(21): p. 3961-3963.

99. Sastre, G., et al., *Effect of the germanium incorporation in the synthesis of EU-1, ITQ-13, ITQ-22, and ITQ-24 zeolites.* J. Phys. Chem. B, 2004. **108**(26): p. 8830-8835.

100. Sastre, G., A. Pulido, and A. Corma, *An attempt to predict and rationalize relative stabilities and preferential germanium location in Si/Ge zeolites.* Microporous Mesoporous Mater., 2005. **82**(1-2): p. 159-163.

101. Cheng, C.H., et al., *Synthesis, characterization, and growth rates of germanium silicalite-1 grown from clear solutions.* J. Phys. Chem. B, 2006. **110**(43): p. 21430-21437.

102. Kamakoti, P. and T.A. Barckholtz, *Role of germanium in the formation of double four rings in zeolites.* J. Phys.Chem. C, 2007. **111**(9): p. 3575-3583.

103. Yang, X.B., D. Albrecht, and J. Caro, *Solvothermal synthesis of germano silicate-sodalite and silica-sodalite: Effects of water, germanium and fluoride.* Microporous Mesoporous Mater., 2007. **100**(1-3): p. 95-102.

104. O'Brien, M.G., et al., *Role of Germanium on the Nucleation and Growth of Zeolite A from Clear Solutions As Studied by in Situ Small-Angle X-ray Scattering, Wide-Angle X-ray Scattering, and Dynamic Light Scattering.* J. Phys.Chem. C, 2009. **113**(43): p. 18614-18622.

105. Schaack, B.B., W. Schrader, and F. Schuth, *How are Heteroelements (Ga and Ge) Incorporated in Silicate Oligomers?* Chemistry-a European Journal, 2009. **15**(24): p. 5920-5925.

106. Petkov, P.S., et al., *Framework Stability of Heteroatom-Substituted Forms of Extra-Large-Pore Ge-Silicate Molecular Sieves: The Case of ITQ-44.* Chem. Mater., 2012. **24**(13): p. 2509-2518.

107. Alvaro, M., et al., *Photochemical Generation of Electrons and Holes in Germanium-Containing ITQ-17 Zeolite.* J. Phys. Chem. B, 2005. **109**(8): p. 3696-3700.

108. Song, W.G., et al., *Development of improved materials for environmental applications: Nanocrystalline NaY zeolites.* Environ. Sci. Technol., 2005. **39**(5): p. 1214-1220.

109. Ogura, M., et al., *Aluminosilicate Species in the Hydrogel Phase Formed during the Aging Process for the Crystallization of FAU Zeolite.* Chem. Mater., 2003. **15**(13): p. 2661-2667.

110. Robson, H.E., *Verified Syntheses of Zeolitic Materials*. 2001: Elsevier Science Limited.

111. Bennett, J., C. Blackwell, and D. Cox, *High-Resolution Silicon-29 Nuclear Magnetic Resonance and Neutron Powder Diffraction Study of Na-A Zeolite. Lowenstein's Rule Vindicated - Correction.* J. Phys. Chem., 1983. **87**(24): p. 5050-5050.

112. Martens, J.A., et al., *Phase discrimination with silicon-29 MAS NMR in EMT/FAU zeolite intergrowths.* J. Phys. Chem., 1993. **97**(19): p. 5132-5135.

113. Ciriminna, R., et al., *The Sol–Gel Route to Advanced Silica-Based Materials and Recent Applications.* Chemical Reviews, 2013.

114. Valtchev, V. and L. Tosheva, *Porous Nanosized Particles: Preparation, Properties, and Applications.* Chemical Reviews, 2013.

115. Argyo, C., et al., *Multifunctional Mesoporous Silica Nanoparticles as a Universal Platform for Drug Delivery.* Chemistry of Materials, 2013.

116. Knezevic, N.Z., et al., *Magnetic mesoporous silica-based core/shell nanoparticles for biomedical applications.* RSC Advances, 2013. **3**(25): p. 9584-9593.

117. Yang, P., S. Gai, and J. Lin, *Functionalized mesoporous silica materials for controlled drug delivery.* Chemical Society Reviews, 2012. **41**(9): p. 3679-3698.

118. Lehman, S.E. and S.C. Larsen, *Zeolite and mesoporous silica nanomaterials: greener syntheses, environmental applications and biological toxicity.* Environmental Science: Nano, 2014.

119. Argyo, C., et al., *Multifunctional Mesoporous Silica Nanoparticles as a Universal Platform for Drug Delivery.* Chemistry of Materials, 2014. **26**(1): p. 435-451.

120. Lin, Y.-S. and C.L. Haynes, *Synthesis and Characterization of Biocompatible and Size-Tunable Multifunctional Porous Silica Nanoparticles.* Chemistry of Materials, 2009. **21**(17): p. 3979-3986.

121. Asefa, T. and Z.M. Tao, *Biocompatibility of Mesoporous Silica Nanoparticles.* Chemical Research in Toxicology, 2012. **25**(11): p. 2265-2284.

122. Zhao, W., et al., *Fabrication of Uniform Magnetic Nanocomposite Spheres with a Magnetic Core/Mesoporous Silica Shell Structure.* Journal of the American Chemical Society, 2005. **127**(25): p. 8916-8917.

123. Chen, Z., et al., *Preparation of Magnetically Separable Mesoporous Silica Microspheres with Open Pore Systems in Supercritical Carbon Dioxide.* Industrial & Engineering Chemistry Research, 2009. **48**(7): p. 3441-3445.

124. Zhen, G., et al., *Comparative Study of the Magnetic Behavior of Spherical and Cubic Superparamagnetic Iron Oxide Nanoparticles.* The Journal of Physical Chemistry C, 2010. **115**(2): p. 327-334.

125. Kucheryavy, P., et al., *Superparamagnetic Iron Oxide Nanoparticles with Variable Size and an Iron Oxidation State as Prospective Imaging Agents.* Langmuir, 2012. **29**(2): p. 710-716.

126. Hong, Y., et al., *Transport of Iron-Based Nanoparticles: Role of Magnetic Properties.* Environmental Science & Technology, 2009. **43**(23): p. 8834-8839.

127. Wang, N.-N., et al., *Preparation and characterization of magnetic iron nanoparticles encapsulated in mesoporous silica: The effects of reduction procedure and pore size.* Materials Letters, 2013. **112**(0): p. 20-22.

128. Wang, Y., et al., *Synthesis of Monodisperse, Hierarchically Mesoporous, Silica Microspheres Embedded with Magnetic Nanoparticles.* ACS Applied Materials & Interfaces, 2012. **4**(5): p. 2735-2742.

129. Lu, F., et al., *Size Effect on Cell Uptake in Well-Suspended, Uniform Mesoporous Silica Nanoparticles.* Small, 2009. **5**(12): p. 1408-1413.

130. Ruiz-Hernández, E., et al., *Aerosol-Assisted Synthesis of Magnetic Mesoporous Silica Spheres for Drug Targeting.* Chemistry of Materials, 2007. **19**(14): p. 3455-3463.

131. Arcos, D., et al., *Supramolecular mechanisms in the synthesis of mesoporous magnetic nanospheres for hyperthermia.* Journal of Materials Chemistry, 2012. **22**(1): p. 64-72.

132. Zhang, K., et al., *Facile Large-Scale Synthesis of Monodisperse Mesoporous Silica Nanospheres with Tunable Pore Structure.* Journal of the American Chemical Society, 2013. **135**(7): p. 2427-2430.

133. Molday, R.S., *Magnetic iron-dextran microspheres*. 1984: U.S.

134. Grün, M., et al., *Novel pathways for the preparation of mesoporous MCM-41 materials: control of porosity and morphology.* Microporous and Mesoporous Materials, 1999. **27**(2–3): p. 207-216.

135. Möller, K., J. Kobler, and T. Bein, *Colloidal Suspensions of Nanometer-Sized Mesoporous Silica.* Advanced Functional Materials, 2007. **17**(4): p. 605-612.

136. Qiao, Z.-A., et al., *Synthesis of Mesoporous Silica Nanoparticles via Controlled Hydrolysis and Condensation of Silicon Alkoxide.* Chemistry of Materials, 2009. **21**(16): p. 3823-3829.

137. Ge, J., et al., *Core–satellite nanocomposite catalysts protected by a porous silica shell: controllable reactivity, high stability, and magnetic recyclability.* Angewandte Chemie, 2008. **120**(46): p. 9056-9060.

138. Jin, C., et al., *Magnetic iron oxide nanoparticles coated by hierarchically structural silica: highly stable nanocomposite system and ideal catalyst supports.* Journal of Materials Chemistry A, 2014.

139. Kim, J., et al., *Multifunctional Uniform Nanoparticles Composed of a Magnetite Nanocrystal Core and a Mesoporous Silica Shell for Magnetic Resonance and Fluorescence Imaging and for Drug Delivery.* Angewandte Chemie, 2008. **120**(44): p. 8566-8569.

140. Yuan, L., et al., *Preparation of pH-responsive mesoporous silica nanoparticles and their application in controlled drug delivery.* The Journal of Physical Chemistry C, 2011. **115**(20): p. 9926-9932.

141. Castillo, S.I., et al., *Silica cubes with tunable coating thickness and porosity: From hematite filled silica boxes to hollow silica bubbles.* Microporous and Mesoporous Materials, 2014. **195**: p. 75-86.

142. Yang, Y., et al., *Engineering the Mesopores of Fe3O4@Mesosilica Core–Shell Nanospheres through a Solvothermal Post-Treatment Method.* Chemistry – An Asian Journal, 2013. **8**(3): p. 582-587.

143. Huang, S., et al., *Magnetic Fe3O4@mesoporous silica composites for drug delivery and bioadsorption.* Journal of Colloid and Interface Science, 2012. **376**(1): p. 312-321.

144. Zhang, J., et al., *One-pot synthesis and characterization of rhodamine derivative-loaded magnetic core–shell nanoparticles.* Journal of Nanoparticle Research, 2011. **13**(5): p. 1909-1916.